

DISSERTATION

Energy Measurement of Hadrons with the CERN ATLAS Calorimeter

ausgeführt zum Zwecke der Erlangung des akademischen Grades eines Doktors der
technischen Wissenschaften unter der Leitung von

Univ. Prof. Dipl.-Ing. Dr. Christian Fabjan
E141
Atominstitut der österreichischen Universitäten

eingereicht an der Technischen Universität Wien
Fakultät für Physik

von

DI Peter Speckmayer
Matrikelnummer: 9626025
428, Rue des Vertes Campagnes
01170 Gex

Wien, im Mai 2008

Kurzfassung

Der *Large Hadron Collider* am europäischen Zentrum für Teilchenphysik, CERN, erzeugt Proton-Proton-Kollisionen mit einer Energie von $\sqrt{s} = 14$ TeV. ATLAS, eines der vier großen Experimente am LHC ist ein vielseitiger Detektor mit dem die Energie und die Richtung von Teilchen gemessen werden kann die in den Proton-Proton-Kollisionen entstehen.

Das Hauptziel dieser Dissertation ist es die Genauigkeit zu ermitteln mit der, beim momentanen Verständnis für die Wechselwirkungen von Hadronen mit Materie und bei der momentanen Beschreibung des Ansprechverhaltens des zentralen ATLAS Kalorimeters, die Korrekturen, die zur vollständigen Energiemessung von Pionen notwendig sind, vorhergesagt werden können. Für den kombinierten Strahl-Test 2004 (CTB) wurde ein kompletter Abschnitt der zentralen Region des ATLAS Detektors mit all seinen Teil-Detektoren in der H8 Strahl-Linie des CERN SPS Beschleunigers installiert. Pionen und Elektronen mit Energien von 1 bis 350 GeV wurden gemessen.

Die Fähigkeit der Monte Carlo (MC) Simulationen, die grundlegenden Observablen zu beschreiben, wurde im Strahl-Test überprüft. Es wurde herausgefunden, daß die Beschreibung der longitudinalen Entwicklung des Schauers vom Fragmentationsmodell und die totale deponierte Energie sowie die radiale Ausdehnung des Schauers von den intranuklearen Kaskadenmodellen gut wiedergegeben wird. Mit dem optimierten Simulations-Modell wird die totale rekonstruierte Energie für eine Strahl-Energie von 20 GeV und höher auf 1% genau beschrieben. Die mittleren Energien in den einzelnen Schichten des Kalorimeters werden auf 10 bis 20% genau beschrieben.

Um die Qualität des Schemas zur hadronischen Kalibration zu bewerten, wurde es mit MC Simulationen und mit Daten getestet. Es konnte gezeigt werden, daß das vollständig korrigierte Signal von Pionen für MC (Daten) innerhalb von 2% (5%) von der ursprünglichen Pionenergie für eine Strahlenergie von $E > 20$ GeV liegt. Die Auflösung kann um ca. 10 (10) bis 15% (40%) im Vergleich zum unkorrigierten Signal in MC (Daten) verbessert werden. Die MC Simulationen haben Probleme die gemessene

Energie-Auflösung zu beschreiben. Es wird allerdings erwartet, daß die Abweichung von MC zu Daten geringer wird, wenn für die Berechnung der Korrekturen für die hadronische Kalibration zu den neuersten Versionen von GEANT4 gewechselt wird.

Über das Standardschema von ATLAS um Pionen zu Kalibrieren hinaus gehend wurde eine neuartige Technik zur Korrektur von Energieverlusten Aufgrund von totem Material entwickelt mit dem Verbesserungen von Linearität und Auflösung erzielt werden konnte.

Abstract

The ATLAS detector is a multi-purpose detector measuring the energy and direction of particles produced in proton-proton collisions at an energy of $\sqrt{s} = 14$ TeV provided by the Large Hadron Collider at the European center of particle physics, CERN.

The main aim of this thesis is to assess the precision of the present understanding of the interactions of hadrons with matter (as implemented in Monte Carlo (MC) simulations) to describe the response of the ATLAS calorimeter and to predict the correction necessary to measure the full energy of pions. The simulations are compared to testbeam data. The present description of the response of the ATLAS central calorimeter is able to predict the energy corrections, as verified by using testbeam data. For the Combined Test Beam 2004 (CTB) a full slice of the central region of the ATLAS detector including all sub-detectors has been installed in the H8 beam line of the CERN SPS accelerator. Pions and electrons with the energies ranging from 1 to 350 GeV have been measured.

The ability of the various MC simulations to describe the basic observables has been tested in the CTB. It has been found that the longitudinal shower development is described by the fragmentation model, while the response and the radial shower extension is well represented by using intra-nuclear cascade models. Using the best model, the description of the response is within 1% for a beam energy of 20 GeV and above. The mean energies in the individual calorimeter layers are described within 10 to 20%.

The hadronic calibration scheme has been applied on MC and data. It has been shown that the fully corrected pion signal is within 2% (5%) of the initial pion energy for $E > 20$ GeV in MC (data). The resolution is improved by about 10 (10) to 15% (40%) compared to the non-corrected signal in data (MC). The MC simulation has problems to describe the measured energy resolution. The deviation of MC and data is expected to become smaller when the corrections for the hadronic calibration are derived with the new version of GEANT4. Beyond the ATLAS standard pion calibration scheme a novel technique for the correction for the energy loss due to dead material has been developed which has shown to improve the linearity and the resolution.

Acknowledgements

First, I want to thank my doctoral thesis adviser Prof. Christian Fabjan for the opportunity to work at CERN and his great support during the work on my thesis. Special thanks go to Tancredi Carli—my CERN supervisor—who guided my work on a day-by-day basis and who introduced me to calorimetry in general and the ATLAS calorimeter system in particular.

My ATLAS colleagues deserve being mentioned here, since they created a pleasant atmosphere which has made the time being a PhD student at CERN a very enjoyable experience. To name a few of them: Ana (my group leader), Martin, Walter, Nils, Robert, Claudio, Gerolf, Vincent, Irene and many more. Since one spends most of the time in the office, I want to mention in particular some of my office mates: Margar, Francesco, Christophe and Amir. They were always in a good mood and made coming to work in the morning so much more fun. I especially want to thank Amir—who shares my compassion for beautifully designed computer programs—for the nice conversations we had.

For the work on the hadronic calibration, I owe thanks to the people from the hadronic calibration group. Sven, Guennadi, Peter, Karl-Johan, thanks for the help with software, dead material corrections and the good questions in the meetings. It was a pleasure working with you!

For lunch-times and leisure activities, such as parties, the austrian community at CERN has been an enjoyable company. Thanks!

I want to thank my parents a lot for just everything and last, but certainly not least I want to thank my wife Mónica for her enormous support, which has made writing this thesis much easier.

Contents

Introduction	1
1 Physics at the LHC	4
2 LHC and Detectors	8
2.1 The LHC	8
2.2 The LHC experiments	10
2.2.1 CMS	10
2.2.2 ALICE	11
2.2.3 LHCb	12
3 ATLAS Detector	14
3.1 Overview of the ATLAS detector	14
3.2 Inner Detector	15
3.3 Calorimetry system	16
3.3.1 Liquid Argon calorimeter	17
3.3.2 Tile Calorimeter	21
3.4 Muon system	24
4 Interaction of particles with matter	26
4.1 Energy loss of charged particles	26
4.2 Development of electromagnetic showers	27
4.3 Energy resolution of sampling calorimeters for electromagnetic showers .	30
4.4 Development of hadronic showers	31
4.4.1 Energy measurement of hadronic showers	34
4.4.2 Visible, invisible and escaped energy	34
4.5 Summary	40
5 Implementation of models of the interaction of particles with matter in Monte Carlo Simulations	41

5.1	Design overview of GEANT4	42
5.2	Structure of GEANT4	43
5.2.1	Events	43
5.2.2	Geometry	43
5.2.3	Tracking and transportation	44
5.3	Physics processes and models	46
5.3.1	Decay of particles and nuclei	47
5.3.2	Electromagnetic processes	48
5.3.3	Hadronic processes	50
5.4	Optical processes	54
5.5	Physics lists	54
5.5.1	Models and energy regions	55
5.5.2	Implemented physics lists	56
5.6	CalibrationHits and calculation of the invisible energy	58
5.7	Summary	58
6	Computing Model	60
6.1	The LHC Computing Grid	60
6.2	Simulations of the CTB on the GRID	61
7	Combined Testbeam 2004 (CTB)	63
7.1	The setup of the H8 beam line	63
7.1.1	Calculation of the beam energy	63
7.1.2	Description of the beam instrumentation	66
7.2	Data set and event selection	69
7.3	Simulation of the detector response in Monte Carlo	70
7.3.1	Modeling of noise	71
7.3.2	Photo statistics	71
7.3.3	Light attenuation in the Tile calorimeter cells	71
7.3.4	Recombination effects in LAr for heavily ionizing particles	72
8	Calorimeter calibration	75
8.1	Calibration of the electromagnetic energy scale	76
8.1.1	Liquid Argon calorimeter	76
8.1.2	Tile calorimeter	78
8.2	Calibration of the hadronic energy scale (energy measurement)	80
8.2.1	Topological clustering	82

8.2.2	Weighting correction for invisibly deposited energy	88
8.2.3	Out-of-cluster corrections	90
8.2.4	Dead material corrections in ATLAS	91
8.3	Summary	98
9	Comparison of data to Monte Carlo simulations	100
9.1	Comparison of the energy distribution in the calorimeter layers	101
9.2	Comparison of the cluster moments and estimators for selected physics lists	116
9.3	Energy sharing between the LAr and Tile calorimeters	123
9.4	Energy sharing and selected moments for 20 GeV pions	127
9.5	Summary	127
10	Hadronic energy measurement with the ATLAS baseline method	131
10.1	Technical details	131
10.2	Weighting correction	132
10.3	Out-of-cluster corrections	133
10.4	Dead material corrections	135
10.5	Combined corrections applied on MC	137
10.6	Combined corrections applied on data	138
10.7	Comparison of different dead material corrections in MC simulations . .	140
10.8	Discussion	142
	Conclusions	144
	Appendix: Historical Remarks on the Monte Carlo Method	147
	Glossary	148
	Bibliography	151
	Curriculum Vitae	155

Introduction

The European Organization for Nuclear Research (CERN) has been founded in 1954 for the purpose of building a European research facility to study the fundamental constituents of matter. Beside the 20 European member states further 65 countries are involved with CERN either as observer states or non-member states. About 9000 scientists from nearly 600 institutes and universities from those countries participate with research undertaken at the facilities at CERN.

The Large Hadron Collider, a large circular particle accelerator and storage ring, is currently under construction. It will serve to study matter on a sub-nuclear scale by colliding protons or ions. The protons will collide with a center of mass energy of up to 14 TeV and a luminosity of $10^{-34} \text{ cm}^{-2}\text{s}^{-1}$. Four large experiments are built at the LHC searching for new physical effects.

One of those experiments is ATLAS. It is a general purpose detector which will be used to search for new particles, like the Higgs boson, or new short-distance interactions. ATLAS consists of an Inner Tracking Detector, a calorimeter system and a muon system.

One of the main aims of the ATLAS calorimeter system is to measure the energy of hadrons. The quarks and gluons produced in the hard scattering of the colliding proton constituents lead to bundles of hadrons, called jets. The measurement of jets is important for most physics analyses at LHC. For instance, the single inclusive jet cross-section as a function of the jet transverse momentum is one of the first measurements that can be performed at the LHC and gives insights into QCD, the theory of strong interactions and in particular the proton structure and the strong coupling at large momentum transfers. At very large transverse momenta new interactions, e.g. from contact interaction, might be revealed. The sensitivity to find such new effects requires a good control of the uncertainty of the energy measurement. Another example, where the measurement of hadrons is important is the search of an extension of the Standard Model called supersymmetry (SUSY). In most SUSY models the lightest SUSY particle is stable. Given the expected very low interaction probability with matter, the typical signature is

missing transverse energy. The measurement of the missing transverse energy is directly related to the ability to correctly measure jets and low energetic hadrons.

Parts of the energy deposited by hadron showers in the calorimeter can not be measured, since they lead to energy deposit which are not measurable ("invisible") (e.g. break-up of nuclei, nuclear excitation). Also, in regions where no active elements of the calorimeter are present (e.g. cables, cryostat walls) called *dead material*, energy cannot be measured. The amount of energy deposited in those regions has to be estimated from other observables such as energies in the neighbouring layers or observables which describe the shower topology.

The so-called *local hadronic calibration* is the default calibration scheme in ATLAS. The corrections for invisible energy, dead material energy, etc. are derived from Monte Carlo simulations and are then applied on the data. This strategy relies strongly on the accuracy of the description of the data by Monte Carlo simulations. In this thesis, the question is addressed to which extent the presently available Monte Carlo simulations are able to provide the calibration constants by applying this calibration scheme on testbeam data where a full slice of the ATLAS detector has been exposed to pion beams.

After a short description of the LHC physics program in chapter 1, chapter 2 presents the LHC and the four large experiments ATLAS, CMS, ALICE and LHCb. Whereas ATLAS and CMS are multi purpose detectors to exploit the physics produced in pp -collisions, ALICE focuses on ion-ion-collisions and LHCb is specialized for the measurement of mesons containing heavy quarks.

The ATLAS detector and its sub-detectors are explained in chapter 3.

In chapter 4, the interactions of particles with matter are described, emphasizing the development of electromagnetic and hadronic showers. The modeling of those interactions in Monte Carlo simulations is explained in chapter 5.

The simulation of a large number of events at many energies and with varying geometry and with different physics models has been necessary. This amount of simulation could only be done using the powerful computing network GRID. Chapter 6 gives a brief overview about the properties and the structure of the LHC GRID.

In chapter 7, the setup of the Combined Test Beam 2004 is described. In this testbeam a full slice of the barrel region of the ATLAS detector including all sub-detectors has been installed in the H8 beam line of the CERN SPS accelerator. Pions and electrons with

the energies ranging from 1 to 350 GeV have been measured. The selection of the events is explained and the Monte Carlo simulation of the detector response is presented.

Chapter 8 focuses on the calorimeter calibration. First the calibration of the electromagnetic energy scale is explained. Subsequently, based on the electromagnetic energy scale, the calibration of the hadronic energy scale with the local hadronic calibration scheme is presented. For the dead material correction two alternative methods are compared.

In chapter 9, several observables like the total response and resolution as well as the energy distribution in the individual calorimeter layers and variables characterizing the hadronic shower topology are measured in the data and are compared to various Monte Carlo simulations including a large variety of physics models.

In chapter 10, the local hadronic calibration scheme is applied on MC simulations to test its performance on self-consistency. Finally the local hadronic calibration scheme is applied to data.

1 Physics at the LHC

This chapter outlines the current status of the Standard Model of particle physics and hypothetical theoretical models which describe the physics beyond the Standard Model (supersymmetric models).

The *Standard Model* (SM) of particle physics describes the four fundamental interactions of nature: electromagnetism, weak interaction and strong interaction. It is a quantized theory consisting of quantum electroweak and quantum chromodynamics theories. It involves 12 fermions (see tab. 1.1) and their respective antiparticles, which are the constituents of matter and 5 bosons which carry the forces (see tab. 1.2).

On the other hand, there is the general relativity theory, which is the most accurate model available to describe the gravitational force between two masses. Gravitation acts even on large distances across the universe and is modeled with a curvature of the space-time. However, general relativity theory is not quantized.

All attempts to combine gravitation with the SM theory are still in an early stage. There is no model available which includes all four elementary forces and of which predictions have been verified in data. For instance, in the last few years many models assuming large extra space-time dimensions have been developed which explain the weakness of gravitation with respect to the other forces by the fact that only the gravitational force

generation	quarks		leptons	
1	u	up	e	electron
	d	down	ν_e	electron neutrino
2	c	charm	μ	muon
	s	strange	ν_μ	muon neutrino
3	t	top	τ	tau
	b	bottom	ν_τ	tau neutrino

Table 1.1: List of presently known fermions.

force	boson
electromagnetic	γ (photon)
weak interaction	W^+ W^- Z^0
strong interaction	g (gluon)

Table 1.2: List of presently known bosons.

acts in all space-time dimensions while the other forces are restricted to the 3+1 space-time dimensions which we are familiar with. Such models predict e.g. a dramatic change of the jet cross-section at large transverse momenta at the LHC. New experimental results at the LHC might give valuable hints on models, where all known forces are combined.

The SM is a remarkably successful theory which describes the interaction of the presently known particles with excellent accuracy. However, to explain why the particles have masses, the SM has to introduce the so called *Higgs boson*. The Higgs boson has the property that the coupling is proportional to the particle masses. The Higgs boson has not yet been observed. Finding the Higgs boson would complete the SM. In the context of the SM, there are several decay channels which could be exploited to discover the Higgs boson at the LHC depending on its energy (l denote leptons and j jets). The mass of the Higgs boson is not known. From searches at LEP we know that it has to be larger than ~ 114 GeV and from theoretical arguments it is expected to be smaller than ~ 300 GeV.

80	100	150	200	...	1000	[GeV]
H \rightarrow $b\bar{b}$						
	H \rightarrow $\gamma\gamma$					
		H \rightarrow $ZZ^* \rightarrow 4l^\pm$				
			H \rightarrow $ZZ \rightarrow 4l^\pm, 2l^\pm 2\nu$			
			H \rightarrow $WW, ZZ \rightarrow l^\pm \nu 2j, 2l^\pm 2j$			

For the light Higgs boson the most promising channel is the decay channel in two photons (despite its small branching ratio). If the Higgs boson mass is larger than twice the Z -boson mass, the most promising signature is the decay into two Z s, decaying into four leptons. In both cases an excellent performance of the electromagnetic calorimeter

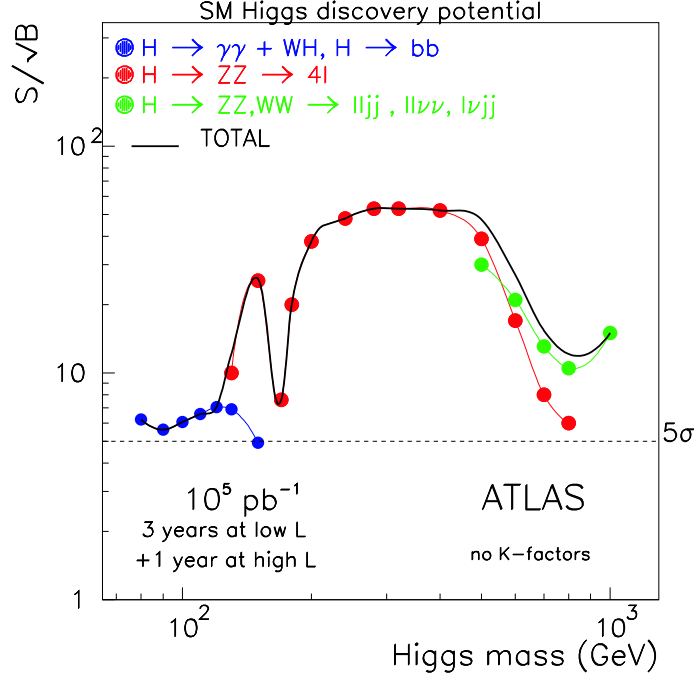


Figure 1.1: The expected significance of the signal of a SM Higgs boson as a function of its mass for an integrated luminosity of 10^5 pb^{-1} .

is needed. The measurement of the hadronic energy in the form of jets becomes important at high Higgs masses, when W -boson pairs are produced that decay into jets. All these channels have to be isolated from an overwhelming background.

In fig. 1.1 the expected significance of the signal of the Higgs boson as a function of its mass is shown for an integrated luminosity of 10^5 pb^{-1} .

Despite the success of the SM, some questions remain which suggest that a more complete model waits to be discovered. Coupling constants and masses in the SM cannot be derived by first principle calculations which is a non-satisfactory situation. Another question which occurs when looking at the particle tables is: why are there three generations? Physicists develop models beyond the SM which address these questions and which might provide deeper insight into the structure of our universe.

Supersymmetry (SUSY) is one of the models which might be a ‘matured’ extension of the SM. The basic idea behind SUSY is that there exists a corresponding supersymmetric fermion for each boson and vice versa, thus doubling the number of particles. In this way the radiative correction to the Higgs boson mass can be stabilized, since the superpartner

cancels the effects of the SM particles in quantum loops. There is no direct evidence yet for supersymmetry which implies, that the superpartners have to be heavy, if the universe is supersymmetric.

The Minimal Supersymmetric Standard Model (MSSM) is the most simple SUSY model. The model adds the particle types: squarks, gluinos, charginos, neutralinos and sleptons to the list of existing particles. One important feature of the MSSM is that all supersymmetric particles decay into the lightest one which—due to the very small interaction cross-section—is not detected resulting in an apparent momentum imbalance and leading to *missing transverse energy* (E_T^{miss}). The determination of E_T^{miss} requires a precise energy measurement in particular of the hadronic energy, a hermetical coverage of the 4π steradians around the interaction points for pp -collisions and an excellent calibration of the calorimeter. The MSSM model would provide further channels for the decay of Higgs bosons:

$$\begin{aligned} A &\rightarrow \tau^+ \tau^- \rightarrow \mu + \nu\text{'s} \\ &\rightarrow l^\pm \text{ and hadrons and } \nu\text{'s} \end{aligned}$$

$$\begin{aligned} H^\pm &\rightarrow \tau^\pm \nu \\ &\rightarrow 2j \end{aligned}$$

In all these channels the performance of the hadronic calorimeter is important.

2 LHC and Detectors

This chapter gives an introduction to the Large Hadron Collider and its major experiments. The ATLAS experiment is explained in the next chapter.

2.1 The LHC

The Large Hadron Collider (LHC) is a circular particle accelerator built at CERN in the border region of France and Switzerland near Geneva. The LHC is built into a tunnel with a circumference of approximately 27 km which was excavated for the Large Electron-Positron collider (LEP) which has been shut down in 2000. A schematic diagram of the LHC is shown in fig. 2.1. The use of the LEP-tunnel has been the main constraint for the 7 TeV beam energy for protons. The LHC can accelerate protons and ions.

In circular particle colliders, intense magnetic fields keep the particles in a circular trajectory. The particles are accelerated by radio frequency (RF) cavities where the particles pass by at each cycle. Two beams of particles are accelerated in opposite directions and brought to head-on collisions in the center of the experiments. The advantage over linear collisions is, that the beam is stored and a high luminosity can be achieved. Compared to fixed target experiments colliders achieve the higher center-of-mass energy for the same beam energy. At particle colliders the experiments have to cover typically 4π steradians, since the produced particles are covering all directions. Particles moving in circular trajectory loose energy due to synchrotron radiation. The synchrotron radiation scales with $(E/m)^4$ where E is the particle energy and m the particle mass. While this effect has been very large at LEP, where electrons and positrons have been accelerated, it is much smaller at the LHC, since the proton mass is about 1800 times higher than the electron mass.

The two main parameters for a particle accelerator are luminosity and energy:

The **luminosity** is related to the rate of the particle collisions. With the LHC experiments physical effects are searched for which happen very rarely and are typically covered by background produced by other effects which have much larger cross-sections. Therefore, for measurements large statistics is necessary to be able to distinguish the

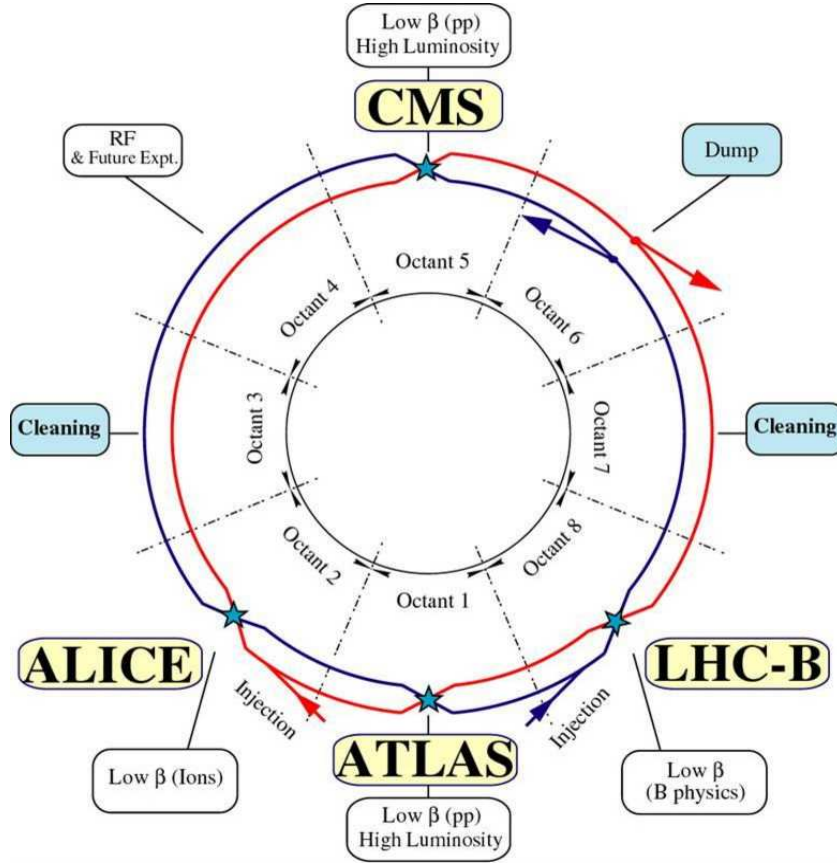


Figure 2.1: Schematic of the Large Hadron Collider (LHC). The four large LHC experiments (ATLAS, CMS, ALICE, LHCb) are shown. At their positions the two beams can be brought to collision.

signal from the background events. A high luminosity is necessary to make a maximum of observations in the available time.

The **energy** of the particles is the second important factor. Many interesting physical effects which are searched for only occur if the energy which is available for their creation is sufficiently high. LHC is the first accelerator that crosses the border into the TeV range and is able to produce beam energies in ranges which could reached up to now only by measuring cosmic radiation. A higher beam energy augments the number of particles which are produced in a collision which makes the analysis more difficult.

The particles are injected with the succession of the Proton Synchrotron (PS) and subsequently the Super Proton Synchrotron (SPS) into the LHC with an energy of 450 GeV, where it is accelerated to the full energy of 7 TeV which allows for a center-of-mass energy for the collision of 14 TeV. The luminosity of the LHC will be $10^{34} \text{ cm}^{-2}\text{s}^{-1}$ for protons. The dipole magnets of the LHC produce a magnetic field of 8.4 T are supercon-

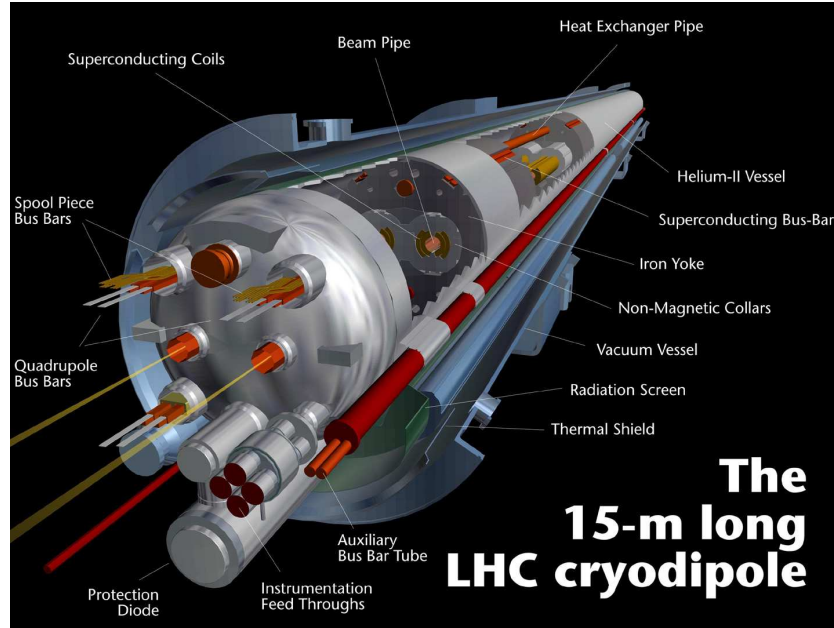


Figure 2.2: Schematic of a dipole magnet of the LHC.

ducting. For cooling purposes superfluid helium ($T \sim 1.9$ K at atmospheric pressure) is used which has a lower viscosity and a higher heat transmission capacity than liquid helium which is not superfluid. A schematic of a LHC dipole magnet is shown in fig. 2.2. The 27 km LHC ring consists of 1232 dipole magnets in eight sectors. At the LHC, the beam consists of bunches of about 10^{11} protons every 25 ns (7 m). When fully filled, the LHC contains about 2800 bunches. At design luminosity in one event (collision of bunches in the detector) about 20 proton-proton collisions take place.

2.2 The LHC experiments

In the following the LHC experiments CMS, ALICE and LHCb are briefly presented. The ATLAS experiment is explained in detail in sec. 3.

2.2.1 CMS

CMS is the acronym for Compact Muon Solenoid named after the 4 Tesla solenoid on which the CMS design is based on. The CMS detector is 21.5 m long, 15 m wide and 15 m high. It has a weight of about 12500 tonnes (see fig. 2.3). The innermost part is the tracker consisting of two barrel layers and two end-cap discs of pixel detectors and 25000 silicon strips. Outside the tracker, the electromagnetic calorimeter (ECAL) is situated.

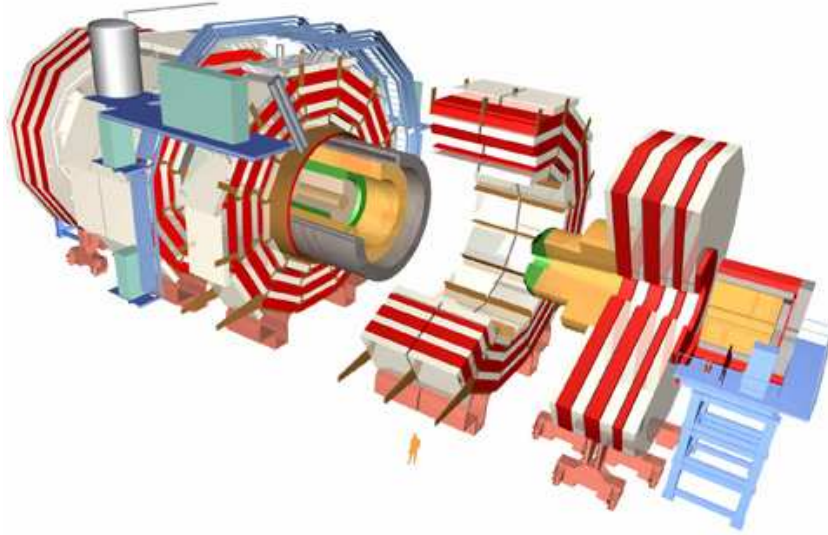


Figure 2.3: Schematic of the CMS detector.

It consists of over 80000 PbWO_4 crystals whose short radiation length allows for a very compact electromagnetic calorimeter. A preshower detector to correct for dead material effects in front of the calorimeter is used in the end-cap region. The hadronic calorimeter (HCAL) consists of a barrel and two end-cap regions. The absorbers are made of copper, the active material are scintillators. The hadronic forward calorimeters at each end of the CMS detector use steel absorber plates which reduce the activation under irradiation compared to copper. The magnet system consists of a large superconducting coil and a magnetic yoke in the barrel and the end-cap region. For the muon chambers gaseous particle detectors have been chosen. In the central barrel regions drift tubes are used, in the end-cap region cathode strip chambers are used and in both barrel and end-cap region there are in addition resistive parallel plate chambers.

2.2.2 ALICE

ALICE (an acronym for *A Large Ion Collider Experiment*) is a detector dedicated to measuring heavy-ion collisions with the aim to study hadrons, electrons, muons and photons produced in heavy-nuclei collisions (e.g. Pb). In those collisions a state of matter called *quark gluon plasma* is thought to be created (see fig. 2.4) that is similar to the state of matter in the very early steps of the creation of the universe [1].

ALICE is 26 m long, 16 m high and 16 m wide. It weighs 10000 tonnes. It has a central barrel part and a single arm forward muon spectrometer. The central detector sys-

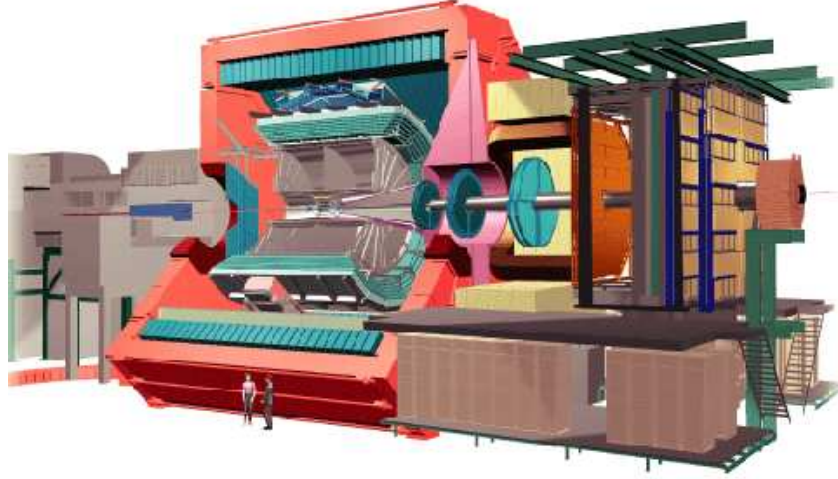


Figure 2.4: Schematic of the ALICE detector.

tem consists of the Inner Tracking System (ITS) which are six layers of high-resolution silicon-detectors, the Time Projection Chamber (TPC) which is the tracking system and the central part of ALICE, a Transition-Radiation Detector (TRD) and a Time-Of Flight (TOF) detector for particle identification. Furthermore, there are two small-area detectors: an array of Čerenkov detectors, a High-Momentum Particle Identification Detector (HMPID) and an electromagnetic calorimeter made of high-density PbWO_4 crystals. There are several forward systems: a muon spectrometer, the Photon Multiplicity Detector (PMD) and the Forward Multiplicity Detector (FMD). ALICE uses the solenoid from the LEP experiment L3. The nominal luminosity for the measurements of Pb-Pb collisions in ALICE is $10^{27} \text{ cm}^{-2}\text{s}^{-1}$. The commissioning will be done with pp -collisions, which are studied as well for effects where ALICE is competitive to the dedicated pp experiments ATLAS and CMS and for reference data for the ion analysis.

2.2.3 LHCb

A Large Hadron Collider beauty experiment (LHCb) is built in the cavern which was formerly used by the LEP experiment DELPHI. LHCb is designed for precision measurements of CP violations in the heavy quark mesons (mainly from beauty quarks) and for the search of rare B -meson decays. It will provide the possibility to study small differences between matter and antimatter. The experiment is 21 m long, 10 m high, 13 m wide and its weight is 5600 tonnes. It is a single arm spectrometer in the forward region with planar detectors [2]. LHCb is designed only to work at a luminosity of $10^{32} \text{ cm}^{-2}\text{s}^{-1}$.

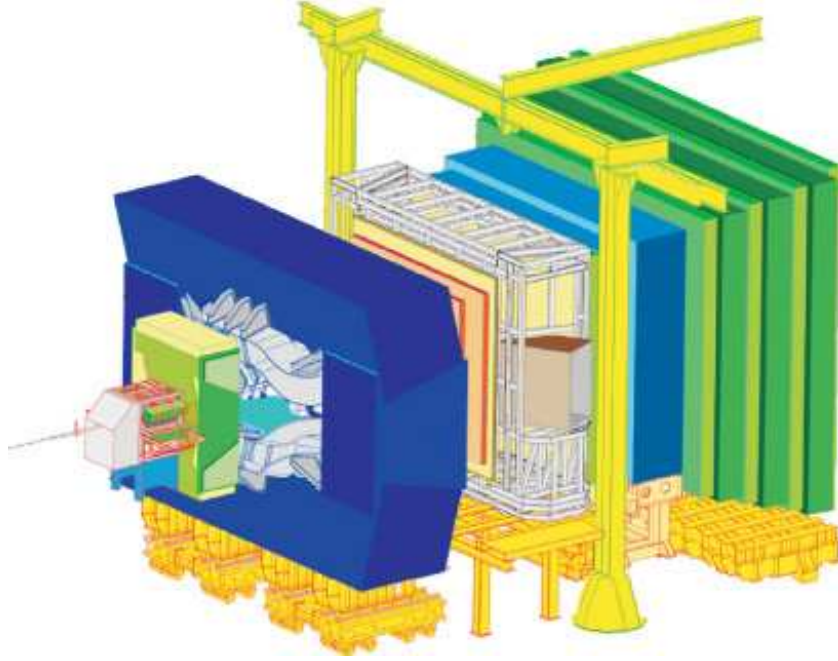


Figure 2.5: Schematic of the LHCb detector.

The part of LHCb which is closest to the interaction point of the pp -collisions is the Vertex LOcator (VELO). It consists of Silicon detectors and is used to observe the decay products of B -mesons. Two Ring Imaging Čerenkov counters (RICH) identify charged particles. They build together with the silicon tracker (a large-surface silicon microstrip detector) the tracking system. A part of the tracking system is placed inside a dipole magnet. An electromagnetic and a hadronic calorimeter are used to identify electrons and hadrons for the trigger and for offline analysis. A muon detector is used for muon identification and the trigger. Emphasis is put on the high performance trigger system which has to select those pp collisions which produce B mesons [2].

3 ATLAS Detector

In this chapter, the ATLAS detector and its subdetectors—the Inner Detector, the calorimetry system and the muon system—are explained.

3.1 Overview of the ATLAS detector

ATLAS which is the largest of the LHC experiments has been designed as a multi-purpose detector for the measurement of proton-proton collisions at a center-of-mass energy of 14 TeV and a luminosity of $10^{34} \text{ cm}^{-2}\text{s}^{-1}$. ATLAS is the acronym for *A Toroidal LHC ApparatuS*.

ATLAS consists of an inner detector, a calorimeter and muon detectors. In the in-

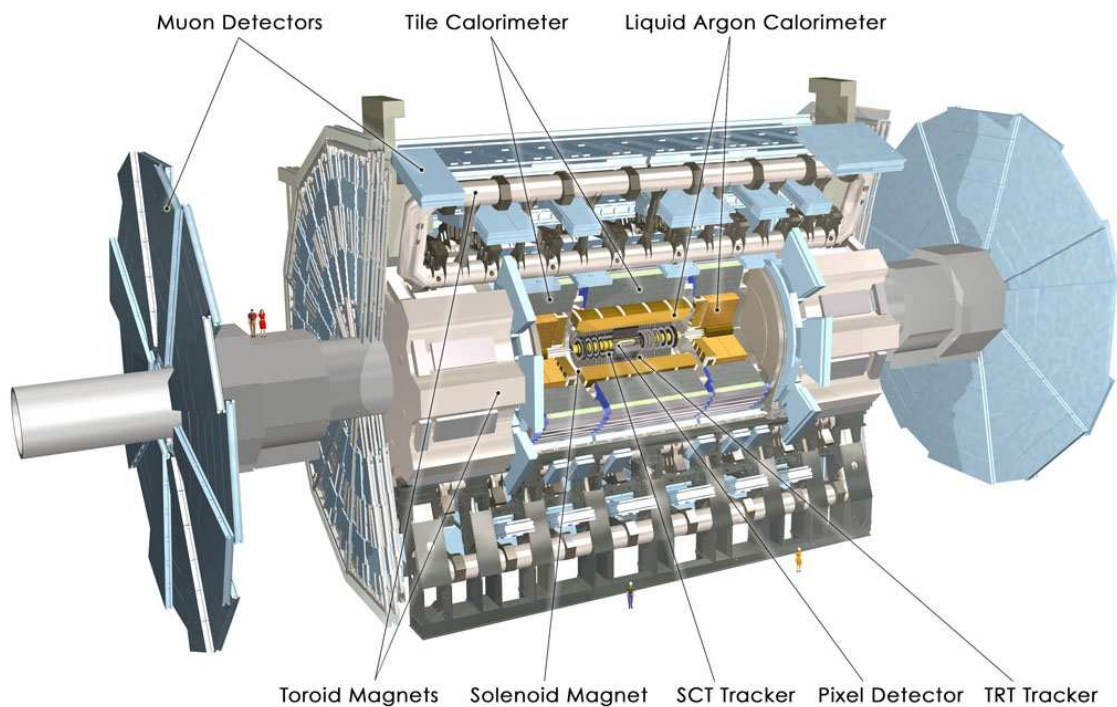


Figure 3.1: Visualization of the ATLAS detector.

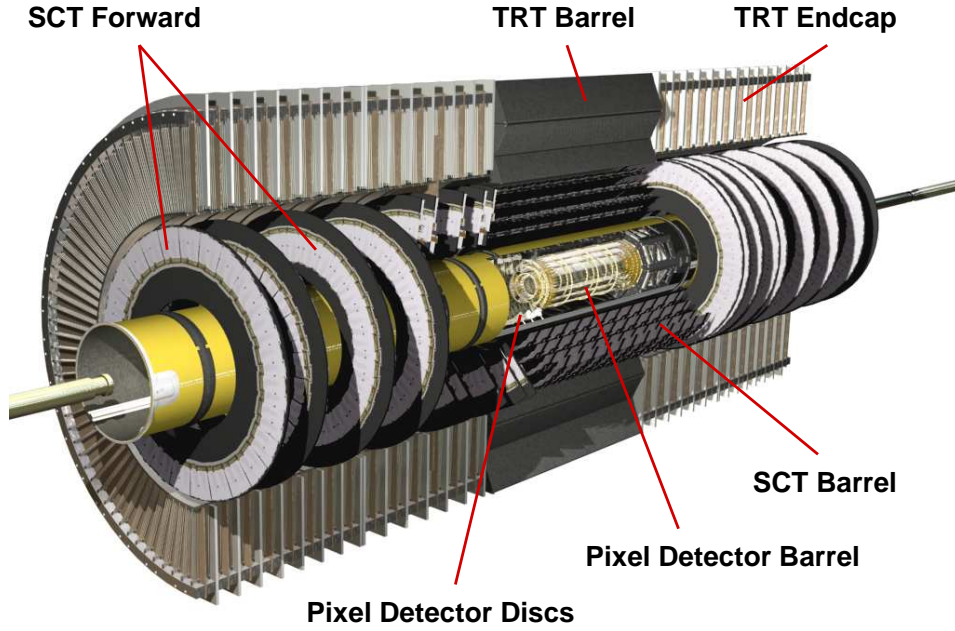


Figure 3.2: Visualization of the Inner Detector.

ner detector the position and the momenta of the charged particles emerging from the interaction point of the pp collisions are measured. The calorimeter, consisting of several subsystems, is placed around the inner detector and is used to measure the energy of charged and neutral particles. Muons leaving the calorimeter are measured in the muon chambers. A large magnet system consists of a solenoid and air-core toroids. The solenoid creates a magnetic field of 2 T and is placed in front of the central part of the LAr calorimeter. The toroid magnet consists of a central part and two end-caps [3].

3.2 Inner Detector

The role of the ATLAS Inner Detector is the reconstruction of the position and the momentum of tracks of charged particles from the collision. It also measures the positions of vertices of the decay products of long lived particles like kaons or mesons containing c - and b -quarks with high efficiency. Some of the objectives of the design have been an excellent sensitivity to the largest possible Higgs mass range, the search for possible new heavy W- and Z-like objects, the search for SUSY particles and precise measurements of the top quark mass. Requirements which the Inner Detector has to cope with are large particle fluxes expected at a luminosity of up to $10^{34} \text{ cm}^{-2}\text{s}^{-1}$.

The detector is 7 m long, has a diameter of 115 cm and is composed of three sections, one central section (± 80 cm) and one end-cap at each end. The total pseudorapidity covered is $|\eta| < 2.5$. The Inner Detector is contained in a solenoidal magnet with a central field of 2 T.

The innermost part of the Inner Detector is the Pixel detector which has the highest granularity and thus provides the highest resolution. The accumulated dose over 10 years of operation is 300 kGy of ionizing radiation and over 5×10^{14} neutrons per cm^2 are expected. Hence, a high radiation resistance is required. The second part is the semiconductor tracker (SCT) where silicon microstrips are used. These two high precision parts are within a diameter of 56 cm. The third part is a transition radiation tracker (TRT) consisting of 420000 straws with a diameter of 4 mm each. Transition radiation photons are created in a radiator between those straws allowing a separation of electrons and pions and providing a resolution of $170 \mu\text{m}$ per straw and allow for a continuation of the track measurement of the Pixel and SCT.

The use of high resolution detectors at smaller radii and tracking elements at larger radii provides a precise measurement of the ϕ and z coordinates and a robust pattern recognition. The number of precision layers is limited to keep the material budget and the cost of the Inner Detector within acceptable limits.

3.3 Calorimetry system

The purpose of the ATLAS calorimetry system is the energy and position measurement of electrons, photons and jets and to contribute to the particle identification. It is also designed to provide a precise estimation of the missing transverse energy.

The calorimetry system of ATLAS consists of an electromagnetic calorimeter which is optimized for the accurate measurement of electrons and photons and a hadronic calorimeter for the measurement of hadron showers. The whole calorimetry system is divided into a central part and two end-cap parts and a Forward-Calorimeter in the two forward regions. Fig. 3.3 shows a sectional drawing of the calorimeter system and its division into the subsystems. For the electromagnetic calorimeters, the hadronic end-caps and for the forward calorimeter liquid argon is used as active material. The passive materials are lead for the electromagnetic calorimeter, copper for the hadronic end-caps and tungsten for the forward calorimeter. For the hadronic central calorimeter (Tile calorimeter) the active material are scintillators, the passive material is steel.

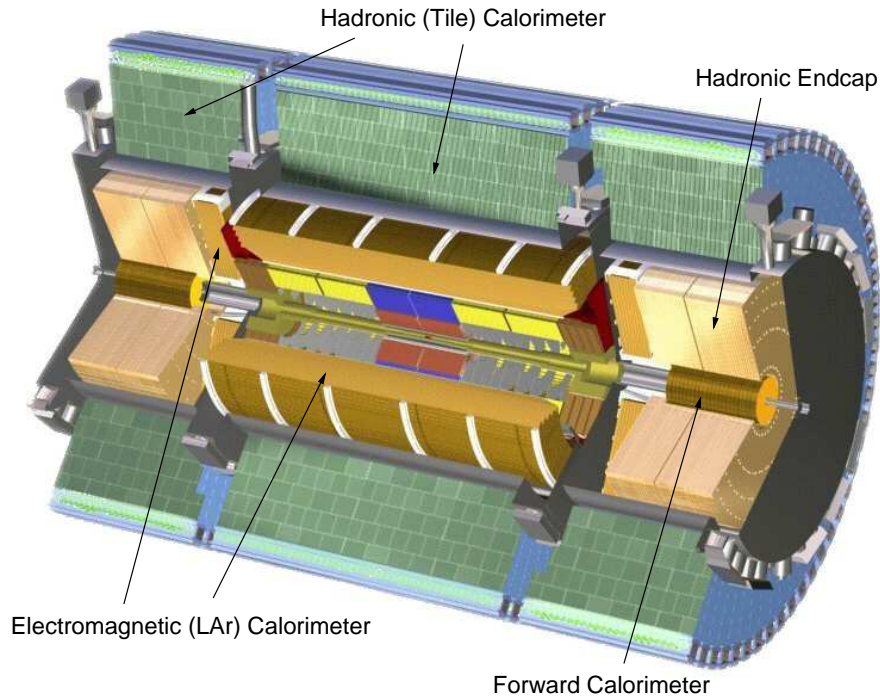


Figure 3.3: Schematic of the calorimetry system. Shown are the central region (‘barrel’ in ATLAS terms) with hadronic calorimeter and electromagnetic calorimeter and the two end-cap regions with the hadronic calorimeter (extended barrel), hadronic end-cap and the Forward calorimeter.

3.3.1 Liquid Argon calorimeter

The research and design effort for the ATLAS Liquid Argon (LAr) calorimeter has been started in 1990. Several requirements have to be met by the design of the calorimeter to be able to provide accurate measurements:

- good energy resolution for electrons and photons
- good uniformity, i.e., the same energy response in all parts of the calorimeter
- insignificant amount of leakage for electron showers (sufficient thickness of the calorimeter)
- accurate measurement of the shower direction (high angular resolution)(for photons where tracks are available)
- large rapidity coverage

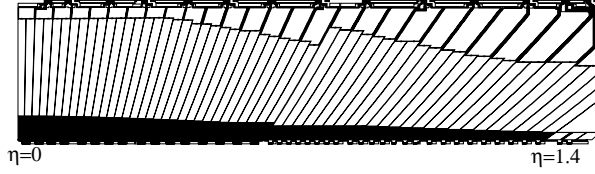


Figure 3.4: Sketch of the cell structure of the LAr calorimeter. It consists of a highly granular first layer (strips), the coarser middle layer and the back layer.

The liquid argon calorimeter is divided into several subsections. The region below pseudorapidity of 1.475 is called ‘barrel’. The end-caps start at $|\eta| = 1.375$ and end at $|\eta| = 3.2$. There are two further calorimeters with liquid argon as active material, the hadronic LAr End-cap between pseudorapidity of 1.5 and 3.2 (HEC) and the forward LAr calorimeter from 3.1 to 4.9 (FCAL).

The liquid argon calorimeter in the central region is a sampling calorimeter with a lead absorber and liquid argon as active material. In most of the calorimeters which have been operated in high energy physics the absorber plates have been placed such that the particles impinge approximately perpendicularly. However, with such a structure where active and passive layers are parallel (concentrically) to the beam-line, cables for signal read-out and high-voltage supply have to be routed through the detector volume. With a structure where active and passive layers are perpendicular to the beam-line, a strong dependency of the sampling fraction to the particle impact point is introduced. This is due to the fact, that electron showers deposit a large fraction of their energy in the shower core. For showers with pseudorapidity close to 0 where the shower axis is nearly parallel to active and passive layers, it is likely, that most of the energy is deposited in either an active layer or a passive layer. To overcome these two problems, the electrodes (active and passive layers) are folded in an accordion structure such that the cell borders point towards the interaction point (see fig. 3.4). This allows to route the cables (signal and high-voltage) in the front and in the back of the detector volume while optimizing the sampling of the showers as they have to pass independently from η through a large number of active and passive layers. The readout configuration of the liquid argon calorimeter in the central region consists of about 150.000 cells.

The accordion part of the LAr calorimeter in the central region consists of three layers called *front*, *middle* and *back*, shown in fig. 3.5. From the interaction point to the calorimeter there are (depending on η) about 2.5 radiation lengths of material. To estimate the amount of energy in that material, a *presampler* (thickness 11 mm) is

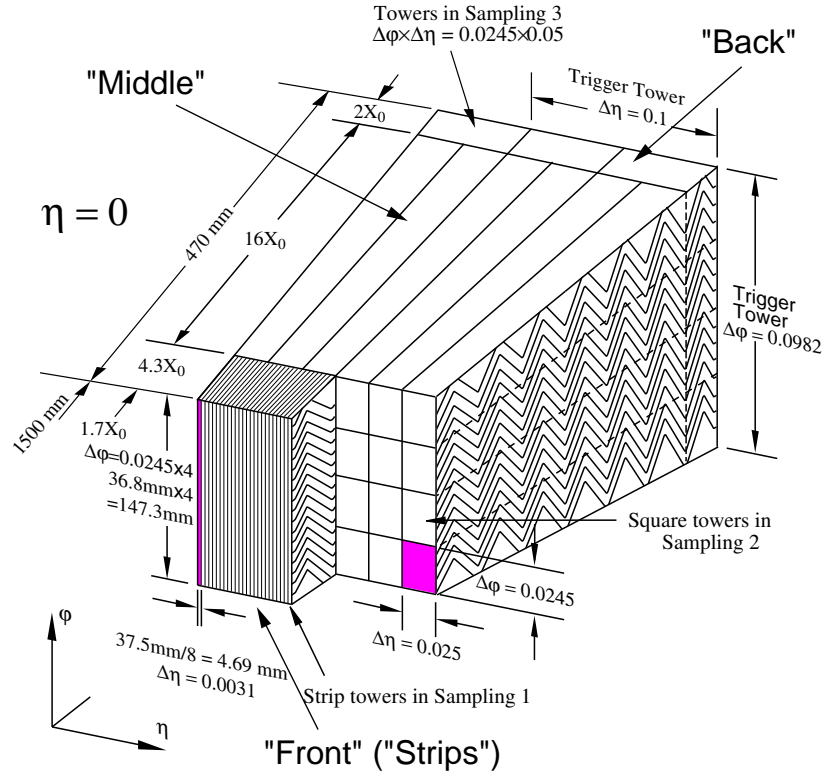


Figure 3.5: Structure of the accordion part of the LAr Calorimeter.

positioned in front of the accordion part of the calorimeter. Its granularity in the central region is $\Delta\eta \times \Delta\phi = 0.025 \times 0.1$.

The front layer (also called "strips") has a fine granularity in η and a coarser one in ϕ ($\Delta\eta \times \Delta\phi = 0.03 \times 0.1$). Its depth is from 2.4 to 4.5 X_0 . The middle sampling is the largest of the three compartments with a depth from 16.5 to 19 X_0 , the granularity is $\Delta\eta \times \Delta\phi = 0.025 \times 0.025$. The largest energy fraction of an electron shower is deposited in this layer. In terms of η one middle cell covers eight front cells. The depth of the back sampling is from 1.4 to 7 X_0 . The back sampling is important for the estimation of the energy lost in the dead material (e.g., cryostat walls, cables) between the liquid argon and the Tile calorimeter for hadronic showers and can be used to estimate the energy leaking out behind the calorimeter.

In fig. 3.6 the structure of the electrodes of the liquid argon calorimeter is shown. The absorber which serves as ground electrode is 2.16 mm thick. It is made of a lead core with a thickness of 1.5 mm and 1.1 mm for pseudorapidities $\eta \leq 0.8$ and $\eta > 0.8$ respectively and a steel cover. The length of the folds is increased and the angles are reduced with larger radii, such that the gap size is kept constant over the full wheel.

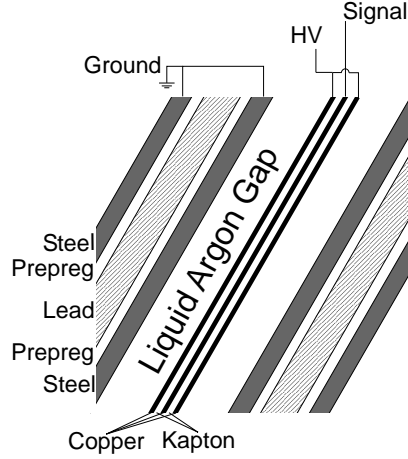


Figure 3.6: Sandwich structure of the liquid argon calorimeter electrodes (not to scale).

The anode is located in the center of the cell, it consists of two copper layers which supply the high-voltage. A third one in their middle, separated (and insulated) from the high-voltage by slices of Kapton is the signal layer.

The gaps between the electrodes are filled with liquid argon. Electrons are produced by ionization of charged particles passing through. They drift towards the anode where their charge is collected and the signal is induced by capacitive coupling.

The end-cap calorimeter uses also accordion shaped electrodes; the granularity of the cells is coarser than in the central region.

In the hadronic end-cap calorimeter (HEC) copper is used as absorber instead of lead. It consists of two wheels with plates as electrodes instead of the accordion shape.

The forward calorimeter (FCAL) covers the forward region ($3.0 < \eta < 4.9$) and its front face has a distance of about 4.7 m to the interaction point. The FCAL is integrated into the end-cap cryostat and consists of three sections, where the first is made out of copper and for the other two tungsten is used as passive material. The high density material tungsten has been chosen to reduce pile-up. The structure of the FCAL is a metal matrix with tubes which contain concentrically positioned rods. The gap between tubes and rods is filled with LAr. The FCAL contains in total (in all three sections) about 30000 tubes and rods which are grouped together to 11288 channels for both end-caps. The metal matrix is grounded and the rods are at high voltage. A big challenge for this calorimeter is the expected high amount of radiation it has to cope with.

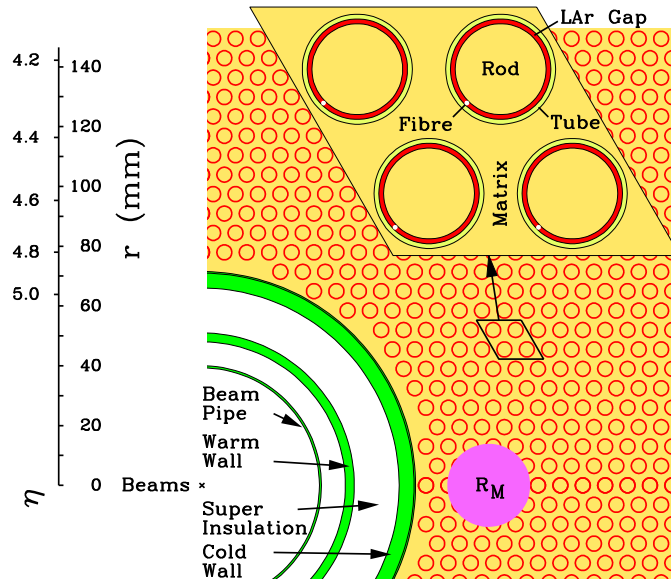


Figure 3.7: Schematic of the structure of the forward calorimeter (FCAL). The FCAL is built around the beam line. It consists a metal matrix with tubes which contain rods. The space between tubes and rods is filled with LAr.

3.3.2 Tile Calorimeter

The Tile Calorimeter (TileCal) is a sampling calorimeter for the energy measurement of hadron showers. The absorber is a massive steel structure with pockets which contain scintillator tiles for signal readout. Two wavelength shifting fibers are connected radially along each scintillator on the outside of the module faces. Each fiber is connected to a photomultiplier (PMT) for the detection of the photons created by scintillation (Fig. 3.8).

The two fibers for each scintillator provide efficient light collection and a redundancy which might be of use considering the large expected period of operation. The Tile Calorimeter consists of a central part which covers the pseudorapidity region of $|\eta| < 1.0$ and an so-called ‘extended barrel’ part on both sides covering $0.8 < |\eta| < 1.7$. A 60 cm wide gap between central region and extended barrel serves to route the cables from the Inner Detector and the LAr Calorimeter to the outside (Fig. 3.9). Scintillators located inside the gap give an estimate of the amount of energy deposited in that volume and can be exploited to estimate the amount of energy deposited in the dead material.

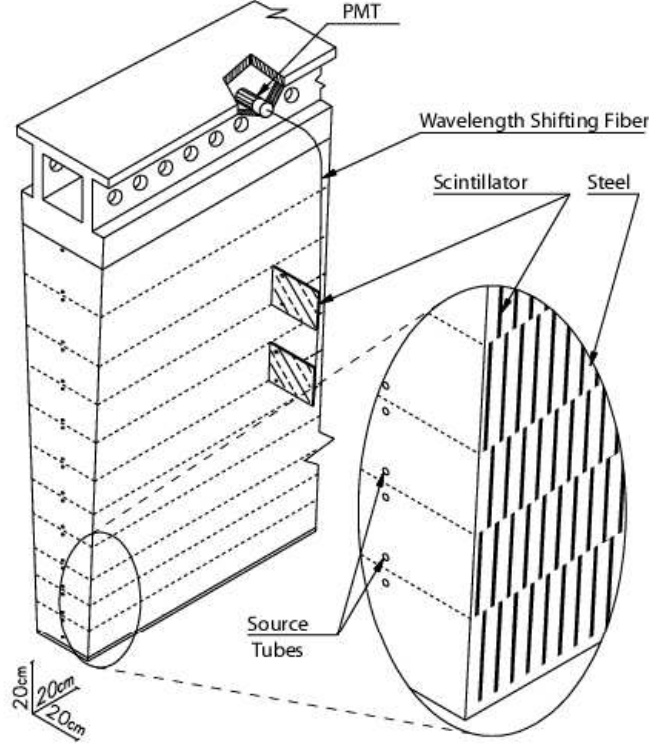


Figure 3.8: Structure of a module of the Tile Calorimeter. Shown is the steel structure with scintillator tiles which are connected via a wavelength shifting fiber with the PMTs. The Cs source for calibration is moved through tubes marked with *source tubes* in the schematic.

The requirements for the design of the Tile Calorimeter have been:

- fast readout system; TileCal is part of the level 1 trigger system (LVL1).
- dynamic range from the MeV to the TeV scale (from the signals in the cells caused by muon signals to highly energetic jets)
- thickness of at least 11 nuclear interaction lengths at $\eta = 0$ (including all material before the TileCal) to reduce leakage (important for a good E_T^{miss} measurement).

The intrinsic resolution for jets after correction for invisible energy losses of hadrons in the calorimeter and energy losses in the dead material for $|\eta| < 3$ should be according to the ATLAS Tile Calorimeter technical design report [4]:

$$\frac{\Delta E}{E} = \frac{50\%}{\sqrt{E}} \oplus 3\% \quad (3.1)$$

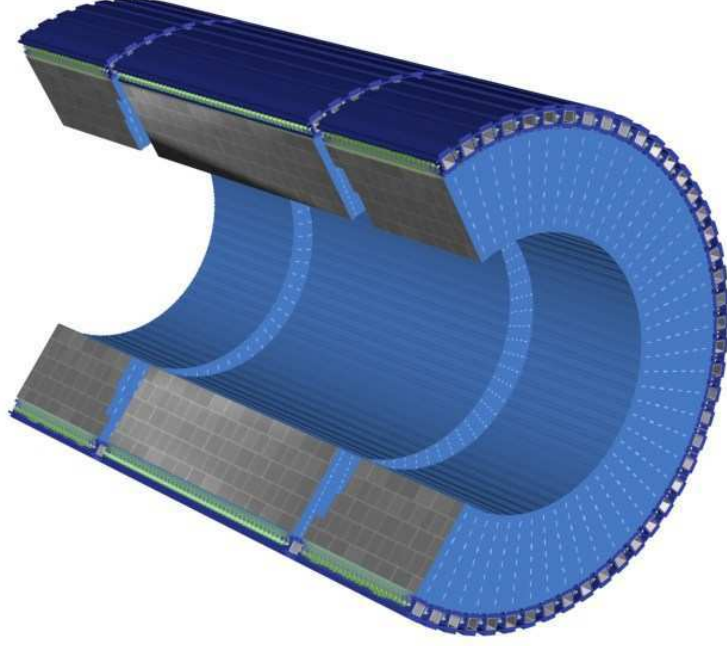


Figure 3.9: Structure of the Tile Calorimeter, central region (‘barrel’) and extended barrel.

The Tile Calorimeter is divided into three radial compartments (samples), called A, BC and D. The length of Tile A, BC and D in units of nuclear interaction length (λ_{int}) at $\eta = 0.4$ is about 1.6, 4.6 and 2.1 respectively. Tile D is used for the estimation of longitudinal leakage.

The granularity of the cells in the samples A and BC of the Tile Calorimeter is $\Delta\eta \times \Delta\phi = 0.1 \times 0.1$ and for the last radial compartment D (the tail catcher) it is $\Delta\eta \times \Delta\phi = 0.2 \times 0.1$. Unlike the calorimeters of earlier experiments using scintillator tiles, in TileCal they are positioned perpendicular to the colliding beam, but staggered in depth. This facilitates the construction of the readout of the light and thus provides a high homogeneity, but introduces a variation of the sampling fraction as a function of the impact position of the particle. The read-out electronics has two gains: *high* for signals up to 10 GeV per PMT and *low* for signals up to 1 TeV.

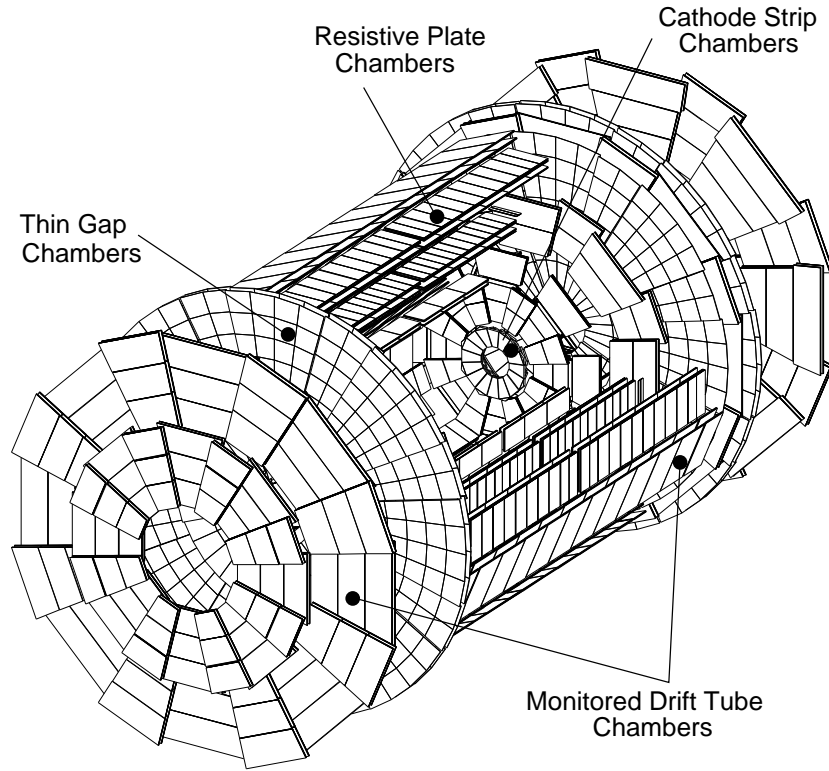


Figure 3.10: Sketch of the Muon system. Shown are the different types of muon detectors and the regions of their use.

3.4 Muon system

The Muon System is the outermost detector of ATLAS. Its role is the identification and reconstruction of muon tracks and the measurement of their mass and momenta. The detector consists of a large air-core toroidal magnet system (a toroid in the central region and two smaller end-cap toroids) with a magnetic field of about 0.5 T and several different chambers. Monitored drift tube (MDT) chambers are used for the high precision measurement of the muon trajectory, resistive plate chambers (RPC) are used for triggering and cathode strip chambers (CSC) cope with the higher counting rates in the end-cap region.

Requirements for the muon system are

- momentum and mass resolutions have to be at the 1% level
- position resolution of $50\ \mu\text{m}$
- track matching with Inner Detector
- bunch crossing identification
- radiation hardness

To be able to reconstruct the trajectory of the muons, three points are necessary. Hence the muon system consists of three layers of precision measurement chambers. The magnets provide a field which is mostly orthogonal to the muon trajectories. In the central region $|\eta| \leq 1.0$ the magnetic field is provided by the central toroid, in the end-cap region $|\eta| \leq 1.0$ this is done by the end-cap toroids. In the transition region $1.0 \leq |\eta| \leq 1.4$ the field is provided by both.

4 Interaction of particles with matter

In this chapter an overview of the physical effects which are most important for calorimetry in high energy physics is given. Particles which transverse matter lose energy due to interactions with the atoms and molecules of the material. Energy is deposited via a multitude of effects. An impinging particle with a sufficiently high energy gives rise to a cascade of particles. The number of particles which is created depends roughly on the energy of the impinging particle. The low-energetic particles produced in the cascade deposit their energy via ionization in the calorimeter. Hence, the energy of the incident particle is completely absorbed in the calorimeter, provided it is large enough to contain the whole cascade. The cascades are called “electromagnetic showers” if they are created by pair-production and bremsstrahlung or “hadronic showers” if they are created by strong interactions. In hadronic showers a large fraction (about 30%) of the energy is deposited such, that it can not be measured with the calorimeter. This energy is called “invisible energy” (see sec. 4.4.2). On the basis of simulations in Pb, Al and Fe, the energy deposition along the shower axis of hadronic showers is shown on the average and for a single shower.

4.1 Energy loss of charged particles

The main reason for the energy loss of moderately relativistic particles which are not electrons are ionization and atomic excitation. With $\beta = v/c$ and $\gamma = 1/\sqrt{1 - \beta^2}$ the energy loss $-dE/dx$ is described by the Bethe-Bloch formula:

$$-\frac{dE}{dx} = Kz^2 \frac{Z}{A} \frac{1}{\beta^2} \left[\frac{1}{2} \ln \frac{2m_e c^2 \beta^2 \gamma^2 T_{\max}}{I^2} - \beta^2 - \frac{\delta(\beta\gamma)}{2} \right]. \quad (4.1)$$

where $K = 4\pi N_A r_e^2 m_e c^2$ with r_e being the classical electron radius $e^2/4\pi\epsilon_0 m_e c^2$ and m_e the electron mass, z is the charge of the incident particle, Z and A are the atomic number and the atomic mass of the material, I is the mean excitation energy, T_{\max} is the maximum kinetic energy which can be passed on to a free electron in a single collision and $\delta(\beta\gamma)$ is a density effect correction.

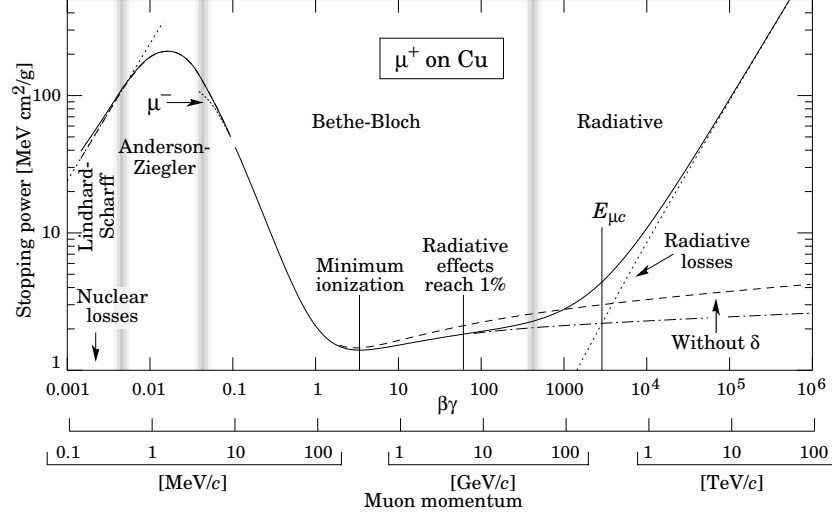


Figure 4.1: Energy loss of muons in copper as a function of $\beta\gamma$. Different approximations are indicated by vertical bands. The Bethe-Bloch parametrization describes the energy loss of muons from $\beta\gamma$ about 0.05 to about 500 [5].

The energy loss of muons in copper over a wide range of energies is shown in fig. 4.1. Within the energy region of about 6 MeV to 6 GeV (which depends on the mass of the particle and the atomic number of the material), the energy loss of pions in a material is well described with an accuracy of about 1% by Bethe-Bloch [5]. For energies below that regions, several corrections have to be applied while for higher energies radiative effects get significant. The curve has a broad minimum at $\beta\gamma$ of about 3.0 for materials with high Z and 3.5 for materials with low Z . Particles where the energy loss is minimal are called *minimally ionizing particles* (mips). Since the energy loss for high energetic particles is close to the one of mips, in practice all particles can be considered as mips.

4.2 Development of electromagnetic showers

The mechanism of how electrons and photons interact with matter depend on their energy. In the low energy region electrons lose their energy through ionization and thermal excitation at collisions with atoms and molecules of the material (see fig. 4.2). Compton scattering and the photoelectric effect are the main sources for energy loss of photons (see fig. 4.2b).

Above energies of about 10 MeV the Bremsstrahlung processes where a photon is emitted by an electron in the presence of an external field becomes the main mechanism for electrons to lose energy while the dominant photon interaction cross section is pair

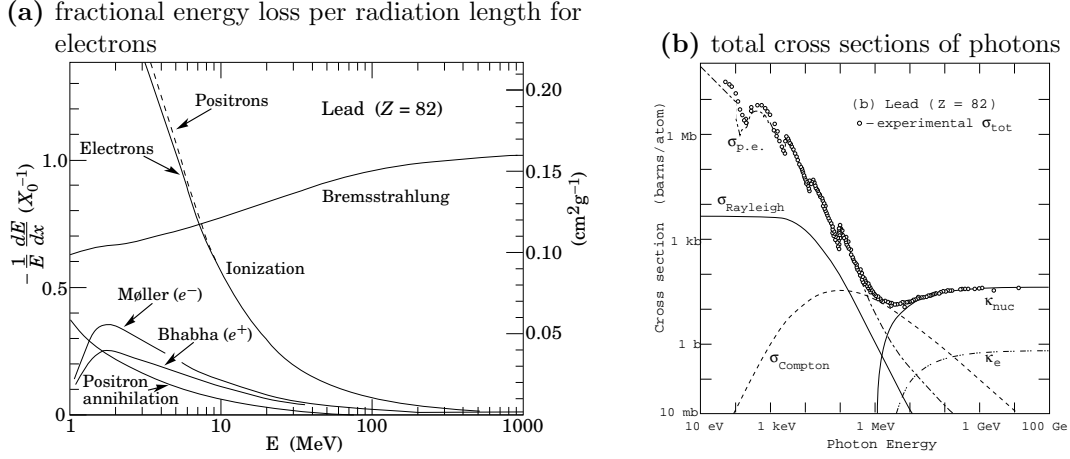


Figure 4.2: Interactions of electrons and photons with matter as a function of their energy. In fig. (a) the fractional energy loss per radiation length is shown as a function of the electron energy (for Lead). The radiation length of Lead is $X_0(\text{Pb}) = 6.37 \text{ g/cm}^2$. Fig. (b) shows the total cross sections of photons in Lead depending on their energy. $\sigma_{\text{e.p.}}$ is the atomic photo-electric effect, σ_{Rayleigh} and σ_{Compton} are the (coherent) Rayleigh scattering and the (incoherent) Compton scattering, κ_{nuc} and κ_e are the pair production in the nuclear field and the electron field and finally $\sigma_{g.d.r.}$ are photonuclear interactions in which the target nucleus is broken up (most important: Giant Dipole Resonance). Both figures have been taken from [5].

production, i.e. the photon converts into an electron-positron pair. The contribution of bremsstrahlung and pair-production rise until about 1 GeV where the cross sections for both processes become roughly energy independent.

Photons with sufficiently high energy interacting with matter will produce secondary electrons and positrons by pair production; Electrons will produce secondary photons by bremsstrahlung. Those secondary particles themselves will produce by the same processes further particles in turn such that a cascade (shower) of particles builds up. The energy of each newly created particles is lower than its primary particle. The number of particles in the shower multiplies until the energy of the electron component falls below the so called critical energy ϵ which for solids (gases) is given by

$$\epsilon = \frac{610 \text{ (710) MeV}}{Z + 1.24 \text{ (0.92)}} \quad (4.2)$$

(Z is the atomic number) where the energy losses due to ionization of the electrons becomes equal to the losses caused by bremsstrahlung. From that point on ionization and excitation become the main processes. In this last stage, the energy of the particles

in the shower is rather dissipated than used to create further particles [6].

The properties of electromagnetic showers can be described in terms of the radiation length X_0 . The energy lost by particles can be characterized as:

$$\langle E(x) \rangle = \langle E_0 e^{-x/X_0} \rangle \quad (4.3)$$

An electron of the energy E_0 which travels a distance $x = X_0$ in a material will reduce its energy on average to $1/e E_0$. The radiation length can be parametrized (eq. 4.4) and depends on the atomic number Z and weight A of the material:

$$X_0(\text{g/cm}^2) = \frac{716 \text{ g cm}^{-2} A}{Z (Z + 1) \ln(287/\sqrt{Z})}. \quad (4.4)$$

For the reduction of the intensity of photons a similar quantity can be defined to be $X'_0 = \frac{9}{7} X_0$. The photons loose their energy mainly through pair production. In terms of X_0 the development of showers can be expressed independent from the material. The mean longitudinal shower development can be phenomenologically described by the Longo-Sestili formula [7]:

$$\frac{dE}{dt} = E_0 b \frac{(bt)^{a-1} e^{-bt}}{\Gamma(a)} \quad (4.5)$$

where $t = x/X_0$ is the depth inside the material expressed in radiation lengths and a and b are parameters which depend on the type of incident particle (electron/positron or photon).

In sampling calorimeters where active layers measuring the energy loss of the passing particles alternate with passive layers (absorbers), only a fraction of the shower energy is deposited within the active layers. The sharing of the deposited energy between the active and the passive material can be expressed with the *sampling fraction*. The sampling fraction can be defined by the energy deposited in the active layers divided by the energy deposited in both, active and passive layers:

$$F_{\text{sampling}} = \frac{\langle E_{\text{active}} \rangle}{\langle E_{\text{active}} + E_{\text{passive}} \rangle} \quad (4.6)$$

where E_{active} (E_{passive}) is the energy deposited by a particle in the active (passive) part of the calorimeter. The relative energy loss in the active part of the calorimeter and in the absorber is slightly different for muons and electrons, since in an electron shower a

lot of low energy photons are produced which have a larger probability to interact in the next absorber than in the active material (Z -dependence of Compton scattering and photo effect) and produced low energy electrons do not reach the active part.

Often the sampling fraction is defined with respect to minimum ionizing particles (mip):

$$F_{\text{sampling}}^{(\text{mip})} = \frac{\langle E_{\text{active}}^{(\text{mip})} \rangle}{\langle E_{\text{active}}^{(\text{mip})} + E_{\text{passive}}^{(\text{mip})} \rangle} . \quad (4.7)$$

The sampling fraction can be estimated using muons with different energies and unfolding the *mip* part of their signal distributions [8].

The sampling fraction, referred to in this thesis, is defined by the energy deposition of electrons in active material versus the total deposited energy.

$$F_{\text{sampling}}^{(\text{e})} = \frac{\langle E_{\text{active}}^{(\text{e})} \rangle}{\langle E_{\text{active}}^{(\text{e})} + E_{\text{passive}}^{(\text{e})} \rangle} . \quad (4.8)$$

4.3 Energy resolution of sampling calorimeters for electromagnetic showers

An electromagnetic shower deposits energy in the detector mainly through ionization and atomic excitation by charged particles. Each of the particles contributes an ionizing track which can be summed up to $T_0 = \sum_{i=0}^{N_0} t_i \propto X_0 N_0$ where N_0 is the number of charged particles in the shower, t_i are the particles' ionization tracks and X_0 is the radiation length. T_0 is proportional to N_0 which itself depends on the energy of the incident particle E_0 ($N_0 = E_0/\epsilon$). As a shower develops stochastically, we can derive the energy resolution from statistical arguments by:

$$\sigma(E) \propto \sqrt{T_0} \propto \sqrt{E_0}, \quad (4.9)$$

which leads to

$$\frac{\sigma(E)}{E} \propto \frac{1}{\sqrt{E_0}} . \quad (4.10)$$

This contribution to the energy resolution is called the *stochastic term*.

The energy resolution may be influenced by electronic noise of the readout chain. This

quantity depends largely on how the signal is measured. The noise contribution behaves like $O(1/E)$ and becomes important at low energies.

There are additional contributions to the energy resolution which do not depend directly on the particle energy. Cell shapes, cracks and other non-uniformities of the detector will cause a change of the calorimeter response depending on the impact point of the particle and location of the shower (lateral and longitudinal leakage, upstream energy losses, dead material losses). Effects such as temperature gradients, radiation damage or imperfections in the readout system will affect as well the measurement. Some of these influences can be reduced by the design and by the construction, others can be corrected by the calibration procedure. The remaining part adds a constant term to the resolution.

The resolution function can now be written as:

$$\frac{\sigma}{E} = \frac{s}{\sqrt{E}} \oplus \frac{n}{E} \oplus c \quad (4.11)$$

where the symbol \oplus denotes a quadratic sum. The first term is the *stochastic term*, the second denotes the *noise term* and the third one is the *constant term* [6, 8].

4.4 Development of hadronic showers

An impinging hadron gives rise to a cascade mostly through strong interactions with the nuclei of matter.

In each interaction $hN \rightarrow X$ a sizable amount of the hadron momentum is transferred to the secondary hadrons. In general a significant amount of energy is used for processes such as spallation, excitation, evaporation of nuclei, etc. This results in a number of particles with energies at the MeV scale. A part of this energy (e.g. energy which has been used to break up nuclei, soft neutrons) cannot be measured with the calorimeter and is therefore called “invisible energy”. Because of the dominance of strong interactions of hadrons with nuclei, the shower dimensions of the hadronic part of the shower are described by the nuclear interaction length λ_I [6, 8]. The nuclear interaction length is defined as the average distance a high-energy hadron can travel inside a medium before a nuclear interaction occurs. The probability for a particle traversing the distance x before undergoing an interaction equals:

$$P = \exp(-x/\lambda_I) \quad (4.12)$$

The relation between the nuclear interaction length λ_I and the total cross section σ_{tot} is given by

$$\sigma_{\text{tot}} = \frac{A}{N_A \lambda_I}, \quad (4.13)$$

where A is the atomic weight and N_A the Avogadro number.

For large values of σ_{tot} and assuming an opaque, spherical nucleus the total cross-section is proportional to the square of the radius of the nucleus: $\sigma_{\text{tot}} \approx O(r^2)$. A nucleus with the atomic weight A has a volume $V \propto r^3 \approx O(A)$. Thus, the radius r is proportional to $O(A^{1/3})$. That gives for the total cross-section $\sigma_{\text{tot}} \approx O(A^{2/3})$. With eq. 4.13 the nuclear interaction length can be derived $\lambda_I \approx O(A^{1/3})$ [8].

The cross section of an interaction of a projectile with a nucleon depends as well on the size of the projectile. A pion is about 20% smaller than a proton. The total cross sections for fixed-target pp and πp interactions at 100 GeV are ~ 38 mb and ~ 24 mb. That leads to an interaction length which is about $\sim 20\%$ larger for pions than for protons [8, 9].

Strong interactions are charge-independent and hence charged and neutral pions are equally produced. Thus, the probability for the creation of π^+, π^- and π^0 will be about the same. Hence, on average approximately one third of the created pions—typically carrying one fourth of the energy of the primary particle (since other particles than π^\pm and π^0 are created as well)—will be neutral. Those will decay immediately (before having a chance to interact) into two photons ($\pi^0 \rightarrow \gamma\gamma$). The photons will give rise to electromagnetic showers as described in section 4.2.

The energy of a hadron shower which is moved to “electromagnetic” energy via π_0 -decay is typically found within a narrow core of the shower. The energy deposited by the hadronic part is deposited mainly by low-energy particles ($\lesssim 1$ GeV). They build a surrounding halo whose energy and particle type distributions are approximately independent from the energy and type of the impinging hadron [9, 10].

We can assume a simple picture of hadronic showers where an incoming hadron starts a cascade of high energy collisions. The average fraction of the energy which is moved to the electromagnetic sector due to the creation of π^0 s is called f_{EM} and the average fraction which remains hadronic f_{H} where $f_{\text{H}} = 1 - f_{\text{EM}}$. These two sectors can now be treated independently. Within a calorimeter the signal of an electromagnetic (hadronic) shower can be measured with an efficiency η_{EM} (η_{H}). An incoming pion with the energy

E will deposit on the average an energy $f_{\text{EM}}E + f_{\text{H}}E$ for which the part

$$E_{\pi}^{\text{vis}} = \eta_{\text{EM}}f_{\text{EM}}E + \eta_{\text{H}}f_{\text{H}}E \quad (4.14)$$

can be measured in the calorimeter. This energy is called “visible” energy. According to Groom et al. [10] the hadronic fraction can be described with:

$$f_{\text{H}} = \left(\frac{E}{E_0} \right)^{m-1}, \quad (4.15)$$

where $m \approx 0.83$ and $E_0 \approx 1$ GeV depending slightly on the material. The value m is related to the number of fast hadrons typically created in a hadronic collision and the fraction of energy which is transferred to the electromagnetic sector by π^0 's. Below the cutoff energy E_0 hadronic production stops to be significant. At higher energies of the incident particle, more secondary pions with energies above E_0 are created within the shower. This increases the number of pions strongly interacting with the nuclei of the calorimeter material which leads to a rise of the electromagnetic fraction.

A value which is interesting for calorimetry is the ratio between the signal created by an electromagnetic shower (induced by an electron or a photon) and by a pion-induced shower. This ratio is called e/π and can be estimated as follows:

$$\left(\frac{e}{\pi} \right)^{-1} = \frac{E_{\pi}^{\text{vis}}}{E_e^{\text{vis}}} = 1 - \left(1 - \frac{\eta_{\text{H}}}{\eta_{\text{EM}}} \right) \left(\frac{E}{E_0} \right)^{m-1}, \quad (4.16)$$

where the signal of a charged pion in the calorimeter E_{π}^{vis} is given by eq. 4.14 and $E_e^{\text{vis}} = \eta_{\text{EM}}E$ is the signal created by an incident electron or photon [10]. Eq. 4.16 expresses that the relative pion response rises with increasing energy, since the electromagnetic compound increases with higher energy.

Qualitative differences can be seen between the showers created by impinging protons compared to pions. When protons and neutrons interact strongly with nuclei the baryon number has to be conserved. As a result, at a collision of a proton with an atomic nuclei one of the secondaries has to be a baryon (e.g. proton, neutron). This baryon will be typically the leading particle and thus carry a large fraction of the energy transferred from the primary particle to the secondaries. The same behavior is found in subsequent interactions as well, which effectively reduces the fraction of energy which can be used for π^0 -production. As a result, the electromagnetic fraction of proton-induced showers is on average smaller than of π -induced showers.

This behavior results in an on average higher signal of pion-induced showers in the calorimeter compared to proton-induced ones. Pion-showers have larger fluctuations in terms of visible energy from event to event which leads to a coarser resolution. With higher energy of the impinging particle, the differences between cascades induced by pions or by protons become smaller. This can be attributed to a decrease of the energy fraction which is carried by the leading particle compared to the other secondaries when the energy rises [8]. Proton showers are typically wider and the shape of the distribution of their total deposited energy is more Gaussian. In contrast, pion-induced showers are narrower, start later, penetrate more deeply and their line shape is asymmetric [9]. Those differences of the properties between proton and pion induced showers have been measured with the ATLAS Tile Calorimeter Test Beam 2002 [11]. Hadron showers can be parametrized using the formula suggested by Bock et al. [12].

4.4.1 Energy measurement of hadronic showers

Due to the complex behavior of hadronic and nuclear processes and the large fluctuations between the processes the measurement of hadronic showers is more complicated than of electromagnetic ones.

4.4.2 Visible, invisible and escaped energy

Particles deposit energy in matter through a large number of physical effects. Since in ATLAS the deposited energy is measured by collecting the charge produced by ionization (liquid argon calorimeter) or by collecting the scintillation light (Tile Calorimeter) only energy deposits caused by those effects can be measured. They are therefore called “visible energy” (E_{vis}). On the other hand, effects such as nuclear excitation or spallation lead to energy deposits which can not be measured in the calorimeters and is therefore called “invisible energy” (E_{inv}). Of those processes, spallation is the one with the highest cross-section when a high-energy hadron impinges on a nucleus. The hadron collides with the nucleons and causes a fast intranuclear cascade. If the transferred energy is sufficiently high, particles such as pions may be created of which some will escape. This is followed by an evaporation stage where particles—typically free nucleons—are evaporated until the excitation energy is below the binding energy of one nucleon. The remaining energy is emitted in form of γ -rays. The energy which is used to release nucleons from the nuclei can not be measured and is therefore invisible. The amount of invisible energy fluctuates strongly.

A third contribution besides visible and invisible energy is the so-called “escaped energy” E_{esc} . The energy of secondary particles which leave the simulated spatial region (“world volume”) is tagged as “escaped” at the position where the secondary particle initially has been created. For instance a neutrino which has been created in a cell in the liquid argon calorimeter and subsequently has left the simulated space is accounted for escaped energy in the cell where it has been created. Visible, invisible and escaped energy sum up to the total deposited energy $E_{\text{tot}} = E_{\text{vis}} + E_{\text{inv}} + E_{\text{esc}}$.

In the simulation it is possible to distinguish for the visible energy if the energy is deposited by hadrons ($E_{\text{had,vis}}$) or leptons or photons¹ ($E_{\text{EM,vis}}$; “EM” for “electromagnetic”). Hence, the total deposited energy is given by:

$$E_{\text{tot}} = E_{\text{EM,vis}} + E_{\text{had,vis}} + E_{\text{inv}} + E_{\text{esc}} \quad (4.17)$$

Comparison of simulated shower shapes for Pb, Al, Fe

To illustrate the behavior of hadron showers in different materials, simulations of 10 GeV pions have been generated. Uniform blocks of aluminum, iron and lead have been simulated. Their size has been chosen, such that the whole hadron shower - except neutrinos and muons - was contained. The source for the simulated particles has been placed in the center of the block to avoid boundary effects where the incident particle enters the block. For each of the three materials 1000 events have been generated to average over the event-to-event-fluctuations. The atomic numbers (Z) of lead, iron and aluminum are 82, 26 and 13, respectively. In Tab. 4.1 some important properties of materials used in the calorimeters in the ATLAS barrel region are compiled.

The profiles of the distribution of the mean total deposited energy (E_{tot}) of hadron showers along the shower axis in the three different materials are shown in fig. 4.3a. The profile in lead starts with a steep rise until it reaches the maximum at about $0.8 \lambda_{\text{int}}$. It falls then slowly until the total energy of the shower has been deposited at about $10 \lambda_{\text{int}}$. The profile of iron rises less steep than the profile of lead and reaches the peak at about $1 \lambda_{\text{int}}$. It falls then—similar to the profile of lead—slowly until all energy has been deposited. Aluminum, the lightest of the three materials behaves similar to lead and iron, but its rise is flatter and the peak is at about $1.2 \lambda_{\text{int}}$. The tail of the profile of aluminum is higher than of lead and iron.

¹In the simulation, for technical reasons, the energy of photons of which the absorption length is shorter than the user defined range cut (in ATLAS: $100 \mu\text{m}$) is deposited at the current position of the photon.

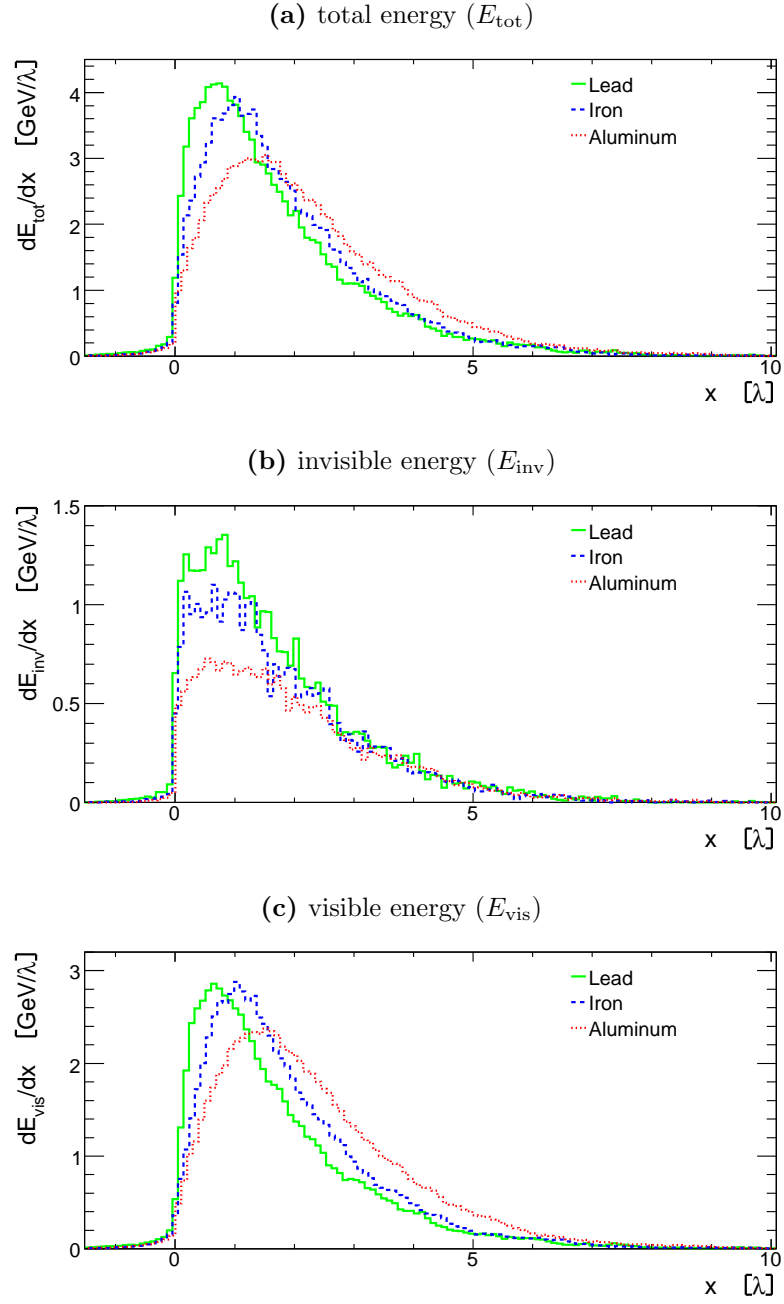


Figure 4.3: Longitudinal profile (in units of interaction length) of the mean total (a), the invisibly (b) and visibly (c) deposited energy of a 10 GeV π -shower in lead, iron and aluminum (1000 events).

Material	$dE/dx _{\min}$ (MeV cm ² g ⁻¹)	E_C (critical energy for e^-) (MeV)	λ_I (g cm ⁻²)	X_0 (g cm ⁻²)
Al	1.615	42.55	107.2	24.01
Liquid Ar	1.508	38.13	119.7	19.55
Fe	1.451	21.81	132.1	13.84
Pb	1.122	7.79	199.6	6.37
Polystyrene ([C ₆ H ₅ CHCH ₂] _n)	1.936	93.11	81.7	43.79

Table 4.1: Atomic and nuclear properties for selected materials. The main materials which are used in the ATLAS barrel calorimeter are listed. Liquid Ar and Pb are used in the electromagnetic calorimeter and Al is the main material between the electromagnetic and the hadronic calorimeter. Fe is the passive material in the hadronic calorimeter and the scintillators are made of Polystyrene. The values for $dE/dx|_{\min}$ show the minimum energy deposition along the particle trajectory due to ionization, E_C is the critical energy for e^- , λ_I is the nuclear interaction length in the material and X_0 the radiation length. The values are taken from Yao et al. [5].

In simulation, it is possible to distinguish between the different ways of how the energy is deposited. In fig. 4.3b the profile of the distribution of invisibly deposited energy is shown. Large amounts of invisible energy are created in strong interactions of hadrons with nuclei. As the average distance until hadrons interact strongly is given by the nuclear interaction length, and the longitudinal profiles of the three materials are drawn in units thereof, all three peaks are approximately at the same place. The average amount of invisible energy deposited at a strong interaction depends on the number of nucleons of the nucleus the hadron is interacting with. In the aluminum block the least amount energy is deposited invisibly and in lead the largest. Iron lies in between the two.

Fig. 4.3c shows the profile of the distribution of the energy which is deposited visibly. This fraction of energy can be further divided into the energy which is deposited by the electromagnetic (e.g. electrons, positrons, photons) part of the shower (Fig. 4.4a) and by ionization through hadrons (Fig. 4.4b).

The comparisons of the energy deposits by pions in the three different materials (Pb, Fe, Al) lead to the conclusion, that the qualitative average behavior of hadron showers in different materials expressed in units of interaction length is similar, but not equal.

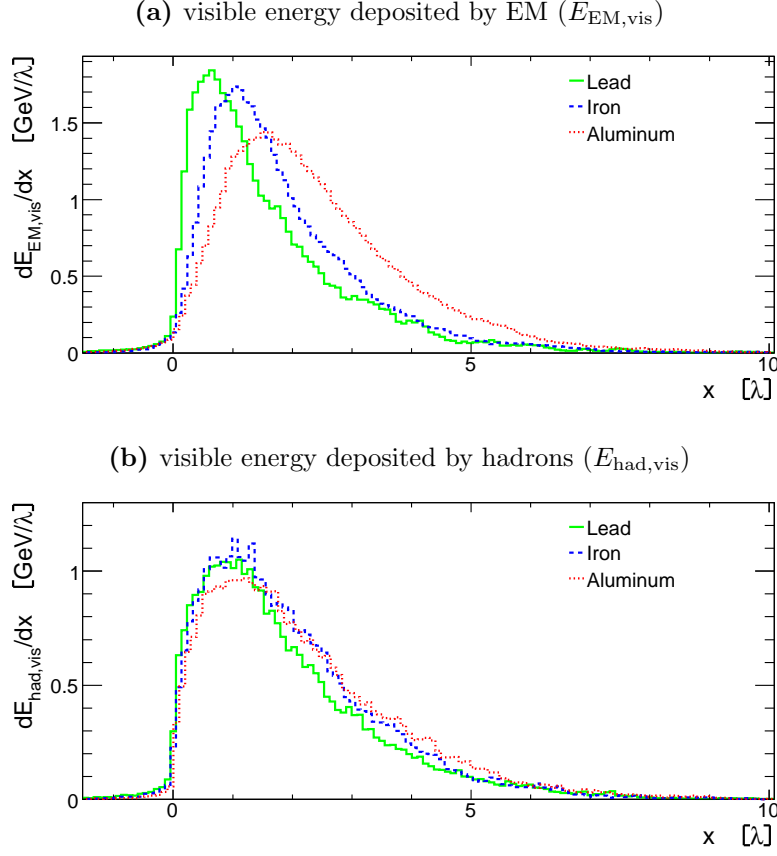


Figure 4.4: Longitudinal profile (in units of interaction length) of the visibly, electromagnetically (a) (by electrons, positrons, photons) and deposited by hadrons via ionization (b) deposited energy of a 10 GeV π -shower in lead, iron and aluminum.

Shower shape of a single pion event

To give an example of the large fluctuations of a pion, in fig. 4.5 the development of the shower of a single 10 GeV π^+ in Aluminum, created at $x = 0$ is shown. The kinetic energy of each particle entering a bin in the dimension x is summed up to the histogram for the respective particle type. From $x = 0$ towards positive x , first, the largest amount of kinetic energy is carried by π^+ particles which is obvious as the incoming π^+ carries all of the energy. The kinetic energy of the pion decreases due to ionization of the material it passes through. At about $x = 1600$ mm, a strong interaction of the incoming π^+ with a nucleus occurs.

The figure in the middle shows the number of particles regardless of their energy (only particles with a path length larger than $100 \mu\text{m}$ —the ATLAS range cut—are considered). Photons are created the most, followed by neutrons which are to a large extent of a low

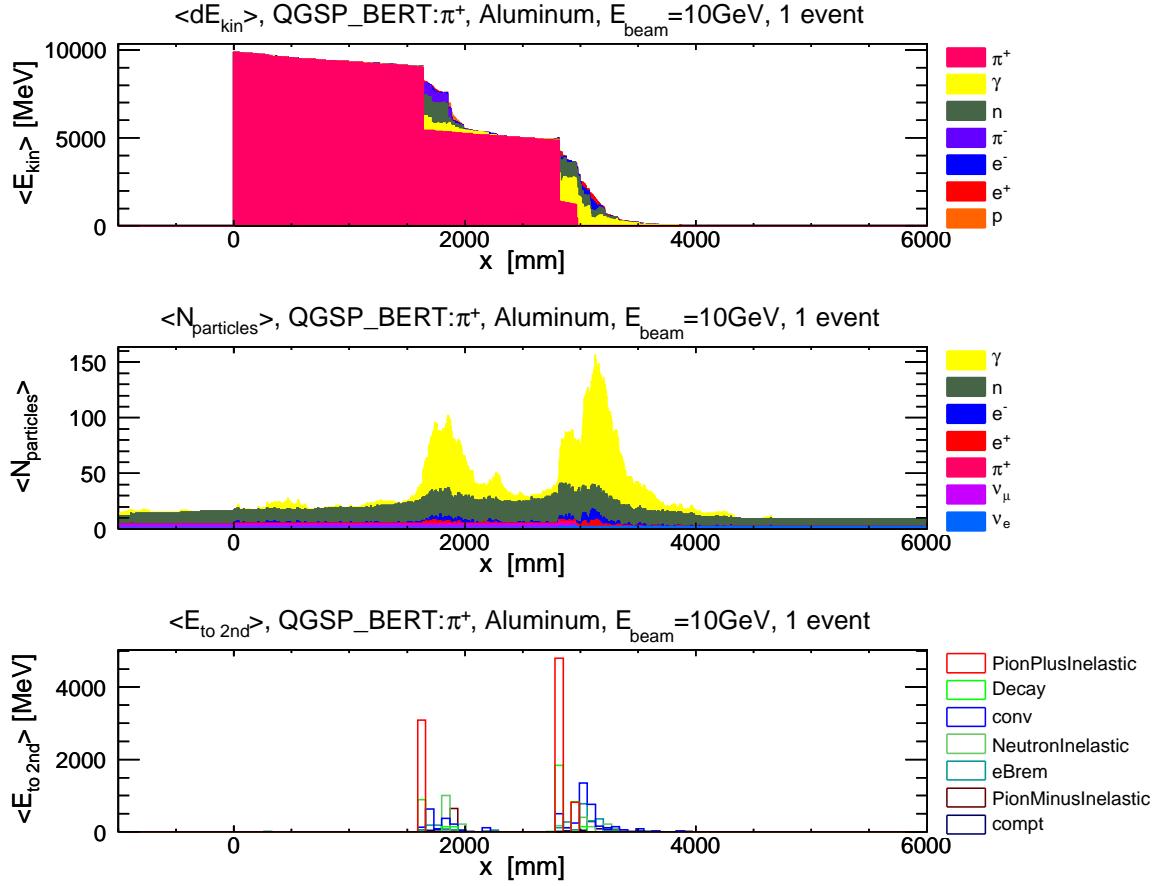


Figure 4.5: Shower shape of one 10 GeV π^+ simulated with GEANT4.7 QGSP_BERT in a block of Aluminum. The figure on the top shows the average kinetic energies of the particles of the shower as a function of depth in the material with the particle originating at $x = 0$. Only particles whose sum of kinetic energies exceed at some position x a threshold of 200 MeV are shown. The energy drawn for each particle type and each bin is the kinetic energy of all particles of that type entering the bin of the histogram. Particles which decay or interact before having passed to the next bin (such as π^0) are therefore not shown. The middle figure shows the number of particles as a function of depth in the material. The bottom figure shows the energy which is transferred from the primary particle to the secondary particles depending on their creating processes in GEANT4. The palettes of the figures are ordered such that the most important particle type, number and process are on the top and the least important on the bottom.

energy. Particles moving into the direction $x < 0$ are mostly albedo neutrons with a low energy.

Fig. 4.5 in the bottom shows the energy that is carried by the secondary particles created by a certain type of physical interaction. The energy is assigned to the point where

the creation process happened. At about $x = 1600$ mm a large peak due to inelastic scattering (`PionPlusInelastic`) of the pion with a nucleus can be seen. This is the same position where in the top figure a sudden decrease of the kinetic energy of the π^+ -particles can be observed: In addition a lot of neutrons and small electron shower are created. At this interaction mainly π^+ , photons, neutrons and π^- are created. A second large inelastic scattering of a pion can be seen at about $x = 2800$ mm with the same large peak in the bottom figure.

4.5 Summary

High-energy particles impinging on matter produce cascades which—provided they are fully contained in the calorimeter—deposit the total energy of the incident particle in the calorimeter, apart from a possible small fraction of “escaped” energy. In the case of hadronic showers, the amount of energy which can be measured in the calorimeter is strongly fluctuating from event to event due to the deposition of invisible energy caused by inelastic, strong interactions of hadrons with the nuclei. This leads to a much coarser energy resolution of hadronic showers compared to electromagnetic showers.

5 Implementation of models of the interaction of particles with matter in Monte Carlo Simulations

The effects influencing the shower development which have been shown in general in chapt. 4 can be simulated in detail with Monte Carlo simulations. In the simulations a large number of physical processes are implemented to model the trajectories and the energy loss of particles in matter. The energy measurement in the ATLAS calorimeters relies strongly on corrections which are derived from simulations. In sec. 9 hadronic showers produced by simulations are compared to those from data to assess the accuracy of the simulation.

In this chapter an overview of the design and functioning of the Monte Carlo based simulation tool GEANT4 [13–15] are given. The principle of interplay between geometry, movement of particles and description of their interaction with matter using processes and models is explained. Afterwards, several compilations of processes and models—the so called *physics lists*—and their properties are discussed. In the subsequent parts of this chapter, the *calibration hits* which represent the true deposited energy in the cells of the calorimeter are discussed and the definition of *invisible energy* is given. Finally, the structure of hadronic showers using different physics lists will be shown.

Monte Carlo methods (MC) are a class of computational statistical sampling techniques which have been successfully applied to a wide range of scientific problems [16,17]. The MC technique was developed by Stanislaw Ulam and John von Neumann and originally used for tracking of elementary particles (for historical remarks see appendix 10.8 on page 147). Due to the development of computers over the last decades, MC techniques can be employed even for very complex concepts. In high energy physics two widely used programs to simulate the interaction of particles with matter are GEANT4 and FLUKA [18,19]. In this thesis all simulations have been done with GEANT4¹.

¹FLUKA cannot be used directly from the ATLAS software since the geometry is treated differently to GEANT4. However, some special simulations have been carried out with the TileCal Test Beam geometry of 2002 and it has been shown, that FLUKA behaves similar to GEANT4 when in addition to the quark-gluon string model an intra-nuclear cascade model is used.

The performance, size and complexity of modern experiments in particle physics require accurate large-scale simulations. Today's high-capacity computer systems have made it possible to build up and use very detailed, but nevertheless robust simulation frameworks. The origin of GEANT4 can be backtraced to 1993 where studies have been done on available modern computing techniques at that time and how they could be applied to achieve an improvement over GEANT3 [20]. Taking GEANT3 as a benchmark and as a source for ideas the it has been started to create a simulation framework based on object-oriented technology. The resulting project, RD44, was a worldwide collaboration of many scientists and engineers. The first production release could be delivered in 1998. In 1999 the GEANT4 collaboration was founded which continues the development on the toolkit [13].

5.1 Design overview of GEANT4

For the simulation of particles passing through matter, the following key domains must be covered:

- geometry and materials
- particle interactions in matter
- tracking management
- digitization and hit management
- event and track management
- visualization and visualization framework
- user interface.

GEANT4 is programmed with the concept of a toolkit. The mentioned domains are therefore realized in an object oriented architecture with coherent interfaces. The user has to assemble his/her program using components either supplied by the GEANT4 toolkit or by him/herself (e.g. geometry description, detector specific digitization).

One of the major design goals of GEANT4 has been, to facilitate changes and extensions to the program code. By using extensively an object-oriented programming style a highly granular, customizable relation between particles and processes is built up where the models for the processes can be easily exchanged for newer or more specialized

ones. The calculation of reaction/production cross-sections can be done using formulae, parameterizations or interpolation of tabulated data separated from the generation of the final states particles. For different energies, particle types and materials alternative or complementary models are provided [13, 14].

5.2 Structure of GEANT4

5.2.1 Events

The main unit of a simulation is an event which is represented by the `G4Event` class. Before the event is processed, objects of this class contain primary particles and vertices. Afterwards they contain hits (i.e. interactions in a given material) and digitizations (the response of a part of the detector, i.e. a cell, to the hits in its volume) which were created by the simulation. There is also the possibility to record the “simulation truth” (trajectories of the simulated particles).

GEANT4 provides interfaces to external physics event generators, e.g. to calculate final states of a collision of particles at high energy. By virtue of the independence of `G4Event` from other classes, the simulation of multiple events (“pile-up”) can be done easily. By delaying digitization until after more events are processed and “adding” these, the detector output signal can be built up from overlapping signal [13].

5.2.2 Geometry

The task of the GEANT4 *geometry* module is the accurate description of the detector geometry and to provide an efficient way for the navigation of particles through it. GEANT4 uses a concept of *logical* and *physical* volumes which can be combined to a hierarchical tree structure. Logical volumes representing detector elements can be embedded in other logical volumes. Equal detector elements can be used repetitively thus resulting in reduced memory usage. Logical volumes which are spatially positioned in reference to the mother volume are called “physical” volumes. Properties independent of the position such as material and sensitive detector behaviour can be attributed to volumes. The parts of the detector which are designated to measure a signal are simulated using a logical volume that is defined to be sensitive. It is linked with a user defined class which is responsible for the calculation of the detector response (e.g. hits, digitizations) from the information given by the simulation. The readout geometry associated with a sensitive detector can be different to the geometrical structures of the detector [13].

5.2.3 Tracking and transportation

In GEANT4 the *tracking* category coordinates the selection and the call of the physical processes. Particles are not *self moving*, but *transported* by a *transportation* process. A transported particle is called a track. Transportation is treated as a physics process like particle decay or pair production. Its purpose is to control the geometrical limits of the step and to calculate the length to the next geometrical boundary.

To every particle physics processes are associated. Tracking requests a proposal for a length for the next *step* (for particles at rest, a time is proposed). Step lengths of the transportation process are determined by geometry boundary limits between different elements of the detector. The preservation of precision is the limiting factor for the step length for processes where the particle loses energy continuously. For all other processes the step length L is calculated starting with eq. 5.1 where λ is the mean free path and $P(L)$ the probability for the particle of not interacting within the distance L .

$$P(L) = \exp\left(-\int_0^L \frac{dl}{\lambda(l)}\right) = \eta \quad (5.1)$$

Taking the logarithm on both sides the following equation is obtained:

$$\int_0^L \frac{dl}{\lambda(l)} = -\ln \eta \quad (5.2)$$

For a decay process the mean free path is given by $\lambda = \gamma v \tau$ where γ is the Lorentz factor, v the velocity and τ is the mean lifetime of the particle. Inserting this into eq. 5.2 and integrating we obtain eq. 5.3:

$$\frac{l}{\gamma v \tau} = -\ln \eta . \quad (5.3)$$

For an interaction with a material, which is composed of different isotopes, λ is written as eq. 5.4:

$$\lambda = 1/(\rho \sum_i x_i \sigma_i / m_i) , \quad (5.4)$$

where ρ describes the density of the material, m_i the mass of the isotope i , x_i its mass fraction and σ_i denotes the cross-section of the process for this isotope. By inserting the

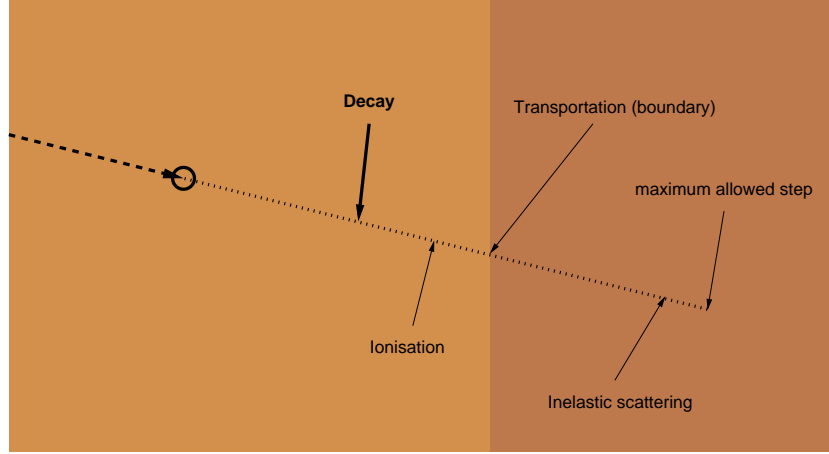


Figure 5.1: Example for the determination of the step length. Several processes proposed step lengths (indicated by the arrows on the dashed line). The process *decay* with the shortest step length is chosen to limit the step.

mean free path (eq. 5.4) for an interaction into eq. 5.2 and integrating we get:

$$L \rho \sum_i x_i \sigma_i / m_i = -\ln \eta = n_\lambda \quad . \quad (5.5)$$

For a newly produced particle a random number η is generated uniformly in the range $(0, 1)$ for each process. With the formulae eq. 5.3 and eq. 5.5 the length L until decay or interaction can be calculated.

Subsequently the tracking chooses the smallest of all suggested step lengths, or the user defined *maximum allowed step*, if it is shorter. The tracking decides which processes are to be invoked. Processes can demand to be done always (e.g. transportation, multiple scattering), if necessary. The *post step action* of the process limiting the step length is called. If the particle is not stopped or transformed due to the interaction or decay, n_λ is reduced for all processes corresponding to the step length. The whole procedure is repeated for a further step of the particle. An illustration of different step lengths proposed by different processes is shown in fig. 5.1. Several processes are proposing a step length. The decay process suggests the shortest step and is therefore selected in this example.

A track consists of many subsequent steps. New tracks created due to production of secondaries are put into a stack. When the simulation of the current track has finished, the next track is taken from the stack and simulated. GEANT4 uses three FILO (first-in-last-out) stacks called “urgent”, “waiting” and “postpone to next event” for the purpose

of prioritizing tracks. The user can decide in which stack the new track is stored. GEANT4 processes first all tracks in the "urgent" stack. Afterwards the user can decide, if some or all tracks of the "waiting" stack shall be simulated. In this way, uninteresting tracks can be suppressed which improves performance.

In the presence of electromagnetic fields, charged particles will propagate in non-linear trajectories between interactions. GEANT4 uses a selection of methods to calculate the motion of the particle. Most of these are involving Runge-Kutta integration². For magnetic fields new integration methods are used which combine Runge-Kutta and known helical solutions for uniform fields. The actual method used depends on the smoothness of the field. To determine the intersections of the particle trajectories with volume boundaries, the path is approximated by chords.

Charged particles produce even at very low kinetic energies a large quantity of soft electrons and photons, especially due to processes like bremsstrahlung and δ -ray production. For CPU performance reasons it is necessary to suppress the generation of those low energy particles in electromagnetic processes. In GEANT4, particles are not generated when their range would be less than a user-defined value. The ranges or absorption lengths of particles in function of their energy are computed once for electrons/positrons, muons, protons and antiprotons and stored in tables. Thus particle ranges can be determined very fast knowing their kinetic energy. For bremsstrahlung the range limit is based on the photons' absorption length [13].

5.3 Physics processes and models

A particular initial state, a final state and a cross-section or mean lifetime define a *process* in GEANT4. A process represents a specific physical interaction of a particle. Typically several complementary processes are assigned to a specific particle type, some within a certain energy range only, some for all energies. The detailed interaction, the production of secondary particles and their kinematics are controlled by a *model*. Since multiple models can be implemented and assigned to a process new models can be produced and used without affecting previous code. Physics lists are provided by the GEANT4 collaboration which are a compilation of sets of processes and models for particle types and energy ranges.

²Iterative, numerical methods for getting approximate solutions of ordinary differential equations.

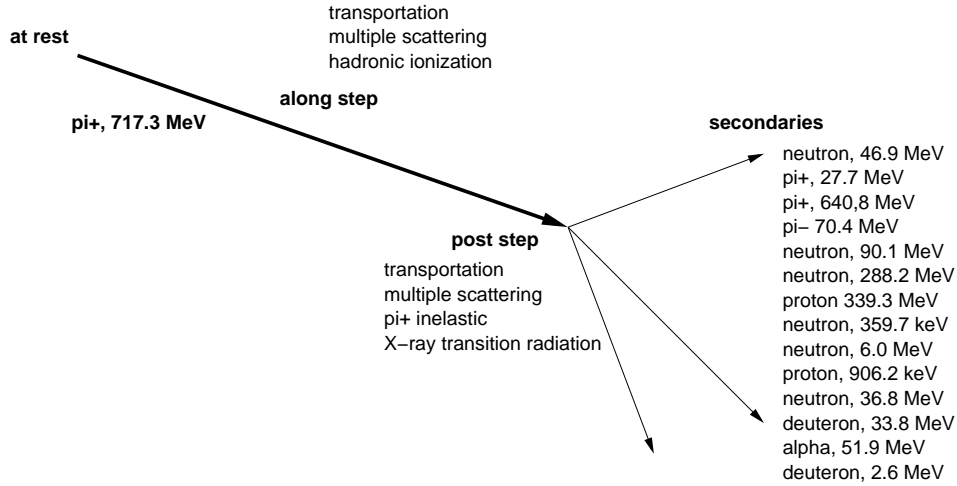


Figure 5.2: Schematic of one simulation step of a π^+ with 717.3 MeV in GEANT4. No processes are scheduled for *at rest*. Along the step (*along step*), three processes take place, transportation, multiple scattering and hadronic ionization. Transportation is necessary for every movement of a particle in GEANT4. The hadronic ionization produces an energy deposit along the path of the particle. Multiple scattering will change the path of the hadron slightly. At the *post-step* transportation, multiple scattering, X-ray transition radiation and the process which limited this step - an inelastic scattering of the π^+ are executed. At the post-step, 14 secondaries are produced whose type and energy are written.

The processes are classified into several sub-categories — hadronic, electromagnetic, transportation, decay, optical, the production of hadrons by photons and leptons, and parameterizations [13].

A process can implement three actions — *at rest*, *along step* and *post step*. In fig. 5.2 a schematic of one step finishing with inelastic scattering of a π^+ is shown.

5.3.1 Decay of particles and nuclei

Default decay tables based on data from the Particle Data Group [5] for many particles (e.g. π , K mesons, Σ , Λ) are provided in GEANT4. The user can also set a decay time and mode of primary particles by himself. GEANT4 selects the particular decay time or path according to the algorithm described in section 5.2.3. Complex decays (e.g. of B mesons) are not modeled. GEANT4 offers two ways of including them into the simulation. Firstly, an interface to external event generators is provided. A concrete implementation of this interface which communicates with an external program to choose a decay mode and secondary particle momenta can be attached to the decay object of the

particle. Secondly, a pre-assigned decay mode approach is possible. Here, the primary event generator simulates the decays of heavy particles beforehand. GEANT4 simply attaches these simulated daughter particles to the parent when that type of decay is requested [13].

5.3.2 Electromagnetic processes

The number of electromagnetic processes implemented in GEANT4 is very large. Interactions of electrons, positrons, photons and charged hadrons are treated. Standard electromagnetic processes average effects of the shell structure of atoms. This leads to a loss of precision where shell effects are important.

The processes implemented for photons are:

- Compton scattering
- γ -conversion into electron and muon pairs
- Photo-electric effect

The processes implemented for e^- and e^+ are:

- Bremsstrahlung
- Ionization
- δ -ray production
- e^+ annihilation
- synchrotron radiation

At the initialization of GEANT4 for every material present in the experimental setup, tables for the energy $\varepsilon(r)$ depending on the range r and tables for the absorption length vs. energy are produced by integrating numerically the *energy loss* of the particles.

For the calculation of the energy loss of e^- and e^+ the continuous contributions to the energy loss from ionization and bremsstrahlung and the discrete contributions from Moeller scattering, Bhabha scattering, δ -ray production and hard bremsstrahlung are summed up. The calculation of the energy loss of muons is done as for e^- and e^+ but with contributions from three processes—ionization, bremsstrahlung, pair production.

The processes include the simulation of δ -ray production, hard bremsstrahlung and hard direct e^+/e^- pair production. For charged hadrons only ionization (including the discrete process of hard δ -ray production) contributes to the energy loss.

With the known energy loss dE/dx of a given particle in a given material and the energy $\varepsilon(r)$ the energy loss during one step can be calculated. With s being the step length and r_0 the range at the beginning of the step eq. 5.6 describes the mean energy loss:

$$\Delta\varepsilon = \varepsilon(r_0) - \varepsilon(r_0 - s) \quad (5.6)$$

The approximation

$$\Delta\varepsilon \approx s \left| \frac{dE}{dx} \right| \quad (5.7)$$

can be used for $s < \kappa r_0$. κ denotes the *linear loss limit* which is an arbitrary parameter. Subsequently the *energy loss* is calculated by adding fluctuations to the *mean energy loss*.

Multiple scattering is simulated for all charged particles. The process calculates the angular deflection, the mean path length correction and the mean lateral displacement for one step due to multiple scattering.

To achieve a range of validity for electromagnetic processes which goes further down to 250eV a low energy extension for electromagnetic processes has been put in place. Electrons, photons, positive and negative charged hadrons and positive ions are covered by processes. Positron and negative ion interactions are in development.

Examples of additions to the standard processes treating the low energy of electromagnetic processes in more detail are mentioned in the following list:

photoelectric effect: electron emission of a metallic surface due absorption of photons with a wavelength below a material dependent threshold

Compton scattering: decrease of the energy of an X-ray or a gamma-ray photon due to interaction with matter

Rayleigh scattering: scattering of electromagnetic radiation on particles smaller than its wavelength

fluorescence emission from excited atoms: excitation of an atom due to absorption of a photon of a particular wavelength leads to an emission of light with a longer wavelength.

Auger effect: radiation-less deexcitation of an atom by emission of an electron.

corrections due to the molecular structure of materials

corrections due to the effect of the nuclear stopping power

Barkas effect: Describes the difference in stopping power of particles depending on their charge. For positively or negatively charged mesons of the same initial energy the Barkas effect results in a difference of their range.

The ionization by hadrons and ions is modeled differently depending on the energy range. The model for high energies (> 2 MeV) uses the Bethe-Bloch formula while in the low energy region (< 1 keV for protons) a free electron gas model is taken. The intermediate range is covered by parameterizations based on experimental data [13].

Electromagnetic processes producing hadrons

In GEANT4 photonuclear and electronuclear reactions are implemented which can convert electromagnetic energy flow (electrons, positrons, photons) into energy flow of mesons, baryons and nuclear fragments. At high energies in the nuclear giant resonance region (above 10 MeV) the cross-sections of these effects are of the same order of magnitude as other electromagnetic processes. Hadron production by nuclear interaction of muons is taken into account as well.

5.3.3 Hadronic processes

The hadronic processes in GEANT4 cover the energy range from thermal neutrons (about 0.025 eV) to interactions at 7 TeV and more for experiments at LHC and for cosmic ray physics. Models can be varied and thus adjusted to the particular setup of the experiment. For calorimetry a good description of hadron nuclear interactions and leading particle effects are crucial. The total cross-sections of GEANT4 for inelastic scattering, capture of neutral particles, induced fission and elastic scattering are parametrized in function of A (atomic weight) and E (particle energy). For hadron induced interactions below 20 GeV and for ion spallation reactions specialized data-sets are provided which replace the GEANT3 cross-sections.

Structure of implementation

Hadronic processes in GEANT4 are organized in several levels. The uppermost one implements the most general use-case for shower simulation and provides the standard

interface for a hadronic process. Each subsequent level treats more specific details of the implementations. Level 2 implements cross-sections and models. There are sources of cross-sections and a number of final state production models which can be chosen by the user. Level 3 provides the user with a framework to insert theory driven models. Level 4 interfaces commonalities for string-parton models and intra-nuclear cascade models. Level 5 treats string de-excitation and is designed to study various fragmentation functions with different types of string fragmentation [21].

Cross-sections

A data-driven approach is used to determine the inclusive scattering cross-sections for hadron-nuclear scattering. This can be complemented with theory-based approaches to extend the model to predict these cross-sections at high energies or to extract missing ones from the measured ones.

Modeling of final states

There are three possibilities for the modeling of final states:

- evaluated or measured data
- parameterizations and extrapolations of experimental data
- theory-driven models.

An approach based on evaluated or measured *data* is obviously to be preferred. Limitations are determined by the availability of precise data. Sufficient data might not be available, for example, for projectiles with high energies, particles with short life-times, strange baryons and for various target materials. The data driven approach is mainly used for:

- isotope production induced by neutrons and protons
- detailed transport of neutrons at low energies (available data: < 20 MeV for neutron kinetic energies, < 150 MeV for some isotopes)
- photon evaporation at moderate and low excitation energies
- radioactive decay (including isomeric transitions, internal conversions and atomic de-excitation after decay or evaporation)
- absorption of particles coming to rest (mainly for μ^- , π^- , K^- and \bar{p})

Parameterized models in GEANT4 are mostly re-written versions of models existing in GEANT3 (GHEISHA [22]). These parameterizations of momentum and angular distribution of the particles produced in reactions and extrapolations of cross-sections and interactions are used for a large quantity of reactions over the full range of energies for hadronic showers. They provide the possibility to tune the simulated hadronic showers to data obtained in testbeams. Examples for physical processes which are modeled that way are:

- induced fission (for neutrons)
- capture (for neutrons)
- elastic scattering
- inelastic final state production

A number of theory-based models are implemented into GEANT4. Some of those being the current state of art. A theory-based approach allows for a better extrapolation of results to energies which were not assessed in testbeams. For interactions of hadrons with a nucleus producing high energy final states ($E_{\text{CMS}} > O(5 \text{ GeV})$) the following parton string models are available:

diffractive string excitation model (Fritiof like): The particles which are scattered only exchange momenta. For each of the scattered particles a string is formed where the quark content of the original hadron is randomly assigned to the string ends [23]

quark gluon string model: The quark gluon string model splits a nucleon into a quark and a di-quark. Between those, strings are formed and hadronized (by adding a $q\bar{q}$ -pair). The color flow between partons from the interacting particles and the hadron-nucleon interactions are mediated by the exchange of Pomerons [23].

Well established fragmentation functions are used for the modeling of the string decay.

For $E_{\text{CMS}} < 5 \text{ GeV}$, intra-nuclear cascade models (e.g. Binary cascade [24], Bertini cascade [25]) can be used. Those models are based on average description of the nuclear medium where effects like coherence length, Pauli-blocking, and formation times are taken into account. The Bertini nucleon-nucleon cascade assumes a step-like concentric nuclear potential in three dimensions. The projectile is transported along straight lines

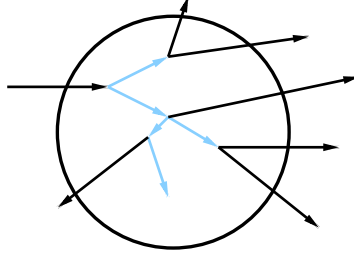


Figure 5.3: Schematic of the Bertini intra-nuclear cascade model. Projectiles are transported along straight lines within the nucleus. Interaction probabilities are computed according to the mean free path. Cross-sections are taken from experimental data.

within the nucleus and the probabilities of interactions are computed according to the mean free path. Cross-sections are taken from experimental data (fig. 5.3).

For energies below $E_{\text{CMS}} < O(100 \text{ MeV})$ two exciton based pre-compound models are available³. They describe energy and angular distributions of the fast particles and are capable to soften the otherwise too steep behaviour of the quasi-elastic peaks.

For the last phase of a nuclear interaction – the evaporation phase – the following models can be used, which describe the behaviour of excited, thermalized nuclei:

- variants of the Weisskopf-Ewing model
- Fermi breakup model (for light nuclei)
- multifragmentation (for very high excitation energies)
- fission

Finally the electron configuration in the residual atom is estimated and atomic relaxation is performed [14].

An alternative to the nuclear fragmentation models is the *chiral invariant phase space* (CHIPS) model. It is a quark level $SU(3) \times SU(3)$ symmetric event generator which treats the fragmentation of excited hadronic systems into hadrons using a universal thermodynamic approach. It can be applied to many hadron-nuclear and lepto-nuclear interactions. [13, 14]

³An exciton is a quasiparticle consisting of a nucleon and a nucleon-hole (analogous to an electron and an electron-hole in a non-metallic crystal where it can move freely). After recombination of nucleon and nucleon-hole, the exciton vanishes.

5.4 Optical processes

In GEANT4 photons with wavelengths much greater than the typical atomic spacing are called *optical*. The corresponding processes are derived from the wave like property of electromagnetic radiation. The optical properties of a medium can be given by the user as a function of the photon's wavelength. Processes which are implemented specially for those optical photons are [13,14]:

Čerenkov process: When a charged particle passes through a medium (insulator) faster than the speed of light in that particular medium the so called Čerenkov radiation is emitted. The Čerenkov radiation can be described with well known formulae.

Scintillation: The emission of light of scintillation material due to ionization. The user can define the material's characteristic light yield, photon emission spectrum and other empirical parameters.

Absorption and Rayleigh scattering: For a correct treatment of absorption, the user has to provide GEANT4 with the empirical data for the absorption length. This process kills the particle. Scattering of electromagnetic radiation with a wavelength much larger than the size of the particles by which it is scattered is called Rayleigh scattering.

Reflection and Refraction: GEANT4 provides the possibility to define optical boundaries where reflection and refraction are simulated.

Transition Radiation: Transition radiation is emitted by a charged relativistic particle which crosses the interface between two materials of different dielectric properties.

5.5 Physics lists

Although any combination of processes and models for all types of particles can be compiled in principle, the GEANT4 collaboration provides several physics lists which combine present best knowledge. While the electromagnetic interactions are well known and the simulations are of very good accuracy, the modeling of the physics of hadrons has not yet the same level of reliability. Therefore various possibilities are available as option to the user. In this section an overview about the currently available models is given.

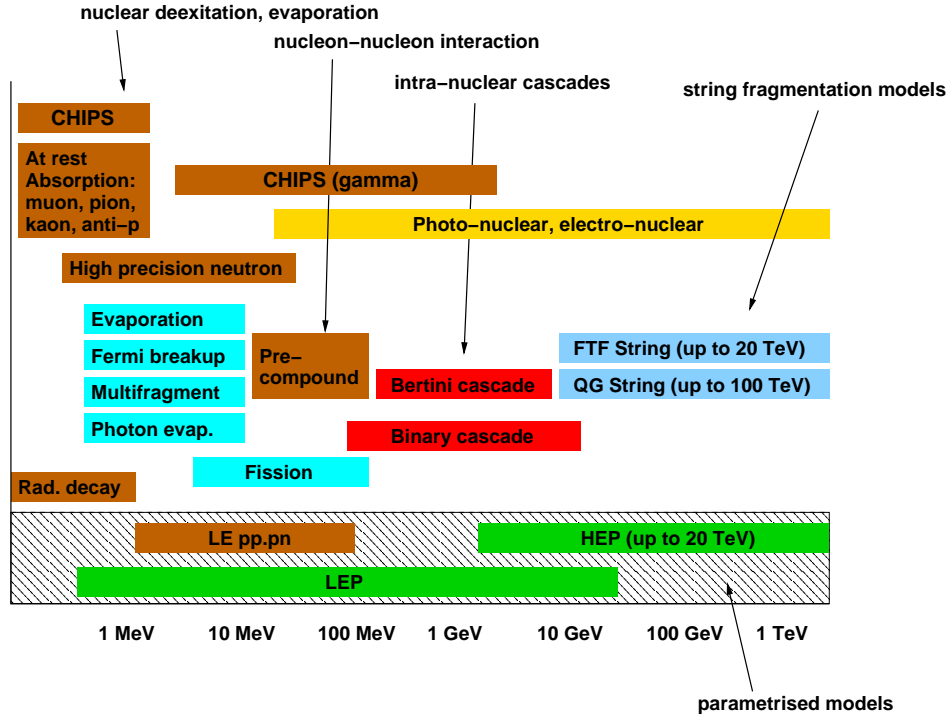


Figure 5.4: Selection of available models which can be combined to physics lists in GEANT4.

5.5.1 Models and energy regions

Fig. 5.4 provides an overview of models which are available and the approximate energy ranges of their respective validity. In a physics list for each particle type the processes and models and the energy range of their validity can be defined. The oldest models are the parametrized models which are shown on the bottom of fig. 5.4. They have been transferred from GEANT3 (GEISHA) to GEANT4. The *low energy parametrized model* (LEP) and the *high energy parametrized model* (HEP) are used as a fall-back solution for all physics lists for particles and energy regions where no other models are defined. Besides HEP, for high energies there are two theory-based models available, the *quark gluon string* (QGS) model and the *Fritiof* (FTF) model which are theory-based models for the simulation of the scattering of high energetic hadrons with nuclei.

The high energy model QGS is valid down to about 12 to 25 GeV, FTF even down to 5 to 10 GeV. Below that, the LEP model or a model for intra-nuclear cascades (Bertini cascade, binary cascade) can be used (fig. 5.3). A multitude of models are available for the simulation of nuclear deexcitation, evaporation etc. for energies down to the keV-level.

The transition between different models in different energy regions (e.g. from QGS to Bertini cascade) are smoothed out such that a continuous transition between the models is achieved. For each interaction which has an energy in the region between the two adjacent models, one of the two models is chosen randomly with an energy dependent probability.

5.5.2 Implemented physics lists

Due to the complex behaviour of hadronic showers the ability to predict the data is still inferior to the simulation of electromagnetic showers. The GEANT4-collaboration puts a large effort into improving the modeling of hadronic showers by comparing simulations to data for many experimental setups and providing improved models for certain physical effects. The requirements for the accuracy of the description of the data by simulations in ATLAS is very high which makes it important to determine the best performing combination of physical models (physics lists).

Questions which have to be answered are: Which fragmentation model describes best the shower development (QGS, FTF)? Do intranuclear cascade models improve the shower description? If yes, which one (Bertini cascade or Binary cascade) agrees better with data and what is the range of applicability? Is a high-precision simulation of the low energy neutrons necessary (increases significantly the computing time)? Does a diffraction model for pions and protons improve the agreement between simulations and data? Does the precompound or the CHIPS model lead to a better description of data? Does the model simulating quasi-elastic scattering improve the agreement of the simulations with data?

For that purpose, fifteen physics lists with different combinations of the mentioned models have been provided by the GEANT4-collaboration to be able to disentangle the effects of the different models. The comparison of the physics lists with data is presented in sec. 9.

In the following description of the implemented physics lists which have been evaluated in this thesis and their energy ranges are mentioned. All physics lists are taken from GEANT4.91 except the one marked as GEANT4.7.

QGSP Quark (Q) gluon (G) string (S) precompound (P) model. QGS for the high energy range down to 12 to 25 GeV, below that LEP.

QGSC Quark gluon string chiral invariant phase space (CHIPS) model. QGSC down to 25 GeV, below that LEP.

FTFP Fritiof precompound model. FTFP down to 10 GeV, below that: LEP

FTFC Fritiof CHIPS model. FTFC down to 10 GeV, below that: LEP

QGSP_BERT Quark gluon string precompound model with Bertini cascade. QGS above 25 GeV. Between 25 GeV and 10 GeV: LEP. Below that: Bertini cascade.

QGSP_BERT_NQE Quark gluon string precompound model with Bertini Cascade, without quasi-elastic scattering. QGSP for energies above 25 GeV. Between 25 GeV and 10 GeV: LEP. Below 10 GeV: Bertini cascade.

QGSP_BERT_HP Quark gluon string precompound model. QGS above 25 GeV. Between 25 GeV and 10 GeV: LEP. Below that: Bertini cascade. For low energy neutrons a *high precision* (HP) simulation is used which needs considerably more computing time.

QGSP_BERT_TRV Quark gluon string precompound model, transition variant. QGS above 25 GeV. Between 25 GeV and 4 GeV: LEP. Below that: Bertini cascade.

QGSP_BERT_DIF Quark gluon string precompound model. QGS above 25 GeV. Between 25 GeV and 10 GeV: LEP. Below that: Bertini cascade. A diffraction model for pions and protons is added.

QGSP_BIC Quark gluon string precompound model. QGS above 25 GeV. Between 25 GeV and 10 GeV: LEP. Below that: Binary cascade for protons.

QGSP_BIC_HP Quark gluon string precompound model. QGS above 25 GeV. Between 25 GeV and 10 GeV: LEP. Below that: Binary cascade for protons. For low energy neutrons a *high precision* (HP) simulation is used which needs considerably more computing time.

QGS_BIC Quark gluon string model. QGS above 25 GeV. Between 25 GeV and 10 GeV: LEP. Below that: Binary cascade for protons and pions.

FTFP_BERT Fritiof model with Bertini cascade. FTF above 10 GeV. Below that: Bertini cascade.

FTF_BIC Fritiof precompound model with binary cascade. FTFP above 5 GeV. Below that: Binary cascade. In this model no parametrized model (HEP, LEP) is used for pions and protons.

QGSP_BERT (GEANT4.7) Quark gluon string precompound model with Bertini cascade and without quasi-elastic scattering.

5.6 CalibrationHits and calculation of the invisible energy

When particle showers are simulated with GEANT4 the deposited energies are completely known at every time. For the simulation of the detector signal only energy which is deposited visibly in the active parts of the calorimeter cells is taken into account. These energy deposits, but also those deposited in non-active material are stored in the so called *CalibrationHits*. The so recorded true deposited energy can then be exploited for the calibration of the detectors. We distinguish between energy which is deposited such that it will produce a signal in the calorimeter cells which can be measured (*visible energy*) and energy which cannot be measured (*invisible energy*) (see sec. 4.4.2).

The simulation of the trajectories and the interactions of the particles is done in small, discrete steps. The amount of visibly deposited energy is calculated in GEANT4 for each step as described in sec. 5.3.2 ($E_{\text{vis}} = \Delta\varepsilon$). With ΔE being the total energy loss of the particle during the step and $E_{\text{sec}} = \sum_i^{N_{\text{sec}}} E_{\text{sec},i}$ the energy which is used for the creation of N_{sec} secondaries with the respective energies $E_{\text{sec},i}$, the amount of energy deposited invisibly can be calculated with:

$$E_{\text{inv}} = \Delta E - E_{\text{vis}} - E_{\text{sec}} \quad (5.8)$$

The amount of invisible energy may differ considerably from event to event. There may be events where an incoming pion interacts $\pi^+ n \rightarrow \pi^0 p$ and the resulting π^0 decays immediately $\pi^0 \rightarrow \gamma\gamma$. This leads to a shower which is nearly completely electromagnetic and thus deposits only a small fraction of invisible energy. On the other hand at reactions where nuclei are broken up or excited, a large fraction of energy can be deposited invisibly. Due to this variation of the invisible energy in the events, the resolution achieved for hadronic showers is worse compared to the one for electromagnetic showers.

5.7 Summary

The GEANT4 simulation framework provides a large number of implementations (models) for physical effects treating the interaction of all kinds of elementary particles (e.g. hadrons, leptons). In the simulation, for the whole energy range of each particle type

multiple physical models and their cross-sections can be defined to build up a consistent set of physical interactions called “physics lists”. In the simulation all visible and invisible energy depositions are known and stored in the so-called CalibrationHits. They can be used to derive the corrections for the energy measurement of hadronic showers in the ATLAS calorimeter system.

6 Computing Model

A large number of simulated events is necessary for the evaluation of the accuracy of the simulation and the derivation of the corrections for the energy measurement. To be able to produce the simulations the GRID network has been extensively used. In this chapter the LHC computing Grid is presented and the way the CTB simulations are performed is discussed.

6.1 The LHC Computing Grid

LHC Computing Grid (LCG) aims at building and maintaining a computing infrastructure for large scale, resource intensive tasks. It is capable of providing an analysis infrastructure and a data storage for the high-energy physics experiments using the LHC. Instead of a large centralized computing facility it has been opted for distributing the computing tasks to a multitude of computing centers all over the world. The data coming from the LHC experiments is hierarchically distributed around the globe and processed around-the-clock.

Each year, about 15 Petabytes of data will be produced. Several thousand scientists from about 500 universities and research institutes around the world will analyze the data. The data has to be accessible over the 15 years lifetime of the LHC. An equivalent of about 100000 CPUs (taking the CPU-power of a 2004 built processor as measure) are needed for the analysis of the data and its comparison to MC simulations. An adequate bandwidth between the computing facilities is required.

The hierarchy of the LCG consists of 4 levels named Tier-0 to Tier-3.

Tier-0 The Tier-0 site of the LCG is located at CERN. Its task is the recording of the raw data coming from the data-acquisition systems of the experiments. Data is recorded on tape and distributed to Tier-1 sites. The first reconstruction of data is also done at the Tier-0 site.

Tier-1 The Tier-1 sites are large computing centers which provide an around-the-clock

operation and a storage capacity for a large fractions of the data. They provide computing power for extensive analysis tasks where large subsets of raw, processed or simulated data have to be accessed. They also distribute raw data to Tier-2 sites.

Tier-2 Each Tier-2 site consists of one or more (collaborating) computing facilities which get their data from the Tier-1 sites. The purpose of the Tier-2 sites is to provide computing power for analysis tasks and MC simulations of end-users. The individual scientists have access to Tier-2 sites through Tier-3.

Tier-3 Tier-3 are local clusters in research facilities or universities or are even individual PCs.

ATLAS will write out data events with a frequency of about 200 Hz. Each event will have a size of about 1.5 to 3 MB. The ATLAS experiment aims at processing 50% of the data within 8 hours and 90% within 24 hours.

6.2 Simulations of the CTB on the GRID

The GRID has been extensively used for the simulation of events for the CTB. Pions, protons and electrons have been simulated for energies up to 250 GeV with different physics lists. Improvements in the simulation such as the introduction of Birk's law made dedicated simulations necessary. In total 19 million events have been produced. Simulating these events on a single PC would have taken about 15 years.

Since the GRID is still under development and therefore mainly used by the GRID developers themselves and by dedicated teams producing large productions for the so called data challenges, the efficiency is not always good and the user interface is difficult to handle. A careful selection of GRID sites had been necessary, since the information from the GRID resource broker about the installed versions of the ATLAS software of a particular site sometimes didn't agree with the versions which were installed. Other sites showed notorious problems in handling our simulations and therefore jobs often crashed. Due to the number of simulations the error handling had to be automated. Depending on the type of error encountered a part of the jobs simply had to be restarted, for others though the site where the job failed had to be excluded from the list of permitted sites. Another source of problems has been the storage of the data. A GRID storage element

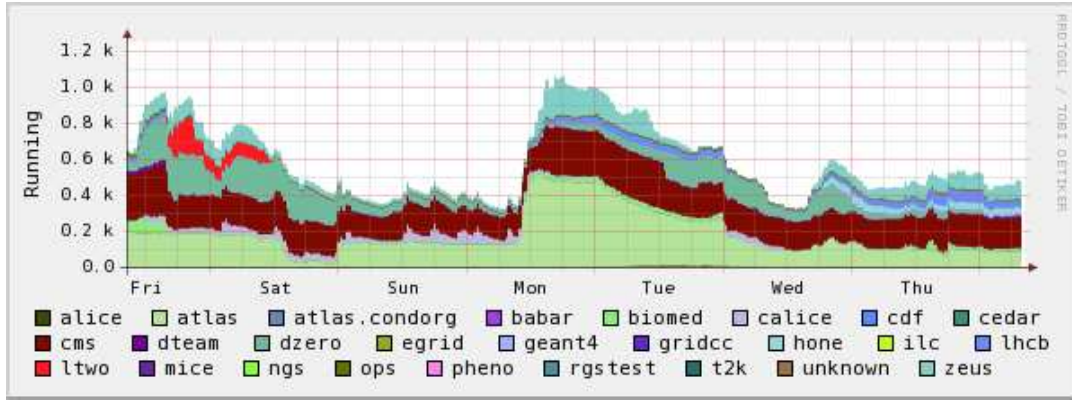


Figure 6.1: Number of operating processes vs. time is shown for the GRID site `ce02.esc.qmul.ac.uk`. A bunch of simulations for the CTB have been submitted at Monday. A peak for ATLAS can be seen at that day.

which is as well a CASTOR-site¹ has been chosen to host the simulated results since then the stored files are immediately accessible even for non-GRID-users. Frequently problems occurred at this process which again made a restart of the respective jobs necessary. Hence, a large amount of time had to be spent to develop the necessary programs and macros to reliably run the simulations. With the gained experiences, other users have been trained to use the GRID.

Fig. 6.1 shows as example a figure which is produced routinely to monitor a certain site at the Grid showing the numbers of operating processes versus time for one of the GRID sites which received a large number of simulations. About 400 runs submitted to simulate the CTB were simulated at that site from Monday (peak for ATLAS) to approximately Wednesday. The same number of simulations would take several weeks for a single normal user at the CERN batch queue (since many people at CERN compete for the available CPU time) and would be impossible on a local machine.

¹CASTOR is the acronym for CERN Advanced STORage manager. It is a storage management system which provides disk- and tape-storage for the LHC experiments and for user files.

7 Combined Testbeam 2004 (CTB)

The corrections for the energy measurement in ATLAS are derived from MC simulations. This relies on a good description of the data by the simulation. Several influences, like an inexact description of the detector geometry or an insufficiently accurate modeling of physical effects in the MC simulation might impair the agreement of MC and data. It is therefore necessary to evaluate the agreement of the simulations with data. A MC to data comparison makes it possible to evaluate each step of the reconstruction of the energy from the cell-level up to the event-level. Before the first pp -collisions in ATLAS, the only source for data are the testbeams which have been undertaken for the calorimeter subsystems and more recently for a full slice of the central part of the ATLAS detector (Combined Testbeam 2004). The comparisons of data and MC simulations in this thesis have been done on the basis of the Combined Testbeam 2004.

7.1 The setup of the H8 beam line

The H8 beam line of the CERN's Super Proton Synchrotron (SPS) provided a beam of electrons, pions or muons to the ATLAS Combined Testbeam 2004. For the primary beam, this beam line emits typically 10^{12} protons per burst with a momentum up to 450 GeV/c. By shooting this beam on a 30 mm Beryllium plate a shower of secondary particles with different types and a wide range of momenta is produced. Using a vertical magnetic spectrometer particles with a certain momentum can be selected. For positive polarity the momentum of the secondary beam can be selected between 10 GeV/c and 180 GeV/c, for negative polarity up to 400 GeV/c. A secondary filter target can be chosen to increase or decrease the electron/pion fraction in the beam. By directing the beam onto a combination of targets further downstream (tertiary beam) and a dedicated magnetic spectrometer very low energy beams can be produced [26].

7.1.1 Calculation of the beam energy

Several quadrupole and dipole magnets have been placed in the beam line for focusing and bending particles. The desired beam momentum could be chosen by selecting the

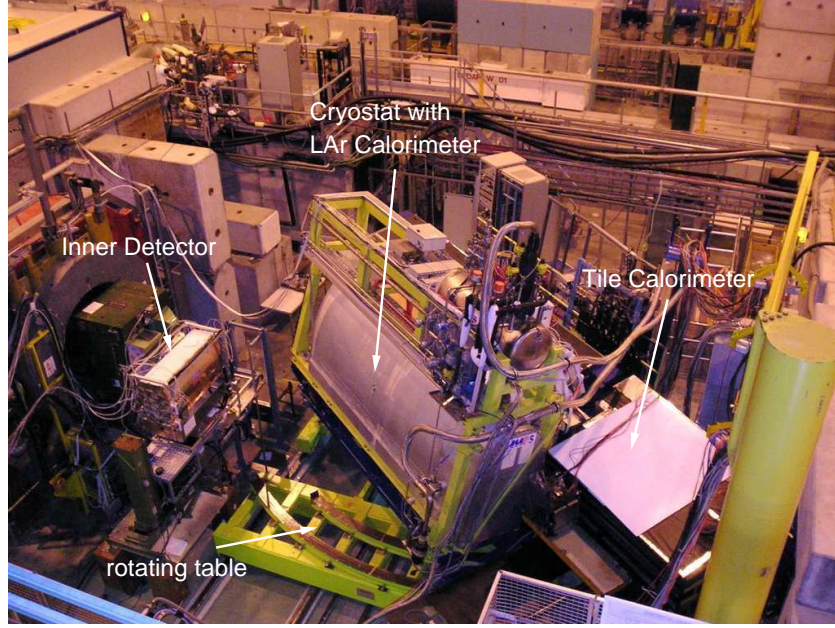


Figure 7.1: Photo of the testbeam setup.

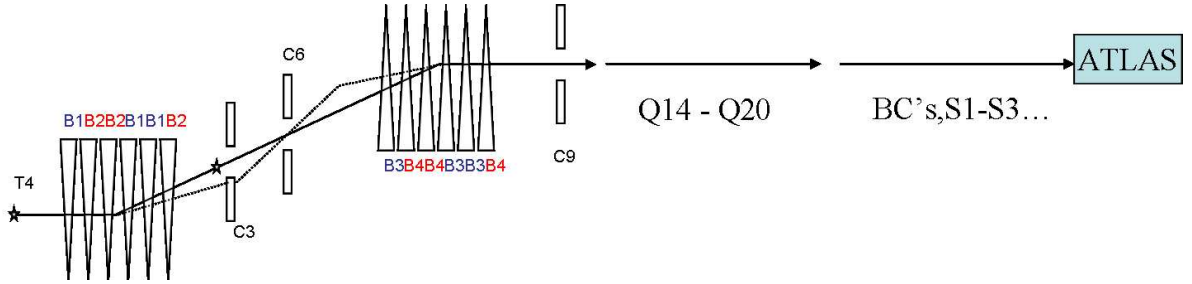


Figure 7.2: Schematic of the beam line far upstream (in the vertical plane).

adequate magnet currents. For an accurate analysis of the taken data, it is necessary to know the precise energy of the particle impinging on the calorimeter. The momentum can be determined knowing the bending power $\int B dl$ of the vertical bending magnets (V-BEND) B3 and B4. Those together with the collimators C3 and C6 form a magnetic spectrometer.

In the magnetic field of the bending magnets, the trajectory of a charged particle can be described by an arc with the radius r given by

$$\frac{1}{r} = e \frac{B}{p} \quad (7.1)$$

where e is the electric charge, B the magnetic field and p the momentum of the particle.

magnet/case	a_0	a_1	a_2	a_3
B3/ $I \leq I_0$	7.93470×10^{-3}	2.18130×10^{-2}		
B3/ $I > I_0$	4.37329×10^{-1}	2.12849×10^{-2}	3.55516×10^{-6}	-1.47542×10^{-8}
B4/ $I \leq I_0$	7.86406×10^{-3}	2.18140×10^{-2}		
B4/ $I > I_0$	4.34258×10^{-1}	2.12899×10^{-2}	3.56113×10^{-6}	-1.47379×10^{-8}

Table 7.1: Coefficients for the calculation of the magnetic bending of the magnets B3 and B4.

The angle by which the beam is bent in the magnetic field can be calculated with

$$\Delta\Theta = \int \frac{dl}{r} = e \frac{\int B dl}{p}, \quad (7.2)$$

where the integral is calculated along the trajectory of the particle within the magnet. Written in terms of typically used units in high energy physics we obtain for the particle momentum

$$p \left[\frac{\text{GeV}}{c} \right] = e \frac{\int B dl}{10^9 e \Delta\Theta / c} = 0.2998 \frac{\int B [\text{T}] dl [\text{m}]}{\Delta\Theta [\text{rad}]} \quad (7.3)$$

where $\Delta\Theta = 41$ mrad for the H8 beam line. The total bending power is the sum of the bending powers of the magnets B3 and B4 $\int B dl = \int_{\text{B3}} B dl + \int_{\text{B4}} B dl$ which themselves can be written as a function of their electric current.

$$\int_{\text{magnet}} B dl = \begin{cases} a_0 + a_1 I, & I \leq I_0 \\ a_0 + a_1 I + a_2 (I - I_0)^2 + a_3 (I - I_0)^3, & I > I_0 \end{cases} \quad (7.4)$$

I_0 is 824.12 A for both magnets B3 and B4. The values for the coefficients are compiled in table 7.1.

For the very low energy (VLE) beam line, a tertiary target had to be put into the beam line. This is due to the long distance from the T4 target to the detectors. The decay length of pions with low momenta is much shorter than the distance from target T4 to the detectors. The decay length of a pion with 1 GeV/c is 56 m. After this distance only about 30% of particles remain without having decayed. For the whole beam line (500 m) nearly no pions would remain in the beam. Putting a tertiary target closer to the detector gives the possibility to produce low energy pion beams. Further magnets had to be installed, as those of the high energy beam line would reach at such low magnetic fields the limits of their power supplies in terms of stability and precision. New magnets

b_0	b_1	b_2	b_3	b_4
5.30982×10^{-3}	3.28502×10^{-6}	5.32397×10^{-9}	2.76483×10^{-12}	3.368×10^{-15}

Table 7.2: Coefficients for the calculation of the magnetic bending of the magnet B8.

had to be installed for the momentum selection such that they could use relatively high currents for the whole range of provided beam energies (1 GeV/c - 10 GeV/c) [27].

The low energy beam line is fed with a beam of the energy 40-50 GeV/c. The momentum selection of the VLE beam depends on the field of magnet B8. The exact calculation is done according to the procedure for the high energy beam line. With an angle $\Delta\Theta$ of 120 mrad the formula 7.3 gives

$$p \left[\frac{\text{GeV}}{c} \right] = 2.49826 \int_{B8} B dl \quad (7.5)$$

and $\int_{B8} B dl$ can be calculated with

$$\int_{B8} B dl = b_0 I + b_1 I^2 + b_2 I^3 + b_3 I^4 + b_4 I^5 \quad (7.6)$$

and the coefficients given in table 7.2.

For the high energy beam line, the influence of the collimators C3 and C9 on the beam spread has been assessed by simulating the beam line varying their openings over their range from ± 2 mm to ± 60 mm each.

7.1.2 Description of the beam instrumentation

For the purpose of offline data control and event triggering several instruments have been placed upstream of the inner detector and the calorimeter. Their data has been added to the event data of the ATLAS detectors and some of the scintillators were used to trigger the readout. In figure 7.3 a schematic of the layout is shown. The exact setup could be varied to meet the specific requirements for different studies.

Čerenkov counters

Three Čerenkov counters have been positioned in the beam line. One of them in the high energy beam line (CHRV2,HE), one in the low energy beam line (CHRV2,VLE),

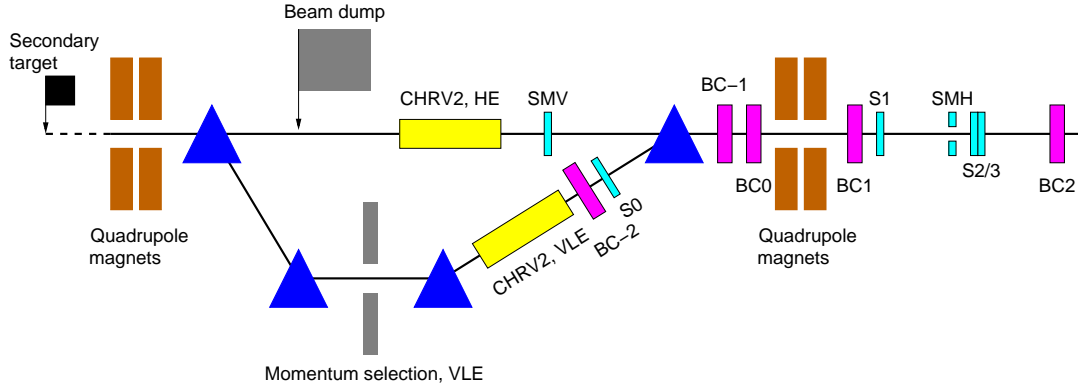


Figure 7.3: Layout of the beam line.

and a third one further upstream (CHRV1) which is not visible in the scheme 7.3. Their purpose has been to be able to separate pions and electrons at low energies. For the analysis only CHRV2,VLE could be used, the other Čerenkov counters were not operational at data taking.

Beam chambers

Five beam chambers (denominated BC-2 to BC2) of the type of delay wire chambers (DWC) have been placed into the beam line. Their purpose has been the measurement of the exact position of the particle. The working principle of those chambers is that of multi wire proportional chambers. A particle passing through the chamber will ionize the gas. Thus, free electrons are created which are accelerated towards the anode. The strong field near the anode wires provokes an avalanche multiplication. In the cathode wires placed closest to the avalanche an image current is induced. The cathode wires are connected by a tapped delay line. Their signal is summed up according to the delay per tap. By measuring the time delay for the integrated waves at each end of the delay line compared to the anode signal, the impact point of the particle can be determined. A two dimensional readout of the position of the particle impact can be obtained by placing a second plane of anode and cathode wires orthogonally into the same casing [28]. The space resolution of the beam chambers used in the CTB was about $200 \mu\text{m}$.

Scintillators

For the purpose of particle selection and triggering some scintillators have been placed in the beam line. In the following the scintillators are described in the order from upstream to downstream:

Muon veto (SMV) was located at the end of the high energy beam line before the dipole magnet. The muon veto is used to tag unwanted muons passing through the high energy beam line while using the low energy beam line.

S0 was positioned in the VLE line. It is used for checking the beam intensity.

S1 is located after the quadrupole magnets and beam chamber BC1. It is used in combination with S2 and S3 as the main trigger.

Muon halo (SMH) is located after S1. It is a scintillator with a hole of 3.4 cm diameter centered on the beam. Its purpose is the tagging of halo muons and other particles.

S2, S3 are used in combination with S1 for the main trigger. Their position is closely after the muon halo scintillator.

Cryostat scintillator is located between the LAr- and the Tile-Calorimeter. It can be used to estimate the energy deposited in the dead material between the two calorimeters.

Muon Wall is a combination of 12 scintillators placed behind TileCal. Its purpose is to recognize particles leaking out behind the calorimeters. of leakage.

Muon Tag is placed downstream after the first beam dump. The muon tag recognizes the muons as they are the only particles which can penetrate the beam dump.

Triggering

The trigger signal was designed to emulate the level 1 accept (L1A) as it is used in ATLAS to trigger the readout of one event. It was composed most of the time by the signal of the scintillators S1, S2 and S3 being in coincidence, vetoed by the Muon veto and the Muon Halo scintillator.

Measurement of the particle phase

Whenever the readout was ready to take data a L1A initiated - based on a 40.08 MHz clock (emulating the LHC bunch crossing clock) - the readout of all detectors. With a TDC which was started by the trigger and stopped by the clock the phase between the arrival of the particle and the readout clock could be measured. The knowledge of this phase is necessary for the precise reconstruction of the energy in the LAr calorimeter.

7.2 Data set and event selection

Even for a nominal pion beam, in general the beam is contaminated by other particles like electrons, muons or protons. The particle type has to be determined by the beam line detectors, if possible. The composition varies a lot depending on the beam energy.

Several cuts have been applied to get a clean sample of pions (contaminated with protons):

- Only physics events with a valid trigger signal were accepted. Events without a particle in the detector, resulting only noise are not taken into account.
- Only events of which the particle position has been measured in the beam chambers were accepted, i.e. events with erroneous measurements have been removed.
- A narrow beam spot in BC0 was required. Only events were considered where $-20 \text{ mm} < \text{BC0}_x < 20 \text{ mm}$ and $-20 \text{ mm} < \text{BC0}_y < 20 \text{ mm}$.
- A narrow beam spot in BC1 was required. Only events were considered where $-20 \text{ mm} < \text{BC1}_x < 20 \text{ mm}$ and $-20 \text{ mm} < \text{BC1}_y < 20 \text{ mm}$.
- A parallel beam was required, i.e. only events where the coordinates in subsequent beam chambers (e.g. BC-1/BC0) differ less than 10 mm in x and 20 mm in y (BC-1 is shifted by about 40 mm compared to BC0 which were taken into account).
- At least one track in the Inner Detector with a relevant number of hits was required (sum of the hits in the Pixel detector and the SCT has to be greater than 6). This makes sure the particles pass through these sub-detectors and do not hit support material in the beam line.
- One track in the TRT with at least 20 hits was required. Reject events with a second track with more than 9 hits. This makes sure the pion passes as mip and does not make a hadronic interaction before the calorimeter.
- Two or less higher level hits in the TRT were required. This selects pions and rejects electrons.
- Muons passing through the scintillator behind the calorimeters were excluded by requiring $360 < \text{MuonTag} < 400$
- By removing all events where more than 99% of the energy has been deposited in the LAr calorimeter electrons were excluded. This is necessary to reject the residual electron contamination. A very small fraction of pions that interact electromagnetically are also rejected this way.

p_{beam}	proton fraction	events	selected events
[GeV/c]			
20	0	51300	10155
50	0.41	118672	27799
100	0.59	72553	14549
180	0.75	200390	18739

Table 7.3: Proton fraction in a nominal pion beam depending on the beam energy as determined with the TRT. The third column shows the total number of events for each beam energy and the fourth column the selected events.

The data set (runs) used in this analysis and the total number of events and the number of selected events are listed in table 7.3.

Due to a wrong gas pressure-setting of the Čerenkov counter in the high energy runs it could not be used to separate pions from protons. Therefore it was not possible to identify protons on an event-by-event basis. In the very low energy region ($E_{\text{beam}} < 10\text{GeV}$) the Čerenkov V2 counter was used for electron/pion separation.

In table 7.3 the proton contamination for nominal π^+ beams of the analysis used in the fully combined data taking period 8 of the CTB are given for several energies. These proton contaminations have been measured with the TRT. The inner detector can determine an average of the fraction of protons in the beam by analyzing the probability that a particle passing through the gas produces a high level hit (a hit with large ionization) as a function of the velocity factor of the particle. These proton fractions are in rough agreement with the measurement performed in the 2002 testbeam with a Čerenkov counter. At 20 GeV the estimated fraction is compatible with zero. In 2002 no proton contamination has been found. The uncertainty on the proton fraction is about $\sim 20\%$.

Since pions and protons cannot be separated on an event-by-event basis, for comparisons of data with simulations, it is therefore necessary to simulate both, pions and protons and mix them according to their respective fractions for the analyzed beam energy.

7.3 Simulation of the detector response in Monte Carlo

With the Monte Carlo simulation, the energy deposits at every position inside and outside the detectors can be calculated. However, to derive for the simulation the signal created by the calorimeter cells equivalent to data the energy depositions have to be

combined according to the readout structure of the calorimeters. This process is called *digitization*. In addition, the noise in the detector has to be simulated and other physical processes in the detector that alter the detector response and that are not included in the GEANT4 framework have to be taken into account. Such effects are described in this chapter.

7.3.1 Modeling of noise

For the cells in the Tile and the LAr calorimeters the noise distribution has a Gaussian shape. The noise distribution of the different types of cells has been measured at the CTB with randomly triggered events. The energy from the simulation is convoluted with a Gaussian noise distribution with the standard deviation taken from data. The good accuracy of the simulation of the noise distribution has been shown by comparing data and MC. It has also been checked that the noise is stable over the data taking period.

7.3.2 Photo statistics

In the Tile calorimeter cells the signal is created by scintillation. The created photons are collected with optical fibers and transmitted to photomultipliers (PMT). The number of photons reaching the PMTs and consequently the number of photoelectrons created by the PMTs are Poisson distributed. The light yield of the scintillators is about 70 photoelectrons/GeV. For small signals even small fluctuations of the photon number can have a large impact on the energy distribution. For example a muon depositing an energy of 400 MeV in a Tile A cell will create about 28 photoelectrons on average. In that energy region the spread of the distribution of the photons reaching the PMTs grows due to the reduced statistics. The correct modeling of the photo statistics in the digitization step of the Monte Carlo simulations has shown to be important for the description of data.

7.3.3 Light attenuation in the Tile calorimeter cells

In the Tile calorimeter cells, the signal is produced by light which is produced by particles passing through the scintillators. The light is collected at both sides of the scintillator. Depending on the particle trajectory through the scintillator, the photons get created at different distances from the fibers. The light is attenuated exponentially as a function of the amount of material it has to pass through. The signal of both readout fibers is combined. Hence, the signal can be described with the sum of two exponential functions. The same amount of scintillating light produced in the middle of the cell creates a signal

in the PMTs which is about 10% lower than if produced on either side close to one of the fibers. This effect is not included in the Monte Carlo, since the exact parameters needed to describe the light attenuation are not known. Since pion showers are rather broad in the Tile Calorimeter, the effect of light attenuation is small for pions.

7.3.4 Recombination effects in LAr for heavily ionizing particles

To compute the measured signal from the energy deposited in a cell the drop of the signal due to charge collection inefficiencies has to be known. Possible reasons are for instance recombination effects. This correction is done in the digitization step. In the default implementation in the ATLAS software this charge collection is modeled as a function of the electric field only. However, there are further recombination effects for energy deposited by particles with high dE/dx which are not modeled per default. These recombination effects are however important for hadronic showers. Due to discrepancies of data and simulations in the LAr calorimeter—especially in the LAr middle layer—the effect of these recombination effects has been studied further.

For hadronic particles with $\beta\gamma$ inferior to about 3 (see fig. 4.1) the stopping power increases sharply. Charged hadrons with those values for $\beta\gamma$ cause a large amount of ionization close to the particle trajectory. A fraction of the electrons will recombine with ions and will not contribute to the signal of the calorimeter cell. Usually this behavior is parametrized with *Birks' law*:

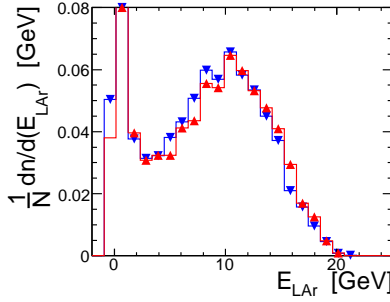
$$R = \frac{Q}{Q_0} = \frac{A}{1 + \frac{k}{\epsilon} \frac{dE}{dx}} \quad (7.7)$$

where A and k are constants and ϵ is the electric field [29–32]. We define $k_Q = k/\epsilon$ and $k_E = k \, dE/dx$. Q_0 is the nominal charge and Q the reconstructed charge.

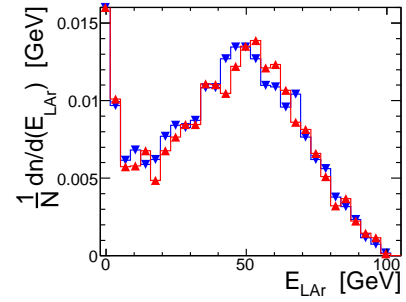
Measurements of ionization (dE/dx) at the ICARUS project using a large LAr time projection chamber (TPC) lead to the values $A = 0.8$ and $k = 0.0486 \, \text{kV/cm} \frac{\text{g/cm}^2}{\text{MeV}}$ for electrical fields up to 500 V/cm [30]. The electrical field in the ATLAS LAr calorimeter is in most regions 10 kV/cm which gives $k_Q = \frac{k}{\epsilon} = 0.00486 \, (\text{g/cm}^2)/\text{MeV}$. The importance of this measurement is that the ICARUS project was the first where the functional form of Birks' law was really validated.

In the RD4 project at CERN, the recombination factor for particles emitted by an α -source and a β -source have been measured [32, 33]. Under the assumption that Birks' law is valid, k_Q can be extrapolated from the data points for an electric field of 10 kV/cm

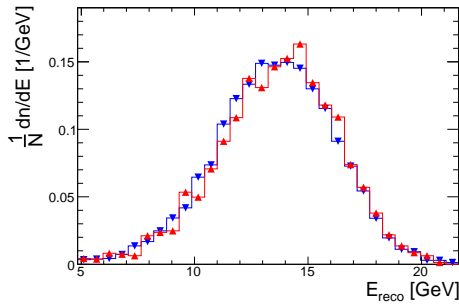
(a) Energy deposited in the LAr calorimeter by 20 GeV pions



(c) Energy deposited in the LAr calorimeter by 100 GeV pions



(d) Energy deposited in LAr and Tile calorimeter by 20 GeV pions



(e) Energy deposited in LAr and Tile calorimeter by 100 GeV pions

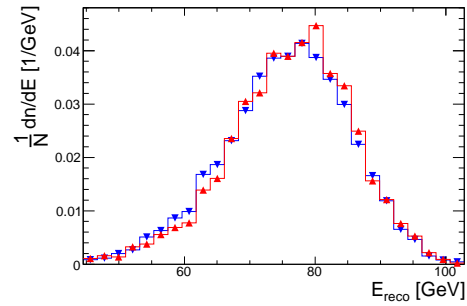


Figure 7.4: Comparison of simulations of 20 GeV and 100 GeV pions with and without Birks' law. The upper figures show the energy deposited in the LAr calorimeter, the figures on the bottom show the energy deposited in LAr and Tile calorimeter. When using Birks' law, for 20 GeV pions, the mean of the energy deposited in the LAr calorimeter (only taking into account events which deposit more energy higher than 3 GeV in the LAr calorimeter) is reduced by a factor 0.97; for 100 GeV (for events depositing more than 10 GeV in the LAr calorimeter) the factor is 0.984.

giving a k_Q which is close to the value from ICARUS.

The dependence of the charge collection on the particle dE/dx has been implemented in addition to the field dependence. The influence of the recombination effects parametrized with the Birks' law in the simulations is shown in fig. 7.4. For the parameter k the value $k = 0.00486 \text{ (g/cm}^2\text{)}/\text{MeV}$ has been chosen. The normalization parameter A has been set to the value $A = 1.0088$ such that the implementation of Birks' law has no effect on the simulation of electrons. This is important, since the recombination effect for electrons as a function of the electrical field have already been taken into account in the detector simulation. Indeed, it has been verified that the normalization factor stayed constant for electrons over the whole energy range.

The effect of this saturation can be observed for events for which the hadron shower has already started in the LAr calorimeter, since only low-energy hadrons produce high energy densities which are subject to saturation effects. The energy deposited in the LAr calorimeter is clearly reduced for those events. The peak at low energy is unchanged, since it corresponds to high energetic pions passing as mips. For 20 GeV the energy above 3 GeV is reduced by 3%, for 100 GeV for events depositing more than 10 GeV by 1.5%. The energy dependence in the reduction factor might be due to the changing electromagnetic content in a hadron shower due to a different relative amount of low energy hadrons at the beginning of the shower [10].

8 Calorimeter calibration

Calibration is the task of relating the raw signal of the measurement to the true quantity which should be measured.

The purpose of this chapter is to give an overview of the calibration procedure for the ATLAS calorimeter. The aim of calorimeters is the measurement of the energy of incoming particles. Those deposit energy in the active and passive material of the calorimeters. In the LAr calorimeter the electric charges created by ionization are collected and in the Tile calorimeter photons created by scintillation are collected and transformed into charges (with PMTs). Hence, the signal is available in the form of electric charges and has to be set into relation to the energy deposited by the incoming particles and further to the energy of the impinging particle.

There are several challenges which have to be met: the signal produced by the calorimeter depends on the particle type. Electrons create a different signal in the calorimeter than hadrons. The calorimeter response for hadrons depends non-linearly on the energy of the particle. The response differs also depending on which part of the shower is measured in the calorimeter. This is an important consideration especially for longitudinally segmented calorimeters like in ATLAS [8].

First the calibration procedure for “electromagnetically interacting particles” (electrons, positrons and photons) on the calorimeter cell level is discussed for the LAr and the Tile calorimeter. Then, the calibration procedure for hadrons is discussed. The calorimeter calibrated for electromagnetically interacting particles provides the basis for the calibration of hadrons. However, since the response of the calorimeter to particles interacting only electromagnetically and to hadrons is different, additional corrections are necessary.

In this chapter all the necessary calibration steps are presented. For hadrons, first the signal that should be calibrated has to be defined by grouping adjacent cells together to form clusters. The calculation of the corrections are then based on the energy, the location, the shape, etc. of the clusters. Correction procedures are presented for the recovery of invisible energy (see sec. 4.4.2), for the recovery of energy deposited outside

of the clusters and for energy deposited in non-active material before the calorimeters, between them and for energy leaking out laterally or longitudinally.

8.1 Calibration of the electromagnetic energy scale

The first step of the calibration aims at deriving the visibly deposited energy in each cell from the measured signal (e.g. electric current, light). This step is called in ATLAS terms: *calibration of the electromagnetic energy scale*.

8.1.1 Liquid Argon calorimeter

The calibration of the LAr calorimeter consists of:

- subtraction of pedestals from the measured signal (definition of zero)
- peak reconstruction from the measured signal via optimal filtering
- calibration of the electronics with an electric current
- transformation of the current (caused by the collected charges) to an energy ($\mu A \rightarrow \text{MeV}$)

The strategy is to extract the calibration from special runs (pedestal runs, calibration runs). The current to energy conversion setting the absolute scale is extracted by using testbeam data and taking corrections into account based on MC-simulations. In ATLAS this can be done by looking at events where a Z -boson is created and decays into an electron positron pair. The precise knowledge of the Z -boson mass can be exploited.

The readout system (see fig. 8.1) consists of a preamplifier which is located outside the cryostat, an analog digital converter (ADC) and a trigger system. To make better use of the dynamic range of the ADC three gains with gain ratios of approximately 1:10:100 are used. The limits for the medium gain are 1300 counts for the low limit and 2500 counts for the high one. To optimize the signal-to-noise ratio, shapers are located after the preamplifiers which transform the triangular signal into a sharp peak and a long undershoot (Fig. 8.2). The amplitude of the peak is proportional to the energy deposited in the cell (Fig. 8.1). The measured signals are kept in an analog storage which can hold up to 144 samples. They are digitized only when the level 1 trigger (LVL1) accepts the event.

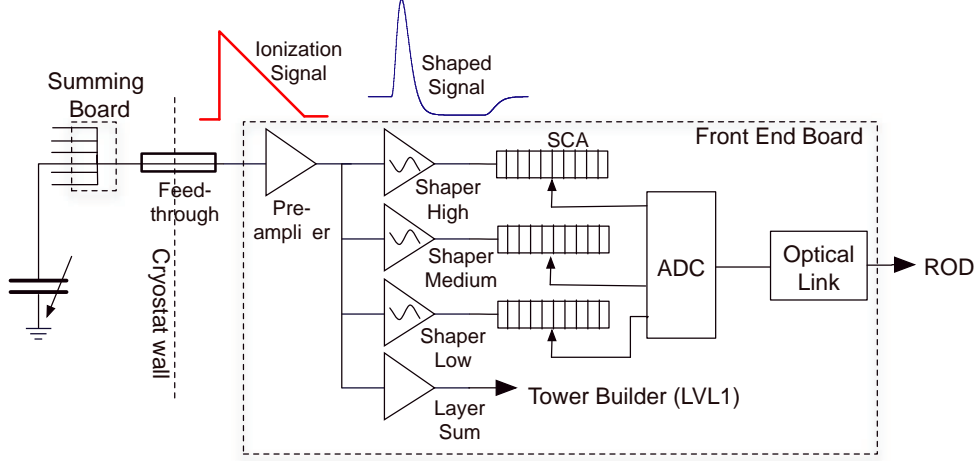


Figure 8.1: Readout chain of the LAr calorimeter.

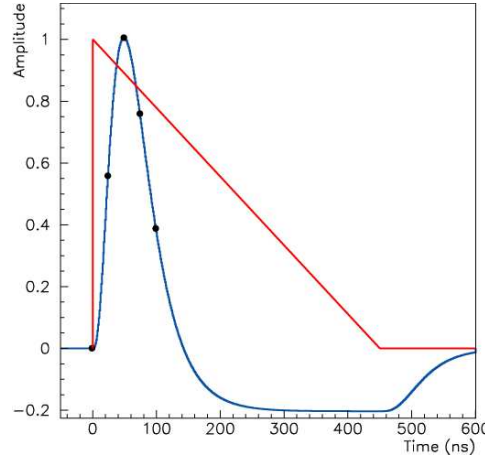


Figure 8.2: Signal shape of a LAr calorimeter cell.

From the shaped signal, the energy has to be computed. For this purpose, the optimal filtering technique [34] is used to calculate the peak while minimizing the contribution of the electronics noise. For the calculation of the OFCs an ansatz for the normalized shape of the signal (and its first derivative) is taken. The pulse shape of each cell is measured from delay runs, where the difference between the trigger time and the data acquisition clock is scanned. The delay run is taken with the pulse. Therefore the pulse shapes correspond to the calibration signal. The noise contribution is given by the noise autocorrelation matrix. For each cell and gain OFCs is computed. The amplitude A and the time offset τ of the signal are then computed using the weighted sums $A = \sum a_i s_i$ and $A\tau = \sum b_i s_i$ where s_i are the pedestal subtracted ADC values in the five read out

bins and a_i, b_i are the energy and time OF coefficients respectively. From the calculated peak of the signal (ADC_{peak}) the energy can be computed as given in [35]:

$$E = F_{DAC \rightarrow \mu A} \cdot F_{\mu A \rightarrow \text{MeV}} \cdot \frac{M_{\text{phys}}}{M_{\text{calib}}} \sum_{i=0,1,2} R_i (ADC_{\text{peak}})^i \quad (8.1)$$

The conversion from DAC (output of the digital analog converter) into MeV is done by two factors. $F_{DAC \rightarrow \mu A}$ depends on the injection resistor on the motherboard and on the properties of the calibration board and $F_{\mu A \rightarrow \text{MeV}}$ corrects for the sampling fraction and also constrains the conversion of current to energy and is thus different for the presampler and accordion part.

The difference in amplitude between the calibration and the physics pulse is taken into account with the factor $M_{\text{phys}}/M_{\text{calib}}$.

During the operation of ATLAS, the measurement of the ionization signal in the cells of the liquid argon calorimeter has to be kept uniform and stable. To ensure this and to correct for imperfections of the read-out chain, a current pulse can be injected for calibration purposes and the response of the electronics can be assessed. A pulse with a known amplitude and a shape similar to an ionization pulse (decay time similar to the drift time in the gap, speed about 1 ns) is injected close to where the current produced by ionization is picked up.

The coefficients R_i are derived by pulsing each cell N_{triggers} times with a set of typically 16 input currents (DAC). The ADC peaks for each of the input currents and each of the samples are measured for all the N_{triggers} triggers and the mean and RMS thereof are calculated. Hence an average calibration wave for each of the DAC values is obtained. The ADC_{peak} for all waves is computed and the parameters R_i are derived assuming the relation:

$$DAC = R_0 + R_1 ADC_{\text{peak}} + R_2 ADC_{\text{peak}}^2. \quad (8.2)$$

8.1.2 Tile calorimeter

The light signal created in the Tile scintillators amplified and converted into a charge at the PMTs anodes (see sec. 3.3.2). This signal represents the physics signal and is subsequently read out and digitized every 25 ns (Fig. 8.3). When the trigger accepts the signal, 9 samples are used to reconstruct the signal. The amplitude of the pulse is (after the calibration) proportional to the energy deposited in the cells.

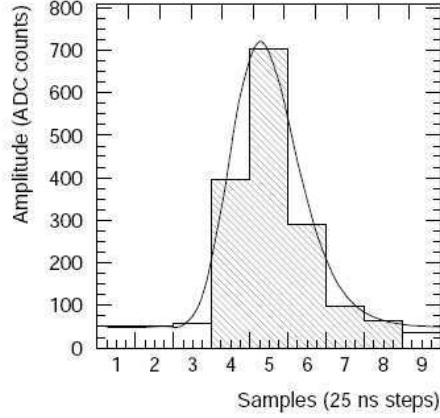


Figure 8.3: An example of signal of a Tile calorimeter cell at the output of a PMT. Nine samples are taken in steps of 25 ns. A fit of the measured pulse shape (line) is applied to the measured samples and the amplitude and the time are computed.

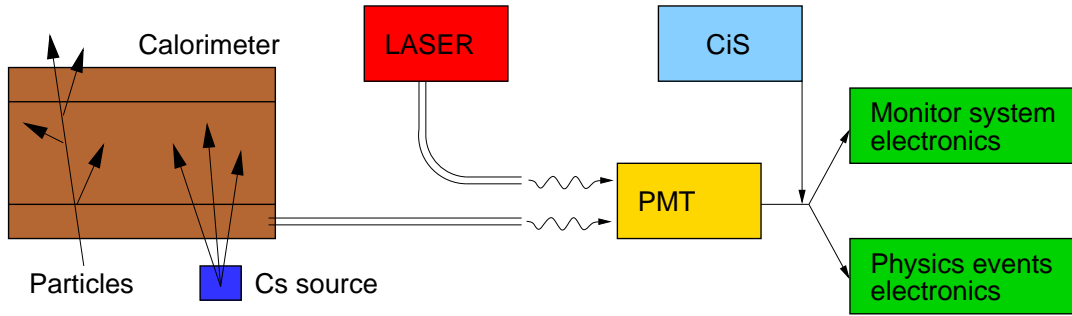


Figure 8.4: Tile Calorimeter calibration system.

For the Combined Testbeam 2004, the amplitude and the time of the signal are computed using the so called "fit method". A pulse shape extracted from the CTB data is adjusted to the first sample until the third samples after the peak. The amplitude, the time at which the pulse is maximal and the pedestal are extracted. In ATLAS presently the use of optimal filtering (as for the LAr calorimeter) is proposed to minimize the influence of the noise. For the CTB this technique has not been available yet.

Regular calibration of the cells of the Tile calorimeter is necessary due to several factors which can change the response of the cells. Aging and radiation damage of the scintillators and fibers can reduce the light yield. The PMT response can also change due to gain drifts.

The calibration (and monitoring) strategy for the Tile Calorimeter relies on three systems: *Cs*, *LASER* and *CiS* (charge injection system) shown in fig. 8.4.

Cs stands for a movable radioactive source (^{137}Cs) which is moved through a tube which passes through all cells. The source emits gamma-rays and thus produces a signal which is very similar to one produced by particles coming from physics events from LHC interactions. The Cs system is used to equilibrate the high voltage in the PMTs before data taking. The Cs calibration is done a few times per year. The Cs system uses a different read-out. Therefore the main purpose of the Cs calibration system is the inter-calibration of the individual cells.

The LASER system produces light pulses on each PMT. The signal imitates the light pulses originating from the calorimeter cells. The LASER system has not been operational during the CTB.

The last step of the calibration strategy is the injection of a known charge into the read-out electronics. The signal measured by the electronics is compared to the injected signal and calibration parameters can be derived for each cell. So far a linear relation between the injected and the measured charge had been assumed. Using the analysis of the CTB data, a non-linear behavior of the electronics in the low region of the low gain due to a cross-talk between the low and the high gain has been found. A correction for this effect has been worked out, and is applied in the data analyses [36].

The absolute electromagnetic scale is set in testbeam runs where electrons are directly impinging on the Tile calorimeter. In the 2002 testbeam 30% of the modules have been calibrated in this way. The conversion factor from pC to GeV was found to be 1.05 with a variation between the modules of 2% [37].

8.2 Calibration of the hadronic energy scale (energy measurement)

The ATLAS hadronic calibration scheme takes as input the calibrated calorimeter cell energies as described in sec. 8.1. Cells with energy deposits above certain thresholds are clustered with a topological clustering algorithm. The visibly deposited energy of each cluster is weighted to get the true cluster energy (visible and invisible energy). Subsequently the true energy which is deposited outside the clusters and the true energy deposited in the dead material is estimated (see fig. 8.5). Weighting, out-of-cluster corrections and dead material corrections are derived from MC simulations where the true energy deposits in each region of the calorimeter are known. The calorimeter is calibrated with a detailed MC simulation of a number of effects that have to be corrected

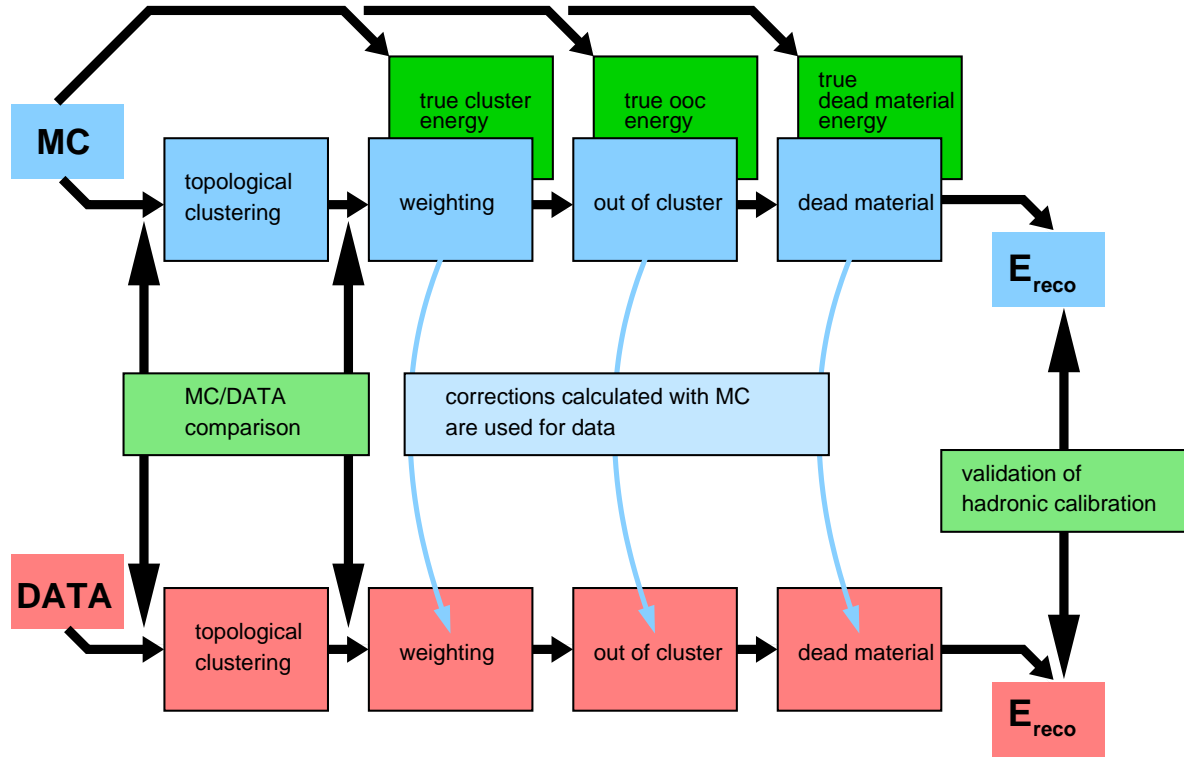


Figure 8.5: Schematic showing the steps to arrive at a fully calibrated pion energy through local hadronic calibration. The visibly in the calorimeters deposited energy (cell energies) is clustered with a topological clustering algorithm. Monte Carlo simulations (MC) provide the true cluster, out-of-cluster (ooc) and dead material energies, such that corrections for each of these energies can be derived with a large number of MC simulations covering the whole range of beam energies. For a specific simulation, the corrections can be computed and added to the visibly deposited energy which gives the reconstructed energy E_{reco} . Data is treated as MC using the corrections derived from MC. To be able to use MC for the calibration of data, it has to be assured, that MC and data are in adequate agreement. Hadron showers of MC and data from different beam energies are therefore compared. After the calibration chain, the results for the reconstructed energy of MC and data are compared to validate the hadronic calibration scheme.

as described in the following chapters. In the testbeam the corrections are validated by applying them on data and by comparing them to the known beam energies.

The accuracy of the hadronic calibration depends therefore on how precise the data are described by the MC simulations. The data and the MC simulation are compared at the cell level and after clustering the cells using the topology of the cells (see sec. 9). This task aims at finding remaining software problems, determining the physics list which describes data best and testing the accuracy of the calibration to the electromagnetic energy scale.

With MC simulations the improvement of each step of the hadronic calibration on the energy measurement can be evaluated. Since the MC simulations describe the data only to a certain level of accuracy it has to be assured, that the corrections for invisible energy, energy deposited outside of the clusters and dead material energy derived from MC work on data. Hence, the reconstructed energy E_{reco} after all calibration steps has to be compared for data and MC (see sec. 10).

8.2.1 Topological clustering

In ATLAS, particles originating from the interaction point (IP) create showers which deposit energy in the calorimeter cells. The signal is superimposed by noise which deteriorates the resolution of the measured signal. The aim of *topological clustering* (topocluster) is to separate signal from noise by clustering adjacent cells with a signal above the noise level while keeping most of the signal. The topological clustering is based on the idea, that the true energy deposits are correlated. A cell with a lower signal which is neighbour to a cell with a higher signal is more likely to contain signal than if that cell would be isolated. After the formation of the clusters, they can be analyzed geometrically (e.g., radius, length, position) and topologically providing information about the shower shape which can be exploited for the (hadronic) energy calibration.

The ATLAS topocluster algorithm is sub-detector independent and is able to collect cells in two dimensions (within the layers) and three dimensions (across layers and sub-detectors). The way cells are collected can be defined in detail for each detector separately. In the same layer the 8 cells surrounding a cell with $\Delta i_{\eta,\phi} = 0, \pm 1$, in adjacent layers, cells which are partially overlapping in η and ϕ and in cells in other calorimeters with adjacent layers which are partially overlapping in η and ϕ are considered as topological neighbours.

Topological clustering forms clusters around cells whose signal are above a certain noise threshold which can be adjusted.

The principle of the topocluster algorithm is described in the following:

- search for the most energetic cell with $|E_{\text{cell}}^{\text{reco}}| > S\sigma_{\text{noise}}$
- add all neighbouring cells (and their neighbouring cells) to the cluster if $|E_{\text{cell}}^{\text{reco}}| > N\sigma_{\text{noise}}$
- add all direct neighbours of collected cells if $|E_{\text{cell}}^{\text{reco}}| > P\sigma_{\text{noise}}$

where σ_{noise} is the noise level in the cell. The coefficients S (*seed*), N (*neighbour*) and P (*perimeter*) are adjusted such that most cells containing signal are clustered while cells only measuring noise are omitted. Cells which are added to a cluster are not considered for other clusters any more. These steps are repeated until no more cells with $|E_{\text{cell}}^{\text{reco}}| > S\sigma_{\text{noise}}$ are remaining.

After the clusters are built, a further algorithm searches in each cluster for local maxima in the layers 2 and 3 of the LAr Barrel and in FCAL 1 (can be configured). Those clusters are then separated by an algorithm that splits large clusters (`ClusterSplitter`) around each of the local maxima. The behaviour of the cluster splitter can be tuned in terms of thresholds for neighbouring cells. Cells of cluster borders in equal distance to multiple maxima can be shared by the clusters.

Cluster moments

Beside the energy deposition in the calorimeter layers, the topology of the showers provides information about their nature and can thus be exploited for corrections like weighting, out-of-cluster correction and dead material corrections. The shower topology can be described by the so called *cluster moments* which are defined by

$$\langle x^n \rangle = \frac{1}{E_{\text{norm}}} \cdot \sum_{\{i | E_i > 0\}} E_i x^n \quad (8.3)$$

with the normalization

$$E_{\text{norm}} = \sum_{\{i | E_i > 0\}} E_i. \quad (8.4)$$

where n is the degree of the moment and x the observable. The moment is calculated with the constituent cells of the cluster. Only cells with a positive cell energy enter the computation of the moments to prevent unphysical results. Exceptions are the moments for the observables η and ϕ where the absolute values of the cell energies are used.

Some of the moments refer to the shower axis which can be calculated by a principal value analysis of the energy weighted spatial correlation with respect to the center of

the cluster of the cluster constituent cells. Only cells with positive energy are taken:

$$C_{xx} = \frac{1}{w} \sum_{\{i|E_i>0\}} E_i^2 (x_i - \langle x \rangle)^2, \quad (8.5)$$

$$C_{xy} = \frac{1}{w} \sum_{\{i|E_i>0\}} E_i^2 (x_i - \langle x \rangle) (y_i - \langle y \rangle), \quad (8.6)$$

where the normalization constant is calculated with

$$w = \sum_{\{i|E_i>0\}} E_i^2. \quad (8.7)$$

The other components C_{xz} , C_{yy} , C_{yz} , C_{zz} are calculated according to C_{xx} and C_{xy} and can be combined in the symmetric matrix:

$$C = \begin{pmatrix} C_{xx} & C_{xy} & C_{xz} \\ C_{xy} & C_{yy} & C_{yz} \\ C_{xz} & C_{yz} & C_{zz} \end{pmatrix}. \quad (8.8)$$

With \vec{i} being the vector from the interaction point (IP) to the barycenter of the cluster and $e_{0,1,2}$ the eigenvectors of C , the shower axis \vec{s} is given by:

$$\vec{s} = \begin{cases} \vec{e}_{0,1,2} \text{ with smallest } \angle(\vec{i}, \vec{e}_{0,1,2}), & \text{if } \angle(\vec{i}, \vec{e}_{0,1,2}) \leq 30^\circ \\ \vec{i}, & \text{if } \angle(\vec{i}, \vec{e}_{0,1,2}) > 30^\circ \end{cases} \quad (8.9)$$

With the shower center \vec{c} and the shower axis \vec{s} the distance of a cell i to the cluster center along the shower axis

$$\lambda_i = (\vec{x}_i - \vec{c}) \cdot \vec{s}, \quad (8.10)$$

and the radial distance of a cell i to the shower axis

$$r_i = |(\vec{x}_i - \vec{c}) \times \vec{s}| \quad (8.11)$$

can be defined.

The following moments are calculated in addition to \vec{c} :

- $\langle \phi \rangle$ (`phi`), the first moment in ϕ
- $\langle \eta \rangle$ (`eta`), the first moment in η

- $\langle r^2 \rangle$ (`m2_r`), the second moment in r
- $\langle \lambda^2 \rangle$ (`m2_lambda`), the second moment in λ
- $\langle \rho \rangle$ (`m1_dens`), the first moment in energy density $\rho = E/V$
- $\langle \rho^2 \rangle$ (`m2_dens`), the second moment in energy density

and several quantities to estimate shower properties are computed:

- λ_{center} (`center_lambda`), the distance of the shower center from the calorimeter front face measured along the shower axis
- f_{em} (`eng_frac_em`), the energy fraction in EM calorimeters
- f_{max} (`eng_frac_max`), the energy fraction in the most energetic cell
- f_{core} (`eng_frac_core`), the sum of the energy fractions in the most energetic cells per layer
- isolation (`isolation`), the layer energy weighted fraction of non-clustered neighbor cells on the outer perimeter of the cluster

and with the definitions:

$\text{lat}_2 = \langle r^2 \rangle$, with $r = 0$ cm for the two most energetic cells

$\text{lat}_{\text{max}} = \langle r^2 \rangle$, with $r = 4$ cm for the two most energetic cells and $r = 0$ cm for all other cells

$\text{long}_2 = \langle \lambda^2 \rangle$, with $\lambda = 0$ cm for the two most energetic cells

$\text{long}_{\text{max}} = \langle \lambda^2 \rangle$, with $\lambda = 10$ cm for the two most energetic cells and $\lambda = 0$ cm for all other cells

- lateral (`lateral`), $\frac{\text{lat}_2}{\text{lat}_2 + \text{lat}_{\text{max}}}$, the normalized second lateral moment
- longitudinal (`longitudinal`), $\frac{\text{long}_2}{\text{long}_2 + \text{long}_{\text{max}}}$, the normalized second longitudinal moment

The names put in parentheses denote the names of the moments and estimators as used in the reconstruction program code and as used in the labels of the figures.

Evaluation of the noise thresholds for cluster creation with the CTB

The aim of topological clustering is to collect as many cells with signal as possible and add them up to clusters while excluding cells only measuring noise. Three parameters S (*seed*), N (*neighbour*) and P (*perimeter*) can be adjusted to optimize this behavior. An evaluation of several combinations of those three parameters has been undertaken on data.

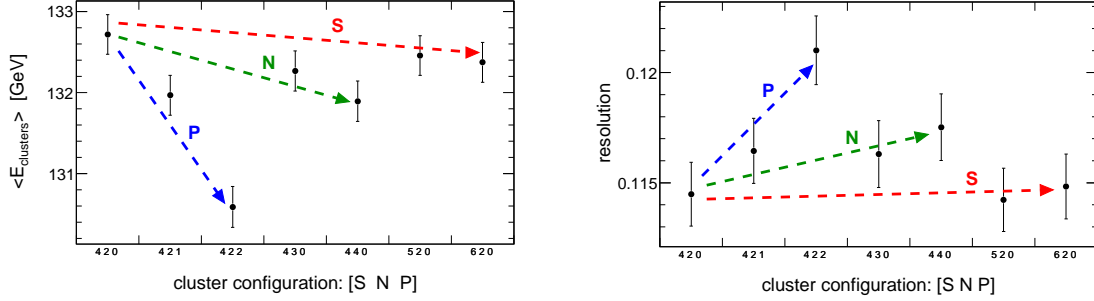
Fig. 8.6 shows the mean and the resolution of the distributions of the energy deposited in all clusters ($E_{\text{clusters}} = \sum_{cl}^{N_{\text{clusters}}} E_{cl}$, where E_{cl} is the energy deposited in a particular cluster and N_{clusters} is the number of clusters created in the event) depending on the cluster configuration for a beam energy of 180 GeV and 20 GeV respectively. The x -axes of the figures show the tested cluster configurations [S N P].

For the parameter S (*seed*) the three parameters 4, 5 and 6 have been tested. The *seed* parameter S will not affect the size of the cluster itself, but only if a certain cluster is generated or not. A value S chosen too low will create more clusters, many of them only containing noise and thus impairing the energy resolution. If the value for S is chosen too high, parts of the signal - especially showers with a small electromagnetic content - will not be clustered and therefore not considered, this will affect adversely the linearity of the energy measurements with the calorimeters. The tendency for the change of mean value and resolution as a function of S is indicated by the red arrow marked with "S". For the mean value a slight decrease can be seen and the resolution gets slightly worse with increasing S . The best choice for the seed parameter S has been found to be 4.

For the parameter N (*neighbour*) three values 2, 3 and 4 are tested for 180 GeV beam energy and additionally 1 for 20 GeV beam energy. A clear decrease of the mean energy can be noticed with higher N . The higher threshold for the clustering of neighbouring cells hence leaves some fraction of cells containing signal unclustered. The resolution generally gets worse when increasing N , but in fig. 8.6d a worsening for the resolution is as well seen when reducing the threshold to 1. Trading off the mean value of the energy in the clusters and its resolution $N = 2$ is the best choice.

The third parameter P defines the threshold for a further slice of cells. Direct neighbours of all cells belonging to the cluster are considered. They are collected when passing the threshold $|E_{\text{cell}}^{\text{reco}}| > P \cdot \sigma_{\text{noise}}$. A threshold $P = 0$ means therefore, that all cells adjacent to cluster-cells are added to the cluster regardless of their energy. On the other hand, a threshold $P \geq N$ turns off this behaviour as all cells fulfilling this constraint are yet

- (a) Average of the energy deposited in all clusters by 180 GeV pions (b) Resolution of the distribution of the energy deposited in all clusters by 180 GeV pions



- (c) Average energy deposited in all clusters by 20 GeV pions (d) Resolution of the distribution of the energy deposited in all clusters by 20 GeV pions

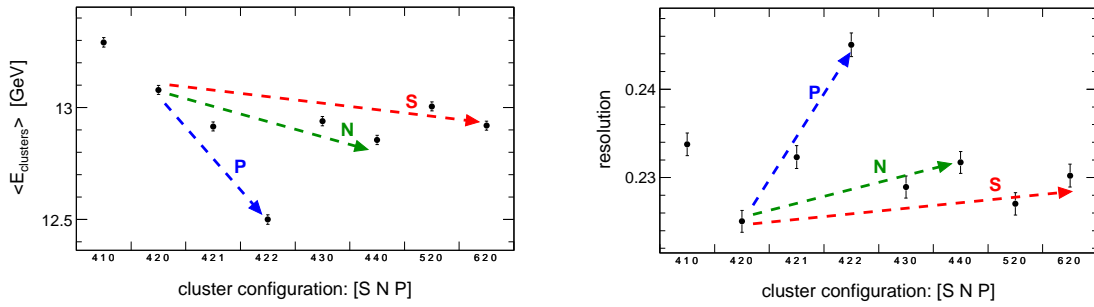


Figure 8.6: Mean values ($\langle E_{\text{clusters}} \rangle$) and resolution ($\text{RMS}/\langle E_{\text{clusters}} \rangle$) of the distributions of the energy deposited in all clusters by pions (π^-) with an energy of 20 GeV and 180 GeV (y -axes) in dependence of the noise thresholds set for seed-, neighbour- and perimeter-cells (x -axes). The tendencies of how $\langle E_{\text{clusters}} \rangle$ and $\text{RMS}/\langle E_{\text{clusters}} \rangle$ change in function of the thresholds are indicated with arrows marked with S, N and P for the seed, neighbour and perimeter threshold, respectively. For 20 GeV pions, the highest mean value is achieved with the configuration [S P N]=[4 1 0] (c), but with this configuration, the resolution is considerably worse than for [S P N]=[4 2 0]. Hence, lowering the threshold N below 2 leads to the collection of more cells and thus more energy, but impairs the resolution. Except from the configuration [S P N]=[4 1 0] the highest mean value and at the same time one of the narrowest energy distributions is achieved with [S P N]=[4 2 0]. Starting from [S P N]=[4 2 0] and increasing one of the parameters, less energy is collected for the clusters and their resolutions get worse.

part of the cluster. An increase of P from 0 to 2 leads to a reduction of E_{clusters} while the resolution gets worse. The best choice for P is therefore 0. All cells which are in the direct neighborhood of cluster cells are therefore added to that cluster.

The conclusion of the evaluation of different cluster configurations is, that [S N P]=[4 2 0] is the best choice in terms of clustering signal but omitting noise.

8.2.2 Weighting correction for invisibly deposited energy

For hadronic showers a fraction of, on the average, about 30% (depending on the incident energy) of the energy is deposited invisibly (e.g., break-up of nuclei, nuclear excitation, production of neutrons) or escapes through particles like muons and neutrinos. This fraction is subject to large fluctuations from event to event. It becomes relatively smaller at higher beam energy. The role of the weighting is to estimate the invisibly deposited energy for each event from the visibly deposited energy and correct for it.

In the ATLAS detector simulation four categories of energy depositions are distinguished: *visible electromagnetic energy*, *visible non-electromagnetic energy*, *invisible energy* and *escaped energy* (as described in sec. 4.4.2). The deposited energy in each of the four categories is computed for each cell. The weights (w) are computed from MC simulations by dividing the total true deposited energy ($E_{\text{cell,total}}^{\text{true}}$, sum of all calibration hits in active and inactive material) by the reconstructed cell energy ($E_{\text{cell}}^{\text{reco}}$):

$$w = \frac{E_{\text{cell,total}}^{\text{true}}}{E_{\text{cell}}^{\text{reco}}} . \quad (8.12)$$

The reconstructed cell energy is the energy which is reconstructed from the visible energy (i.e. it contains the sampling fraction and the noise contribution). The true deposited energy is known through the so called *CalibrationHits* mechanism (see sec. 5.6), which stores the true energy deposits in special containers. For the Combined Testbeam 2004, specific simulations with the testbeam geometry have been produced for single pions and single protons (to account for the proton contamination in the testbeam) to calculate the true energy deposited in the calorimeters.

In ATLAS for the computation of the weights the clusters of each event are classified as electromagnetic or non-electromagnetic (hadronic) (“em-classification”) using moments which are correlated to the electromagnetic component of the cluster. Such moments are the second moment in r ($\langle r^2 \rangle$), the second moment in λ ($\langle \lambda^2 \rangle$) and the distance from the calorimeter front face to the barycenter of the cluster (cluster moments: see

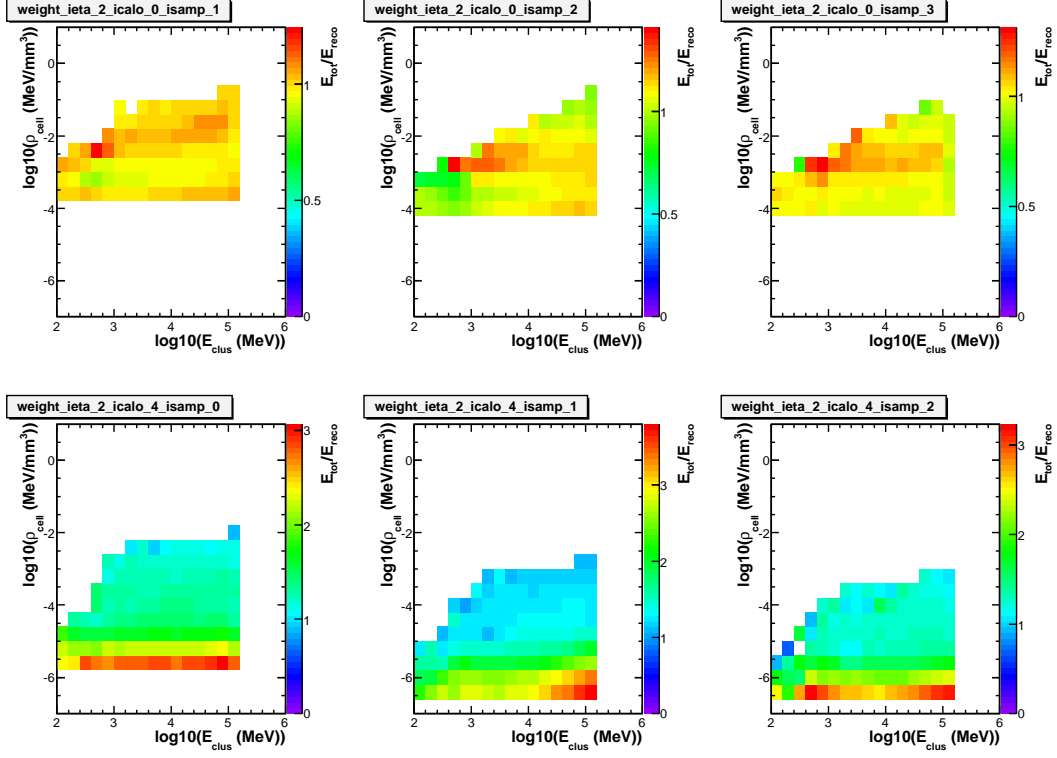


Figure 8.7: Hadronic cell weights in the η -region around 0.4 ($i_{\text{eta}}=2$) for the layers 1,2 and 3 (i_{samp}) for the LAr calorimeter ($i_{\text{calo}}=0$) and the samples A, BC and D (0,1,2) for the Tile calorimeter ($i_{\text{calo}}=4$). The x -axis shows the logarithm to base 10 for the cluster energy E_{clus} , on the y -axis the logarithm to the base 10 of the energy density of the cell ρ_{cell} is plotted and the colors denote the weights $E_{\text{cell},\text{total}}^{\text{true}}/E_{\text{cell}}^{\text{reco}}$. The weights are derived for the CTB for pions with energies ranging from 15 GeV to 230 GeV.

sec. 8.2.1). The main purpose of this em-classification is to avoid that neutral pions accompanying the charged pions in the jets are weighted. Neutral pions lead to pure em deposits and should therefore not be weighted. This classification is not done in the CTB, since the hadronic weighting scheme is tested on particle beams which contain single charged pions and the remaining electron contamination is negligible.

Clusters which have been classified as hadronic are taken for the computation of the weight tables. From the clusters only cells whose reconstructed energy is above $2\sigma_{\text{noise}}$ and their true energy is above σ_{noise} are taken into account to calculate the cell weight, where σ_{noise} is the electronics noise level of the cell. These cuts are applied in order to prevent noise from distorting the weight table. Cells from the presampler are not weighted, since they are only used for correction of dead material losses.

For the calibration procedure, the ATLAS calorimeter is divided into 25 equidistant $|\eta|$ -bins from 0.0 to 5.0. For the CTB only the first 9 bins are used and in the present analysis only one bin is used. The weight tables are filled with the ratios between the calibration hits produced in the cells divided by the reconstructed energy of the cell ($E_{\text{cell,total}}^{\text{true}}/E_{\text{cell}}^{\text{reco}}$). The bin of the weight table is chosen as a function of the cell's energy density $\rho_{\text{cell}} = E_{\text{cell}}^{\text{reco}}/V_{\text{cell}}$ (V_{cell} is the volume of the cell), the energy of the cluster the cell belongs to and the $|\eta|$ of the center of the cell. For both, the cluster energy and the energy density of the cell, the logarithm to the base 10 is taken. Fig. 8.7 shows the weight tables derived for the CTB for pions in the η -region around 0.4 ($i_{\text{eta}}=2$) and for the layers (i_{samp}) 1,2 and 3 for the LAr calorimeter ($i_{\text{calo}}=0$) and the samples A, BC and D for the Tile calorimeter ($i_{\text{calo}}=4$).

8.2.3 Out-of-cluster corrections

A certain part of the energy which is deposited in the calorimeters is not taken into account by the topological clustering algorithm. This is caused by energy deposits which are spatially separated from the clusters and which do not pass the noise thresholds. Another part of the energy which is not contained in the clusters is caused by particles leaking out of the simulated spatial region ("escaped" energy; see sec. 4.4.2). The amount of energy which is not measured due to these two contributions has to be estimated.

The out-of-cluster (ooc) energy is defined as the beam energy minus the true total energy deposited in the clusters in the calorimeter and the total true energy deposited in the dead material. The energy which is deposited out of the clusters can be quantified exactly in the MC simulations. The mean ooc energy divided by the total in the clusters deposited energy as a function of the energy weighted barycenter of the clusters of each event and the η of the incident particle is stored in a weight table.

At the reconstruction, the ooc energy value is retrieved for each event and has to be split up and assigned to the clusters. The part of the ooc energy which is assigned to each cluster depends on the cluster energy and on the isolation of the cluster. To those which are surrounded by many other clusters a smaller part of the energy is assigned than to those which are not in the proximity of other clusters. The ($i_{\text{isolation}}$) moment (see sec. 8.2.1) is taken as a measure for the isolation of a cluster.

8.2.4 Dead material corrections in ATLAS

The total length of the ATLAS calorimeters (radius) is chosen such that only a small fraction of the energy of electromagnetic and hadronic showers leaks out of the calorimeter and most energy is deposited within the detectors (except energy which is lost through particles like ν and μ which deposit only a small amount of energy in the calorimeter). Nevertheless there are some regions in the detector where the deposited energy is not measured, called dead material (DM) such as Inner Detector material and cryostat walls. This energy loss deteriorates linearity, uniformity and resolution of the energy measurement of the calorimeters and thus has to be corrected for. The amount of energy lost in the dead material is determined with ATLAS Monte-Carlo simulations of single pions. Similar to the weighting (sec. 8.2.2) the true energy deposited in the dead material is collected with the *CalibrationHits* mechanism.

In the default method foreseen for the ATLAS detector the dead material corrections are applied at the cluster level. Each cluster is classified as electromagnetic or hadronic using cluster variables (moments) and the corresponding dead material correction is chosen and added to the cluster energy.

Fig. 8.8 shows the average energy deposited in the dead material in ATLAS by 500 GeV pion showers (20000 events). The dead material regions are marked with their respective region codes. Several regions can be identified, such as the Inner detector material, the crack regions between the detector subsystems (e.g., LAr/Tile, Tile Barrel/Tile Extended Barrel, Tile Extended Barrel/ECAL) and leakage. The most important for the Combined Testbeam 2004 are the material upstream before the LAr calorimeter, between Presampler and Strips (important mainly for electron showers) and between the LAr and the Tile calorimeter (important mainly for hadron showers).

In ATLAS, the dead material corrections are computed with MC simulations of single pions where all energy which is deposited in one event in dead material has its origin in the single pion even if the particle causes more than one cluster to be created. In reality we expect many particles or jets depositing energy distributed in the different detector systems and dead material regions. Hence, many clusters will be created all over the ATLAS calorimeter system and the DM corrections cannot be applied on the event level but rather have to be attributed to each cluster. Yet at the stage of computation of the dead material corrections with single pions an algorithm has to be designed which decides which fraction of DM energy is assigned to each cluster. One possibility is to rely on neighbourhood relations and try to find the closest cell to a DM calibration hit

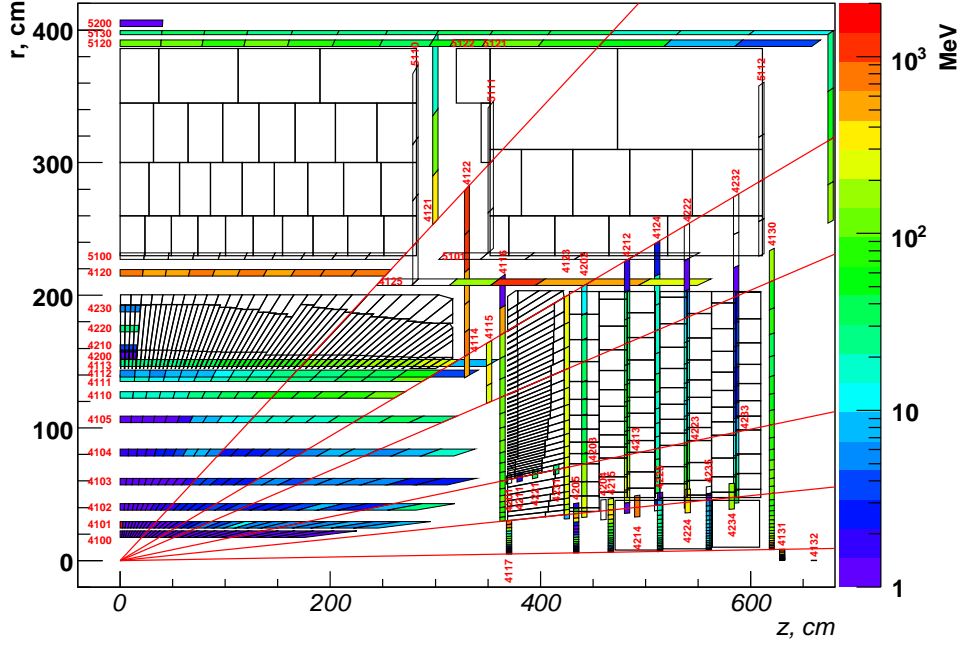


Figure 8.8: Sketch of the ATLAS calorimeters. The colored cells show the average energy deposited in the dead material by 20000 negative single pion events. The energy of the impinging pions is 500 GeV. The red numbers denote the dead material region code.

as explained in the following section. On page 95 an iterative approach is presented to relate cluster quantities (e.g., cluster moments, cluster energy deposited in a layer) to dead material corrections. For the CTB it is possible to simplify the problem of DM corrections by applying them on the event level only (see sec. 8.2.4).

Assignment of the dead material calibration hits to the clusters

The energy deposited in the dead material is a property of the event. Typically more than one cluster is created for a single pion event. The energy deposited in the dead material has to be assigned to the clusters. Part of the DM energy can be assigned to clusters neighboring the DM energy deposits (depending on the granularity of the calorimeter in that region and the η and Φ position of the cells and the calibration hits). For calibration hits which are in the direct neighborhood of more clusters a fraction of the energy is assigned to each of the clusters. The energy of the calibration hits is split up between the clusters depending on the energy in the cluster-cells which are closest to the calibration hits. Hence, no double counting of energy occurs. About 10% to 30% of DM energy is left unassigned by this procedure and assigned to the clusters depending on

their energy and the distance to the calibration hit. After this step, the dead material weights can be calculated for each cluster taking its visibly deposited energy and the assigned DM calibration hits.

Computation of the dead material corrections

Depending on the regions of the ATLAS calorimeter, different ways are used to compute the DM corrections.

Where good correlations between cluster quantities and energy deposits in dead materials can be established parameterizations with first order polynomials are used. The dead material corrections are correlated to either a presampler signal in that region or to the square root of the product of the enclosing calorimeter layers. The formulae are shown in eq. 8.13. *off* (offset) and *sl* (slope) of the parameterizations depend on their classification as electromagnetic or hadronic (c_{class}), the cluster energy E_{cl} and the pseudo rapidity of the cluster η_{cl} . The coefficients are obtained with linear fits from MC:

$$E_{\text{DM:Barrel,Upstream-PS-Strips}} = \text{off}(c_{\text{class}}, E_{\text{cl}}, \eta_{\text{cl}}) + \text{sl}(c_{\text{class}}, E_{\text{cl}}, \eta_{\text{cl}}) \cdot E_{\text{PresamplerBarrel}} \quad (8.13)$$

$$E_{\text{DM:Barrel,LAr-Tile}} = \text{off}(c_{\text{class}}, E_{\text{cl}}, \eta_{\text{cl}}) + \text{sl}(c_{\text{class}}, E_{\text{cl}}, \eta_{\text{cl}}) \cdot \sqrt{E_{\text{LAr3}} \cdot E_{\text{Tile A}}}$$

$$E_{\text{DM:Barrel-Ext.Barrel,Tile}} = \text{off}(c_{\text{class}}, E_{\text{cl}}, \eta_{\text{cl}}) + \text{sl}(c_{\text{class}}, E_{\text{cl}}, \eta_{\text{cl}}) \cdot E_{\text{TileGap3}}$$

$$E_{\text{DM:EMEC,Upstream}} = \text{off}(c_{\text{class}}, E_{\text{cl}}, \eta_{\text{cl}}) + \text{sl}(c_{\text{class}}, E_{\text{cl}}, \eta_{\text{cl}}) \cdot E_{\text{PresamplerEMEC}}$$

$$E_{\text{DM:EMEC3-HEC0}} = \text{off}(c_{\text{class}}, E_{\text{cl}}, \eta_{\text{cl}}) + \text{sl}(c_{\text{class}}, E_{\text{cl}}, \eta_{\text{cl}}) \cdot \sqrt{E_{\text{EMEC3}} \cdot E_{\text{HEC0}}}$$

In regions without presampler and thicker layers enclosing the dead material, it is more difficult to get a good estimation of the energy lost in the dead material (before FCAL and the crack between HEC and FCAL). There, the DM correction is done by adjusting the weights for the layers such that they account not only for the invisibly deposited energy inside the cluster, but as well for the energy lost in the dead material.

For the material in the η -region between 1.8 and 3.2 in front of the accordion structure, in the cracks between the calorimeter modules, for leakage downstream of the calorimeter systems and for low energetic clusters a third approach is chosen for the computation of the dead material corrections. The quantity $\langle E_{\text{DM}}/E_{\text{cl}} \rangle$ is stored in dependence of their classification as electromagnetic-like or hadronic-like, their cluster energy, their cluster depth and their pseudo rapidity in a four dimensional lookup table.

Parametrization of the energy loss in dead material

For the Combined Testbeam 2004 a dedicated parametrization based on the energy deposited per event in the calorimeter layers not considering the individual clusters has been developed (*CTB method*). This type of dead material correction simplifies the problem, since the assignment of the dead material correction to individual clusters does not have to be addressed, but can only be applied to testbeam data. The dead material regions which exist for the Combined Testbeam 2004 are in front of the LAr calorimeter (*Upstream*), between Presampler and Strips *PSStrips*, between LAr and Tile calorimeter *LArTile* and behind the Tile calorimeter *Leakage*.

The corrections are parameterized according to the formulae in eq. 8.14:

$$\begin{aligned}
 E_{\text{DM,Upstream}}(E_{\text{beam}}) &= c_1(E_{\text{beam,n}}) \cdot E_{\text{Presampler}} \\
 E_{\text{DM,PSStrips}}(E_{\text{beam}}) &= c_2(E_{\text{beam,n}}) \cdot \sqrt{E_{\text{Presampler}} \cdot E_{\text{Strips}}} \\
 E_{\text{DM,LArTile}}(E_{\text{beam}}) &= c_3(E_{\text{beam,n}}) \cdot \sqrt{E_{\text{LAr3}} \cdot E_{\text{Tile A}}} \\
 E_{\text{DM,Leakage}}(E_{\text{beam}}) &= c_4(E_{\text{beam,n}}) .
 \end{aligned} \tag{8.14}$$

The coefficients c_1, c_2, c_3, c_4 are computed for a number of different beam energies. They have a small beam-energy dependence, which is parameterized and fitted according to eq. 8.15:

$$\begin{aligned}
 c_1(E_{\text{beam,n}}) &= c_{1,A} \\
 c_{2,3,4}(E_{\text{beam,n}}) &= c_{2,3,4,A} + c_{2,3,4,B} \cdot E_{\text{beam,n}} + c_{2,3,4,C} \cdot E_{\text{beam,n}}^2 \\
 \frac{e}{\pi}(E_{\text{beam,n}}) &= c_{5,A} + c_{5,B} \cdot E_{\text{beam,n}} + c_{5,C} \cdot E_{\text{beam,n}}^2 .
 \end{aligned} \tag{8.15}$$

Since the beam energy is not a priori known, the DM corrections have to be calculated using an iterative procedure. Starting at an initial assumption of $E_{\text{estimate},0} = E_{\text{reco,em}}$, where $E_{\text{reco,em}}$ is the sum of the reconstructed energy in all calorimeter clusters at the electromagnetic scale, the estimated energy is calculated as:

$$\begin{aligned}
 E_{\text{estimate},n+1} &= E_{\text{DM,Upstream}}(E_{\text{estimate},n}) + E_{\text{DM,PSStrips}}(E_{\text{estimate},n}) + \\
 &\quad E_{\text{DM,LArTile}}(E_{\text{estimate},n}) + E_{\text{DM,Leakage}}(E_{\text{estimate},n}) + \\
 &\quad \frac{e}{\pi}(E_{\text{estimate},n}) \cdot E_{\text{reco,em}} .
 \end{aligned} \tag{8.16}$$

To get a correct estimate of the beam energy, $E_{\text{reco,em}}$ is weighted with an beam-energy dependent e/π factor which is parameterized according to eq. 8.15. The e/π factor is a

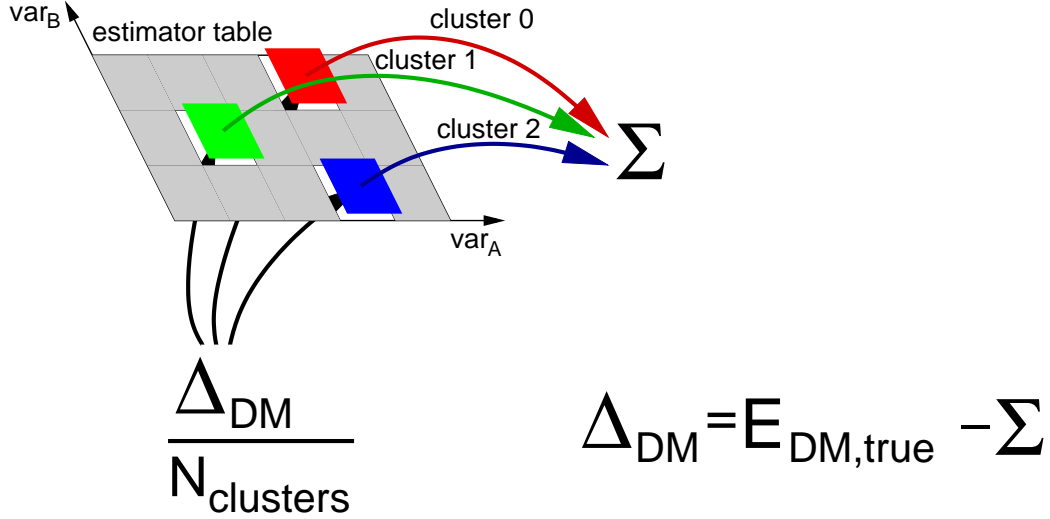


Figure 8.9: Illustration of one step of the iteration to build up the estimator table dependent on two cluster quantities labeled var_A and var_B . For an event with three clusters, the estimators for all cluster are read from the table and summed up (Σ). The difference Δ_{DM} between $E_{DM,true}$ and the sum Σ is calculated and divided by the number of clusters in this event $N_{clusters}$. The table is filled for each cluster with the sum of the old estimator for this cluster and $\Delta_{DM}/N_{clusters}$. The content of each bin is the mean value of all values filled into that bin.

simplified version of the weighting step. The weighting table is replaced by one factor changing the cluster energy to the hadronic scale.

The process is then repeated until the estimated energy converges.

Iterative calculation of the dead material correction

In this section, an iterative approach is shown to relate cluster quantities (e.g. cluster moments, cluster energy deposited in a layer) with the energies deposited in the dead material (*iteration method*).

The basic principle of one iteration step is illustrated in fig. 8.9 and described in listing 8.1. The procedure starts with an empty two dimensional estimator table $f^A(x_0, x_1)$ (all bin contents are set to 0), where x_0 and x_1 are two cluster variables. The procedure can also start with a predefined table with values which are obtained using another DM correction methods. The dead material correction $E_{DM, reco}$ for one event is then

calculated with the formula:

$$E_{\text{DM, reco}} = \sum_{cl}^{N_{\text{clusters}}} f^A(x_{cl}^0, x_{cl}^1) , \quad (8.17)$$

where the variables x_{cl}^0 and x_{cl}^1 are cluster quantities of the cluster cl which define the coordinates (the bin) in the estimator table. The difference $\Delta_{\text{DM}} = E_{\text{true}} - E_{\text{DM, reco}}$ between the true and the reconstructed dead material energy for this event is calculated.

Finally the new correction is divided into N_{clusters} parts and filled into the bins of the estimator table at the positions given by the two cluster quantities x_{cl}^0 and x_{cl}^1 . The new values for the bins of the estimator table are computed with:

$$f^{A, n+1}(x_{cl}^0, x_{cl}^1) = f^{A, n}(x_{cl}^0, x_{cl}^1) + \frac{\Delta_{\text{DM}}/N_{\text{clusters}}}{n+1} , \quad (8.18)$$

where n is the number of times a new value has been added to a particular bin. This step has to be executed for all training events.

Several iterations of this procedure have to be carried out until the estimator table converges to a stable solution. The solution is considered to be stable, when the mean and the RMS of the distribution of true energy deposited in the dead material per event and reconstructed dead material changes by less than $\delta = 0.1$ MeV compared to the previous iteration.

At present, the difference between true and reconstructed dead material energy is equally shared between the clusters. There are other possibilities such as a sharing where the fraction depends on the visibly deposited cluster energy (clusters depositing more visible energy get more DM energy), but no qualitative differences to the equal sharing has been found for the resulting estimator table.

A further possibility is the combination of multiple correction steps as shown in eq. 8.19:

$$E_{\text{DM, reco}} = \sum_{cl}^{clusters} [f^A(x_{cl}^0, x_{cl}^1) + f^B(x_{cl}^2, x_{cl}^3) + \dots + f^N(x_{cl}^n, x_{cl}^m)] . \quad (8.19)$$

First, correction f^A is computed as described earlier until a stable solution is found.

```

for iteration in allIterations:                                # do several iterations
    for event in allEvents:                                     # loop over all events
        eventCorrectionDM = 0

        for cluster in event.clusters:                         # loop over all clusters in the event
            # add correction for this cluster to correctionDM
            # corrections depend cluster-variables varA and varB
            eventCorrectionDM += getCorrection( cluster.varA, cluster.varB )

        # calculate the difference between true DM energy and the correction
        difference = event.trueDM - eventCorrectionDM

        # fill new corrections into the estimator tables
        for cluster in event.clusters: # loop over all clusters
            # get the 'old' correction (same as before)
            oldClusterCorrection = getCorrection( cluster.varA, cluster.varB )

            # new corr. is old corr. plus a fraction of the difference
            fraction = 1.0/event.numberOfClusters
            newClusterCorrection = oldClusterCorrection + fraction*difference

            # finally, fill in the new correction
            fillCorrection( cluster.varA, cluster.varB, newClusterCorrection )

```

Listing 8.1: Pseudo code illustrating the basic principle of the iterative dead material correction method. Within a loop over all events the present dead material correction is computed. This is done by looping over all clusters of the event and retrieving the reconstructed dead material energy for each cluster from the estimator tables. The function `getCorrection(a,b)` looks up in the two-dimensional estimator table in the bin corresponding to the coordinates a and b and gives back the mean of all values which have been filled in before. The variables `cluster.varA` and `cluster.varB` represent two cluster quantities which have been identified to give a good estimation of the energy lost in the dead material. The corrections for all clusters of the event are summed up (`eventCorrectionDM`) and the difference to the true dead material energy of this event is calculated. This deviation of the reconstructed dead material energy from the true value has to be distributed over the clusters in this event. Within another loop over the clusters of the event, Within another loop over the clusters of the event, the DM correction for this cluster is retrieved again (`oldClusterCorrection`). A new DM correction is calculated by summing to the old correction a fraction of the difference.

Then, correction f^A is kept unchanged and correction f^B is calculated with:

$$\sum_{cl}^{clusters} f^B(x_{cl}^2, x_{cl}^3) = E_{DM, reco} - \sum_{cl}^{clusters} f^A(x_{cl}^0, x_{cl}^1) . \quad (8.20)$$

The subsequent corrections f^B, f^C, \dots, f^N are computed in the same manner.

For the additional corrections not only the cluster quantities can be used as coordinates for the estimator tables, but as well the corrections which have been calculated previously. More complex combinations of corrections can be created by making them dependent on a third variable $f^A(x_{cl}^0, x_{cl}^1, x_{cl}^2)$ where multiple estimator tables T_0, \dots, T_n are created for different regions of x_{cl}^2 . An example is the splitting of the estimator table into several ones by the cluster energy. Each table T_n would thus only admit entries, if x_{cl}^2 is within the predefined range for that table.

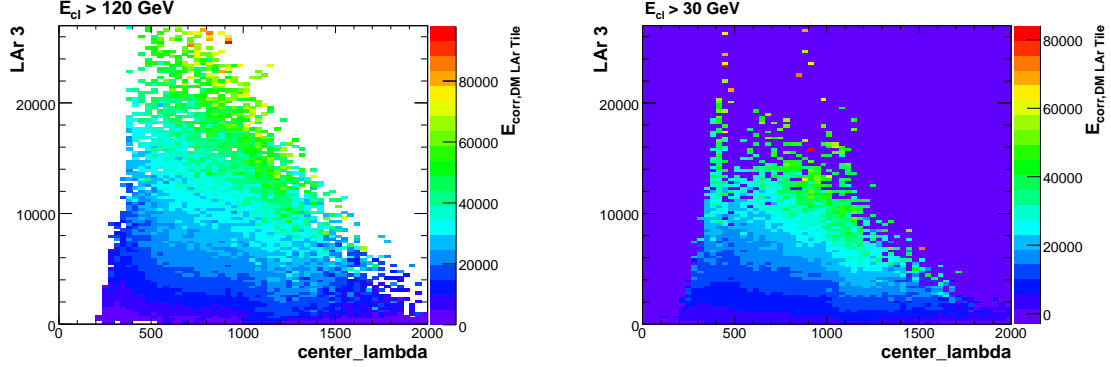
The iterative method has been tested for the dead material region between the LAr and the Tile calorimeter in the Barrel region in the CTB. The dead material region between the LAr and the Tile calorimeter is most important for hadronic showers in the Combined Testbeam 2004. In that region hadronic showers typically deposit a large fraction (on average $\sim 15\%$) of their energy. The reconstruction of this DM energy is therefore crucial for the quality of the hadronic calibration. A set of single particle events (pions and protons) with energies from 10 GeV up to 230 GeV has been simulated to compute the estimator tables. In fig. 8.10 some examples of estimator tables for DM corrections for that region are shown. In fig. 8.10a the estimator table for the dead material energy depending on the cluster variables λ_{center} (barycenter of the cluster) and the energy in LAr3 for all clusters with a reconstructed energy higher than 120 GeV is shown. In fig. 8.10b the same table for reconstructed cluster energies between 30 GeV and 70 GeV are shown. In fig. 8.10c an additional correction as a function of the barycenter of the cluster and the cluster length is shown for cluster energies larger than 120 GeV. The additional corrections although sometimes very large (up to about 1/3 of the first order corrections) have shown to improve linearity and resolution.

Several combinations of the available cluster quantities (energies in layers and cluster moments) have been tested empirically. For the first order correction the barycenter of the cluster and the energy deposited in LAr3 have clearly shown to be the best predictors for the dead material energy. For further orders, no such clear conclusion can be drawn. The energy deposited in Tile A, the cluster length, the η -position of the cluster and the cluster energy itself have shown to improve the result.

8.3 Summary

High-energy particles impinging in the ATLAS detectors create electromagnetic or hadronic showers. The calibration procedure in ATLAS relates the signal produced by the particle showers via ionization or scintillation in the active layers of the calorime-

- (a) Estimator table for $E_{\text{DM,LAr-Tile}}$ for cluster energies larger than 120 GeV as a function of the barycenter of the cluster and the energy deposited in LAr3
- (b) Estimator table for $E_{\text{DM,LAr-Tile}}$ for cluster energies larger than 30 GeV and smaller than 70 GeV as a function of the barycenter of the cluster and the energy deposited in LAr3



- (c) Estimator table for the additional correction $E_{\text{DM,LAr-Tile}}$ for cluster energies larger than 120 GeV as a function of the barycenter of the cluster and m2_lambda (represents the cluster length)

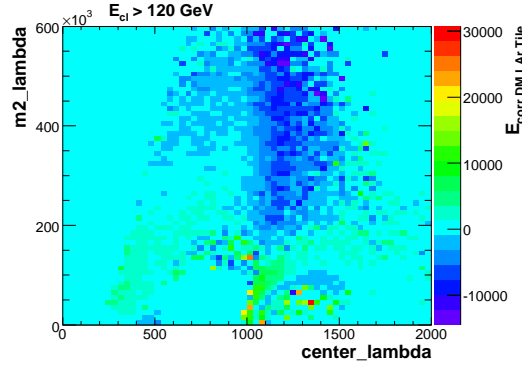


Figure 8.10: (a) and (b) show examples of estimator tables for cluster energies above 120 GeV and between 30 GeV and 70 GeV using `center_lambda` and `eemb3` (energy in LAr3) as coordinates. (c) shows a second order correction for cluster energies above 120 GeV using `center_lambda` and `m2_lambda`.

ters with the true energy of the impinging particle. This is done in several steps. With the calibration of the electromagnetic scale the measured signal of the cells is related to the visibly deposited energy. Subsequently, the hadronic scale is calibrated by grouping the cells to clusters and then relating the visibly in the cells deposited energy to the true cluster energy (known from the CalibrationHits, see sec. 5.6), thus correcting for invisibly deposited energy. Finally, corrections are applied for energy which is deposited outside of the clusters (out-of-cluster energy) and for energy deposited inside inactive material outside the calorimeter cells (dead material energy).

9 Comparison of data to Monte Carlo simulations

In this chapter, the agreement of the MC simulations with data is evaluated by comparing the energy of MC and data after the cells have been grouped by the topological clustering algorithm (see fig. 8.5). The evaluation of MC and data in this chapter is focused on the visibly deposited energy. The aim is to study the influence of dedicated changes in the models for the simulation on the calorimeter response and the shower topology to guide future developments. The best model of the presently used version of the MC simulation framework GEANT4.7 is identified and will be used in ATLAS for the first data taking period. A recommendation is made concerning the models which should be used when ATLAS changes to the version GEANT4.91.

The physics of hadronic showers is very complex and its modeling is under constant development. For some energy ranges there are alternative models such as for the fragmentation models (QGS or Fritiof) or for the intranuclear cascade models (Bertini cascade, Binary cascade). For some models extended versions (e.g. inclusion of diffraction in the QGSP physics lists) exist which treat specific processes with a higher precision (e.g. high precision neutron tracking). For the evaluation of these models different combinations of them have been compiled to physics lists (see sec. 5.5.2). With these physics lists simulations have been produced and compared to the data from the CTB. It will be shown in this chapter, that the differences between these physics lists are often only very small and not of importance for the ATLAS calorimetry. However, some physics lists have shown to provide an improved agreement with data.

In GEANT4 a variety of physics lists are implemented which were compared with data for the CTB. For the comparison of Monte Carlo simulations to data, it is necessary to take the proton contamination of the nominal π^+ beams (see sec. 7.2) into account, because of the differences of shower development for pions and protons (see sec. 4.4 on page 33). For the analysis each distribution has been produced for both types of particles and mixed together according to the fractions estimated for the investigated run.

The ATLAS hadronic calibration scheme has been evaluated in this work with GEANT4.7 QGSP_BERT (see sec. 10). These simulations have been compared to simulations produced with several physics lists with GEANT4.91 and with data. Since the GEANT4.7 version dates from February 2005, in this chapter the newest version is compared to the old one and to data. This might allow to estimate the changes of the new GEANT4 version on the hadronic calibration scheme. The data comparison might direct future work by the GEANT4 team. The MC simulation with GEANT4.7 QGSP_BERT is shown for comparison as a benchmark in all following figures. The physics content represented by the physics lists is explained in sec. 5.5.2.

9.1 Comparison of the energy distribution in the calorimeter layers

Fig. 9.1 shows a comparison of the total energy distribution and the energy distribution in each calorimeter layer of GEANT4.7 QGSP_BERT with GEANT4.91 QGSP_BERT_NQE and GEANT4.91 QGSP_BERT with respect to data. The high peak at low energies corresponding to energies deposited by mips are truncated in the figure to focus on the more important parts of the distributions where the pion already started a hadronic shower. For the sum of the reconstructed energy in all layers, both physics lists GEANT4.91 QGSP_BERT and GEANT4.91 QGSP_BERT_NQE agree well with data. However, near the peak (around 75 GeV) the data shows a dip which is absent in the MC. Several possible origins for this dip have been studied such as an incorrect modeling of the dead material region between the LAr and the Tile calorimeter and the intercalibration of the LAr and the Tile calorimeter, but no conclusive reason has been found. It can be seen that GEANT4.91 QGSP_BERT agrees better with data in this region than GEANT4.7 QGSP_BERT. The comparison of GEANT4.7 QGSP_BERT with the GEANT4.91 QGSP_BERT shows an improvement in the description of the width of the energy distribution. While for GEANT4.7 QGSP_BERT the resolution has been predicted to be too small, GEANT4.91 QGSP_BERT and GEANT4.91 QGSP_BERT_NQE agree better. In particular, the low and the high part of the distribution is much better described.

The main change from GEANT4.7 QGSP_BERT to GEANT4.91 QGSP_BERT is the introduction of *quasi-elastic scattering* which in GEANT4.91 QGSP_BERT_NQE is not used. Hence, differences between GEANT4.91 QGSP_BERT_NQE and GEANT4.91 QGSP_BERT would be due to quasi-elastic scattering. In the analysis of

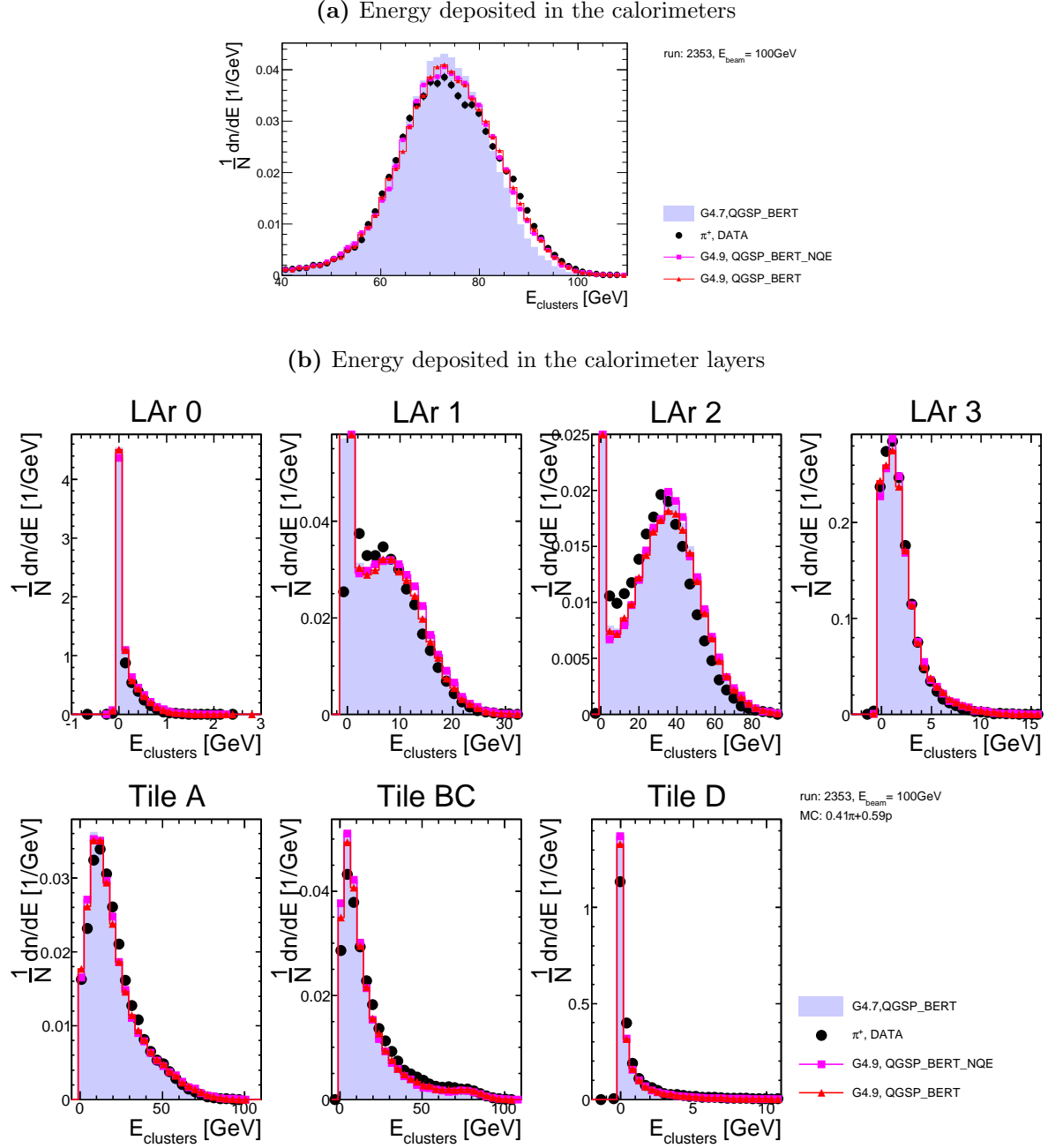


Figure 9.1: Comparison of the total energy distributions in the LAr and Tile calorimeters (a) and in the layers of the LAr calorimeter (0, 1, 2, 3) and of the Tile calorimeter (A, BC, D) (b). Data (black, filled circles) are compared to MC simulations of a mixture of 40% pions and 60% protons simulated with GEANT4.7 with the physicslists QGSP_BERT, and with GEANT4.91 simulated with QGSP_BERT and QGSP_BERT_NQE. The distribution of the sum of the energies deposited in the calorimeters (a) agrees well with data for both GEANT4.91 QGSP_BERT_NQE and GEANT4.91 QGSP_BERT. Data shows a slight dip at 75 GeV which is not seen in the simulations. While there are only slight deviations of both MC from data in the Tile calorimeter, a clear shift of MC to higher energies is visible in the LAr calorimeter. The peak of the distribution of the energy sum is for data 5 to 10% lower than for the simulations.

the TileCal standalone testbeam of 2002 the showers got longer and in better agreement with data. For the CTB the difference can be seen in fig. 9.2 where the ratio between the number of events in MC and in data is shown for Tile BC. Without the quasi-elastic scattering (GEANT4.91 QGSP_BERT_NQE), more events are seen with about 0 GeV and less at large energies. This indicates, that the shower is shorter without quasi-elastic scattering. The difference between GEANT4.7 QGSP_BERT and GEANT4.91 QGSP_BERT_NQE might come from changes in the elastic neutron scattering.

A problematic region is the LAr layer 2 where the simulations predict more events with a larger energy deposit and fewer events with a smaller energy deposit than observed in data. The ratio of the number of events predicted by GEANT4.91 QGSP_BERT divided by the number of events in data as a function of the energy deposited in LAr layer 2 is shown in fig. 9.9a. In events where the particle shower starts in the LAr calorimeter (events which do not pass as a mip through the LAr calorimeter) the energy deposited in the LAr layer 2 is about 10% too high for all three compared physics lists. This means that the shower starts earlier in the MC than in the data. Slight differences in the shape between MCs and data are also visible for LAr 1. The agreement of the shape of data and MC in the Tile calorimeter is good, but in the Tile BC and D layers the simulations predict more events with low energy deposits and correspondingly less events with higher values in the LAr 2 layer. In fig. 9.2 the number of events predicted by the physics lists divided by the number of events measured in data as a function of the energy deposited in Tile BC (sum of all clusters) is shown. For small energies, the simulations predict more events than measured in data. Less events with a larger energy deposit (> 15 GeV) are predicted by the simulations than measured in data. The energy which is deposited in Tile BC by the MC is on the average about 15% too low. For energies in Tile BC above about 75 GeV GEANT4.7 QGSP_BERT predicts drastically fewer events than data, while for GEANT4.91 QGSP_BERT and GEANT4.91 QGSP_BERT_NQE the ratio rises again to above one. These are events where the pion deposits most of its energy in the Tile BC layer and where the interaction is dominantly electromagnetically. This energy region in Tile BC has only a small influence on the response of the calorimeter, since the number of events is much larger for small energies in Tile BC than for high energies (see fig. 9.1b, Tile BC).

The energy deposited by MC in all layers of the LAr calorimeter is on the average about 8% too large while the energy deposited in all layers of the Tile calorimeter is about 8% too small. This indicates that the shower starts and ends too early in the simulations.

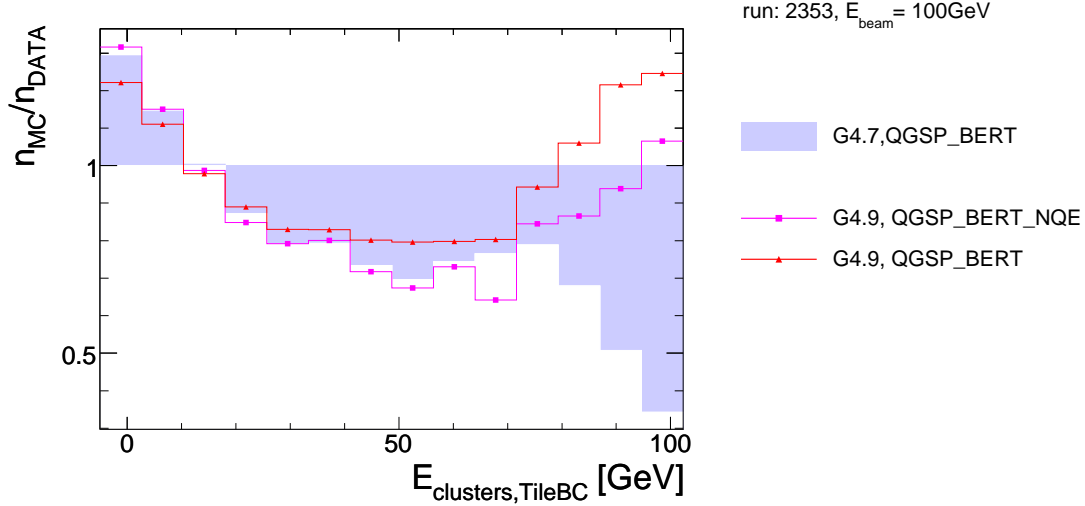


Figure 9.2: The ratio of the number of events predicted by the physics lists divided by the number of events measured in data as a function of the energy deposited in Tile BC (sum of all clusters) is shown. With GEANT4.7 QGSP_BERT about 20% more events have energies below about 10 GeV in Tile BC compared to data. For energies from about 20 to 75 GeV in Tile BC, up to 30% fewer events are produced by GEANT4.7 QGSP_BERT than in data. For energies above about 75% this ratio falls to 70% fewer events. The behaviour of GEANT4.91 QGSP_BERT and QGSP_BERT_NQE is similar up to about 75 GeV. However, it can be clearly seen, that QGSP_BERT_NQE has more events with energies of about 0 GeV, indicating, that the shower gets longer with quasi-elastic scattering. Above 75 GeV, QGSP_BERT_NQE produces up to 10% and GEANT4.91 QGSP_BERT up to 20% more events than data. However, one has to bear in mind, that the absolute number of events decreases considerably towards higher energies.

The main conclusions from the comparisons shown in fig. 9.1 and the ratios in fig. 9.2 are:

- GEANT4.91 QGSP_BERT and GEANT4.91 QGSP_BERT_NQE agree well with data for the total energy distribution, except for a small dip observed in the peak region of the data distribution. The quasi-elastic scattering process makes the shower larger, but not as long as in the data.
- Changing from GEANT4.7 QGSP_BERT to GEANT4.91 QGSP_BERT improves the description of the shape of the total deposited energy.
- The shower starts and ends too early in the simulation. The energy deposited in the LAr calorimeter is about 8% too high and the energy deposited in the Tile calorimeter is about 8% too low.

In fig. 9.3 several flavors of the QGSP_BERT physics lists are compared. The behavior of GEANT4.91 QGSP_BERT, QGSP_BERT_TRV, QGSP_BERT_DIF and QGSP_BERT_HP are similar in all layers except a small peak at about 75 GeV for the QGSP_BERT_HP physics list. The problem that the shower starts and ends too early is not solved by any of the modified physics lists. It can be concluded that the longitudinal shower development is not influenced by the applicability threshold of the Bertini cascade or by the modeling of the low energy neutron physics.

The main conclusion for the comparisons shown in fig. 9.3 is:

- For $E_{\text{beam}} = 100$ GeV all flavors of the QGSP_BERT with GEANT4.91 give very similar results.

In GEANT4 two different intranuclear cascade models *Bertini cascade* and *binary cascade* can be used. In fig. 9.4 the differences of GEANT4.91 QGSP (without cascade model), QGSP_BIC (with binary cascade) and QGSP_BERT (with Bertini cascade) are compared. The agreement of QGSP_BERT with the total energy distribution in the data is good, QGSP_BIC deposits slightly less total energy which makes the description of the data worse. QGSP is clearly shifted to lower energies. In the layers BC and D of the Tile calorimeter QGSP shows a peak at low energies of a much higher amplitude and too few events depositing large energy compared to the data. This indicates that QGSP showers are generally too short. Again all physics lists show the same shift to higher energies in the energy distributions in layer 2 of the LAr calorimeter.

The main conclusions for this comparisons shown in fig. 9.4 are:

- Reasonable agreement of QGSP_BERT and QGSP_BIC with data in terms of total deposited energy. However, the Bertini cascade describes the data better.
- The shift in the LAr 2 layer is independent of the cascade model and is unchanged even if no cascade model is used.
- QGSP produces showers which are too short, using cascade models makes the shower longer in better agreement with the data.

In fig. 9.5 several flavors of the binary cascade are compared. The shapes of the energy distributions for QGSP_BIC, QGSP_BIC_HP and QGS_BIC are very similar to each other for all layers. The shift in LAr 2 to higher energies is present for all flavors of the binary cascade. Compared to QGSP_BIC and QGSP_BIC_HP, QGS_BIC has a more

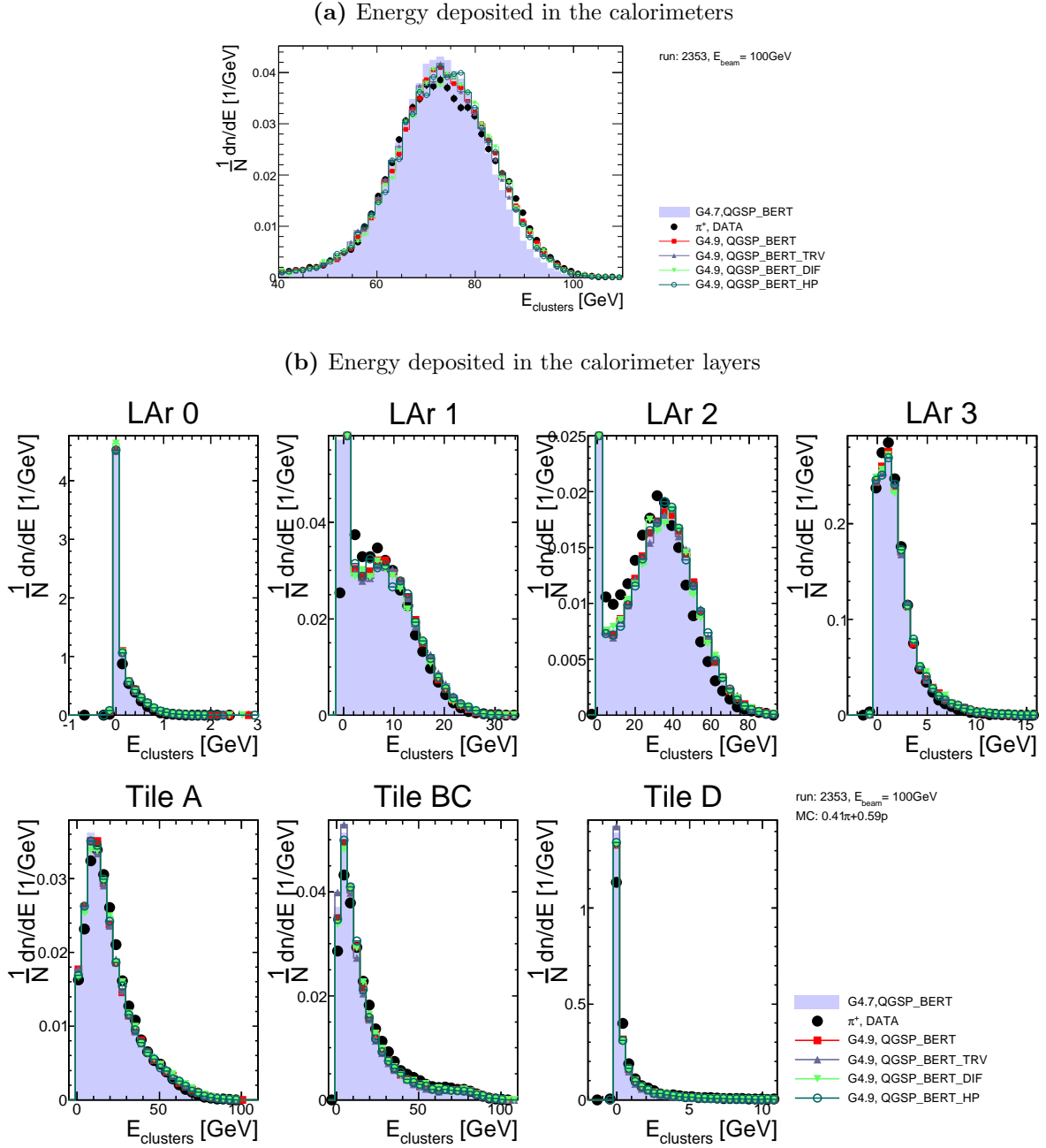


Figure 9.3: Several flavors of the QGSP_BERT model (GEANT4.91) are compared to data and GEANT4.7 QGSP_BERT. No major differences in shape between the different physics lists can be seen in the layer distributions. The shapes of the total energy distributions of the GEANT4.91 physics lists describe the data well. The distribution of GEANT4.7 QGSP_BERT is slightly narrower than data. GEANT4.91 QGSP_BERT, QGSP_BERT_DIF, QGSP_BERT_TRV and QGSP_BERT_HP are very similar. The high precision calculation (HP) produces a small pronounced peak where in data there is a dip (at ~ 75 GeV). In LAr 2 (and to a lesser extend in LAr 1), the distributions of all physics lists are equally shifted to higher energies.

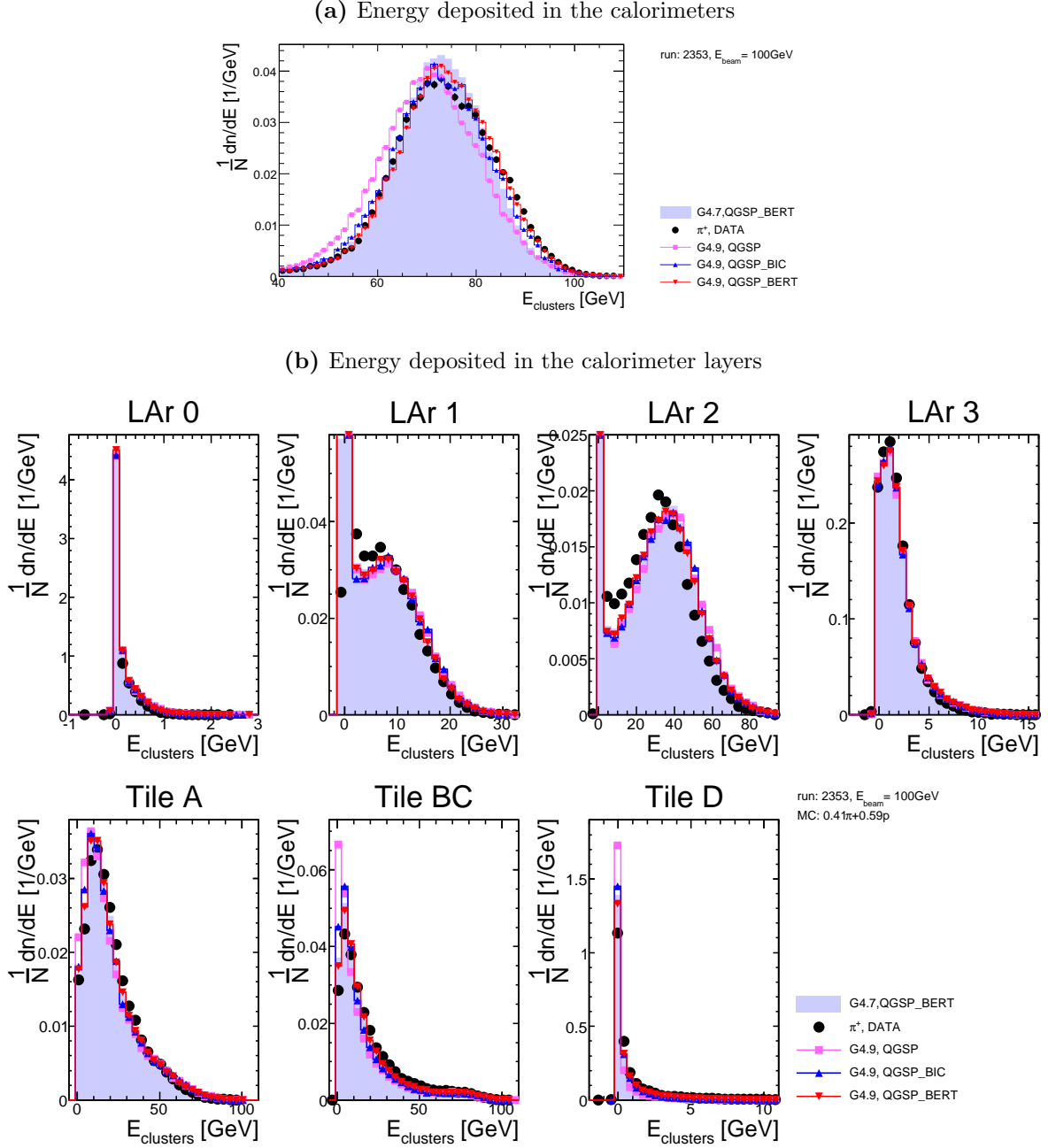


Figure 9.4: Comparison of GEANT4.91 without cascade model (QGSP) with the Bertini cascade (QGSP_BERT) and with the binary cascade (QGSP_BIC) with GEANT4.7 QGSP_BERT and data. The total visibly deposited energy in data is well described by GEANT4.91 QGSP_BIC and GEANT4.91 QGSP_BERT where the first one deposits slightly less energy. GEANT4.91 QGSP predicts less total energy. In the layers all physics lists agree with each other in the LAr calorimeter while in the Tile calorimeter QGSP has a pronounced peak at low energies in Tile BC and D which indicates that QGSP showers are much too short.

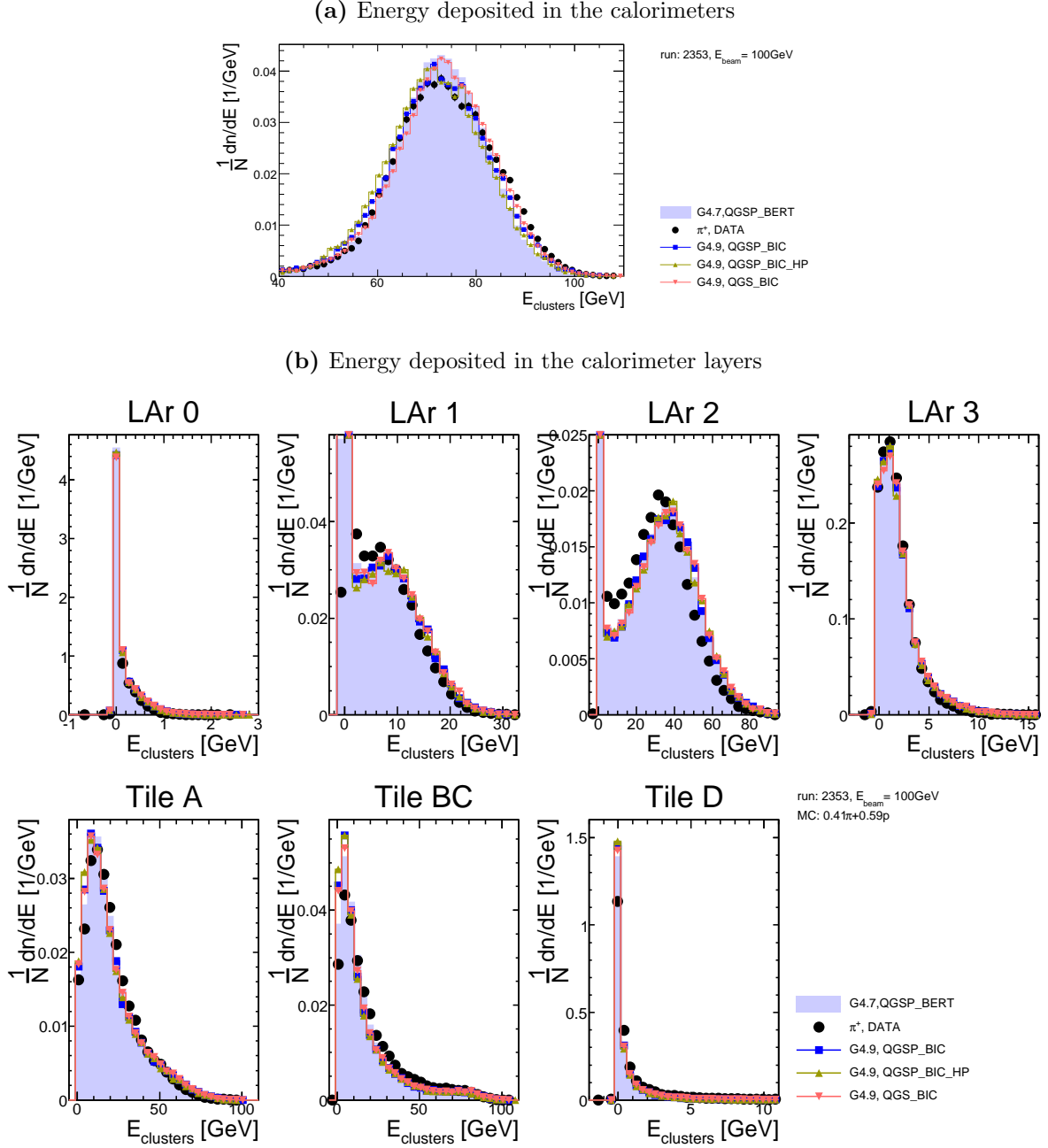


Figure 9.5: Comparison of GEANT4.91 QGSP_BIC, GEANT4.91 QGSP_BIC_HP and GEANT4.91 QGS_BIC with GEANT4.7 QGSP_BERT and data. The behavior of all flavors of the binary cascade is very similar and they describe data generally well. The peak from QGS_BIC is more pronounced than data and the usage of the high precision neutron (QGSP_BIC_HP) model shifts the energy down in worse agreement with the data. The energy deposit in the layers is very similar for all MC. Compared to data, the energy deposits in the LAr calorimeter are too large, while in Tile BC and D they are too low. MC showers are short compared to data.

pronounced peak in the total deposited energy in disagreement with the shape observed in the data.

The main conclusions for this comparisons shown in fig. 9.5 are:

- The shift in the LAr 2 layer does not depend on the modeling of the neutron physics and not on the inclusion of pions in the binary cascade (QGS_BIC).
- Energy depositions are very similar for all models using the binary cascade, using the high precision neutron physics shifts the predicted energy a bit down in worse agreement with data.

In fig. 9.6 several flavors of the Fritiof model are compared. Some clear differences can be observed for layer 2 of the LAr calorimeter. While for QGSP-based models typically a shift to higher energies is observed for MC with respect to data, for the Fritiof models (FTF) the MC describes very well the distribution of data in this layer. In the Tile calorimeter, the peak at lower energies is slightly smaller than in the data while in the high energy regions of the Tile A and BC layers the Fritiof models are slightly above data which indicates that the Fritiof model produces showers which are a bit too long. This is different to the QGSP based models where this behavior is inverse.

In fig. 9.7 the ratio of MC and data as a function of the energy deposited in Tile BC is shown. The ratios for the physics lists without cascade models FTFP and FTFC start too high for very low energies (close to 0 GeV, the first bin), but are then flat until 70 GeV where they start to decrease. FTFP_BERT and FTF_BIC start with a ratio of about 0.8 which increases up to 1.2 at 40 GeV. Then it decreases again to 1 at 80 GeV where it rises again to 1.3 (1.5) for FTFP_BERT (FTF_BIC). This indicates that the Fritiof physics lists without cascade models start slightly too early and the Fritiof physics lists with cascade models start too late.

The total deposited energy is too low for FTFP and to a lesser extent for FTFC. The total energies for FTFP_BERT and FTFP_BIC are shifted to higher values and the width of the distributions for the total energy for the Fritiof models is narrower than in the data. Without the cascade models the total energy is too low. The cascade models make the shower longer than observed in the data.

The main conclusions for the comparisons shown in fig. 9.6 and fig. 9.7 are:

- The Fritiof model predicts a total energy which is lower than in data. Adding the cascade models improves the description independent of the cascade model. With

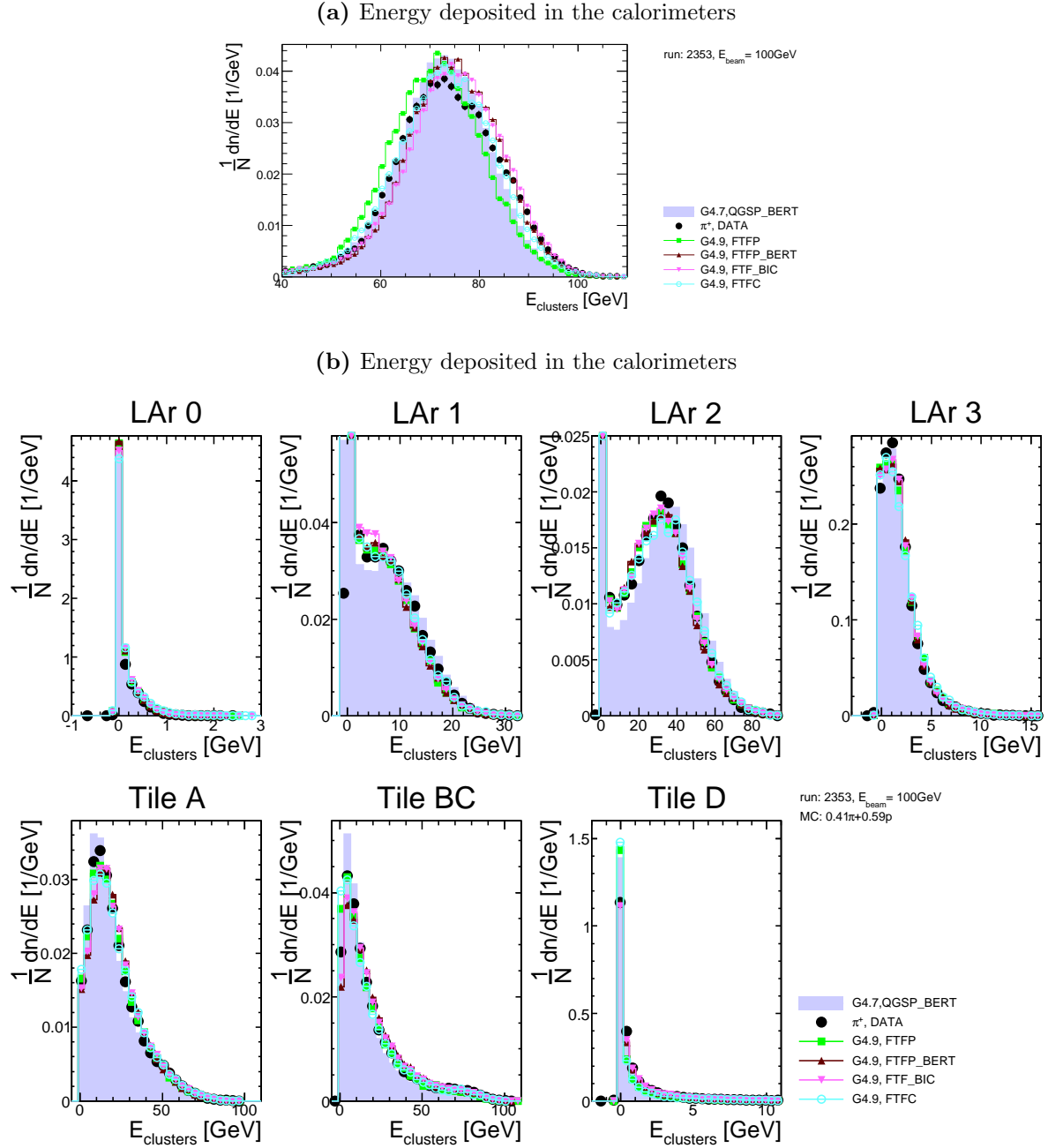


Figure 9.6: Comparison of data and GEANT4.7 QGSP_BERT with several flavors of the Fritiof (FTF) model. The shapes of the energy distribution in the layers are very similar for all flavors of the Fritiof model. In contrast to the QGSP models, all FTF physics lists are able to describe the shape of the distribution of data in layer 2 of the LAr calorimeter much better and also the layer distributions in the TileCal are better described. The total energy is shifted to higher energies for FTFP_BERT and FTFP_BIC, and the width of the distribution is slightly smaller than in data. FTFC agrees with data in the rising slope of the total energy but the falling slope is slightly steeper. FTFP is shifted to lower energies compared to data.

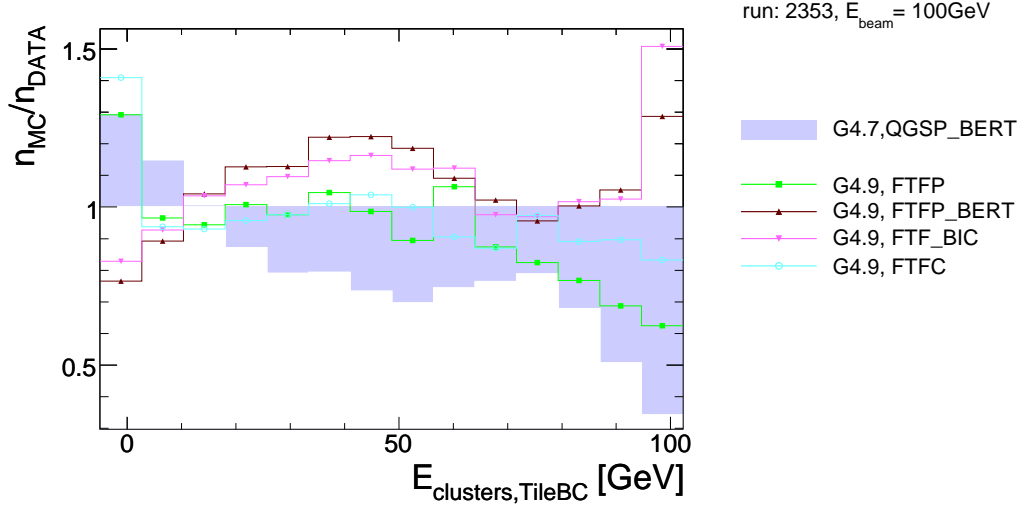


Figure 9.7: The ratio of the number of events predicted by the simulations and the number of events measured in data as a function of the energy deposited in Tile BC (sum of all clusters) is shown for the different variations of Fritiof physics lists. FTFP and FTFC produce too many events where nearly no energy is deposited in Tile BC. Above 5 GeV, the ratio MC to data is about constant up to about 70 GeV where it starts to decrease. The physics lists which use cascade models FTFP_BERT and FTF_BIC predict too few events with small energy deposits in Tile BC. The ratio rises to 1.2 at 40 GeV and then going to 80 GeV decreases to 1. For energies above 80 GeV the ratio increases another time.

cascade models, the total energy predicted by the Fritiof model is larger than in data.

- The longitudinal shower development is well described by the Fritiof model. Adding the cascade models makes the shower a bit longer than in data.

In fig. 9.8 the four main models QGSP, FTFP, QGSP_BERT and FTFP_BERT are compared. To describe the total energy distribution cascade models improve the data description for both fragmentation models (QGS and Fritiof). The total deposited energy agrees best with data for QGSP_BERT, and is shifted slightly to higher energies for FTFP_BERT. The distributions of FTFP and QGSP are both below the data. The LAr 2 energy distribution is best described by FTFP and FTFP_BERT while QGSP and QGSP_BERT are shifted to higher energies. This behaviour can also be seen in fig. 9.9a where the ratio of MC to data is shown for LAr2. While for QGSP and QGSP_BERT the ratio rises from 0.7 at 10 GeV to about 2 at 75 GeV, the ratio for FTFP and FTFP_BERT is about 1 for the whole energy range. This means, that in QGSP and

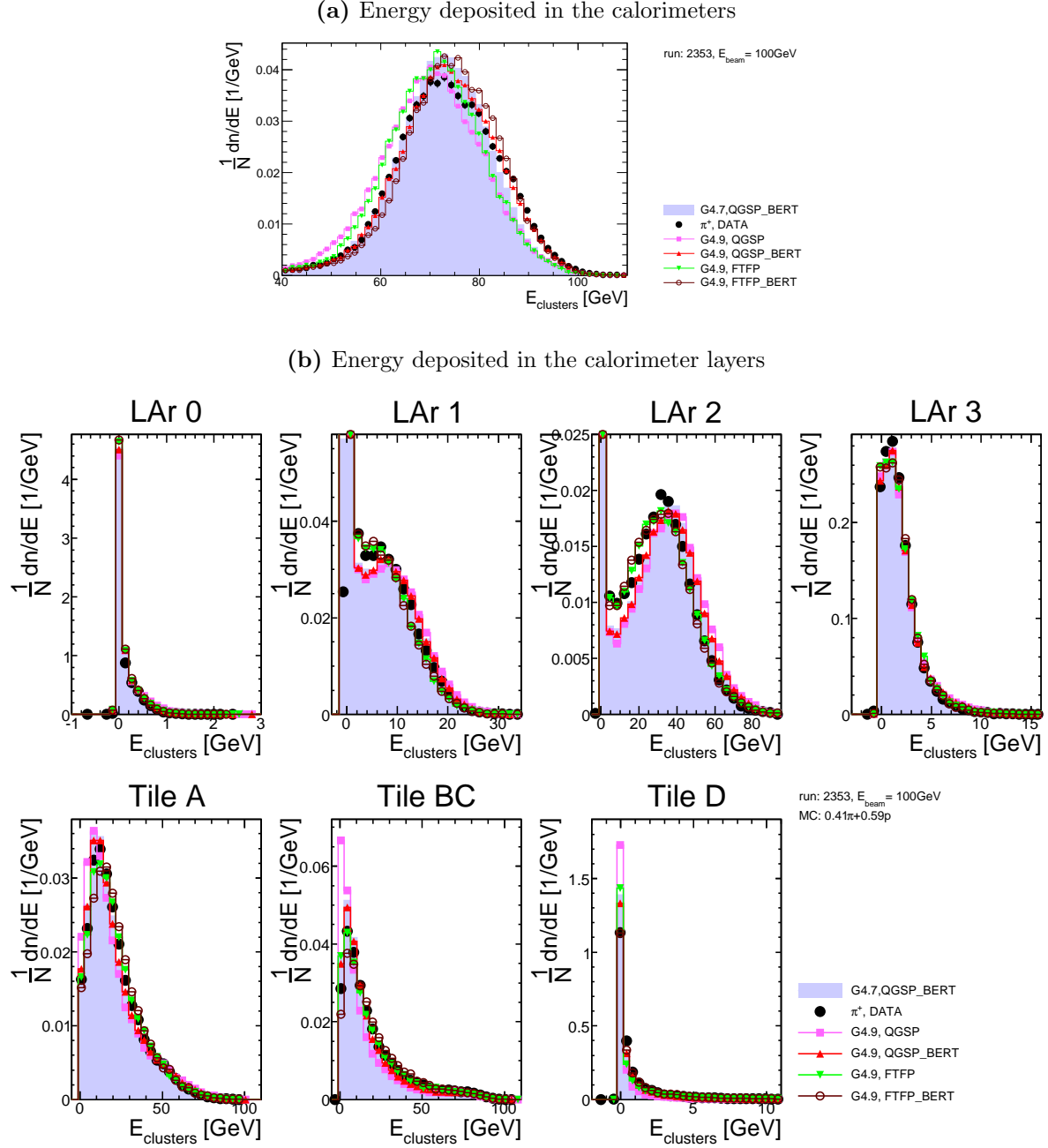


Figure 9.8: Comparison of GEANT4.7 QGSP_BERT with GEANT4.91 QGSP, QGSP_BERT, FTFP, FTFP_BERT and data. Both GEANT4.91 QGSP models give in the layers very similar results with respect to GEANT4.7 QGSP_BERT. In layer 2 of the LAr calorimeter they are shifted to higher energies compared with data, in the Tile calorimeter the QGSP models deposit less energy than data. The Bertini cascade makes the QGSP showers slightly longer and wider, but they still stay short compared to data. A large difference to the QGSP models can be seen for the Fritiof model (FTFP) which for layer 2 of the LAr calorimeter peaks at approximately the same position as data although the peak has a slightly smaller amplitude. The description of the distribution in LAr 1 is as well better described by the FTF models. In the Tile calorimeter the FTFP_BERT predicts slightly more energy than measured in the data. The showers are a bit longer. FTFP shifts the total energy distribution to lower energies.

QGSP_BERT the shower starts too early.

In LAr 1 QGSP and QGSP_BERT stay below data in the low energy region, but are above data for higher energies. FTFP and FTFP_BERT agree with data nicely. In the layers of the Tile calorimeter, QGSP shows a pronounced peak at low energies and stays below data for the trailing slope to high energies. In Tile BC, the low energy peak produced with FTFP_BERT is lower than data, at higher energies FTFP_BERT overestimates the energy depositions, i.e. for this physics list the showers are too long. In fig. 9.9b the ratio of MC divided by data is shown for Tile BC. QGSP produces too many events with low energy deposits in Tile BC, which is a clear indication, that the shower starts and ends too early. The ratio of FTFP is 1.3 for energies below 10 GeV. Above 10 GeV the ratio is about 1 until it decreases to about 0.3 starting from 75 GeV. The ratios of QGSP_BERT and FTFP_BERT show an opposite behaviour. The ratio of QGSP_BERT is too high for low energies and decreasing to a minimum at 50 GeV. This indicates, that the shower starts too early, depositing too much energy in the LAr calorimeter and too few energy in the Tile calorimeter. The ratio for FTFP_BERT is too low for low energies and increasing to a maximum at 40 GeV. This indicates, that the shower starts too late, depositing too few energy in the LAr calorimeter and too much energy in the Tile calorimeter.

The total energy distribution for FTFP is shifted to lower energies by about the same amount as for QGSP (see fig. 9.8a). QGSP_BERT describes the data well and FTFP_BERT is shifted slightly to higher energies. In fig. 9.10 the ratio of MC to data is shown for QGSP, FTFP, QGSP_BERT, FTFP_BERT (all GEANT4.91) and GEANT4.7 QGSP_BERT. Large deviations of the ratio from 1 can be seen for QGSP and FTFP coming from the shift of the total deposited energy to lower energies. The ratio of QGSP_BERT is constant at 1 within 10% indicating a good agreement of QGSP_BERT with data. FTFP_BERT is slightly shifted to higher energies which leads to a minimum at about 55 GeV and a maximum at about 85 GeV. The mean energies of the distributions of the total deposited energies shown in fig. 9.8a are shifted compared to data by -4% for QGSP, -3% for FTFP, 1.1% for FTFP_BERT and no shift for QGSP_BERT.

The conclusions for the comparisons shown in fig. 9.8, 9.9a, 9.10 and 9.9b are:

- The total energy is too low for both QGSP and FTFP. Adding the Bertini cascade increases the responses in better agreement with the data. With the Bertini cascade model, the mean agrees within 1%. The QGSP_BERT simulation is able to reproduce the total energy distribution within 10%.
- The QGSP models produce showers which start and end too early. The energy

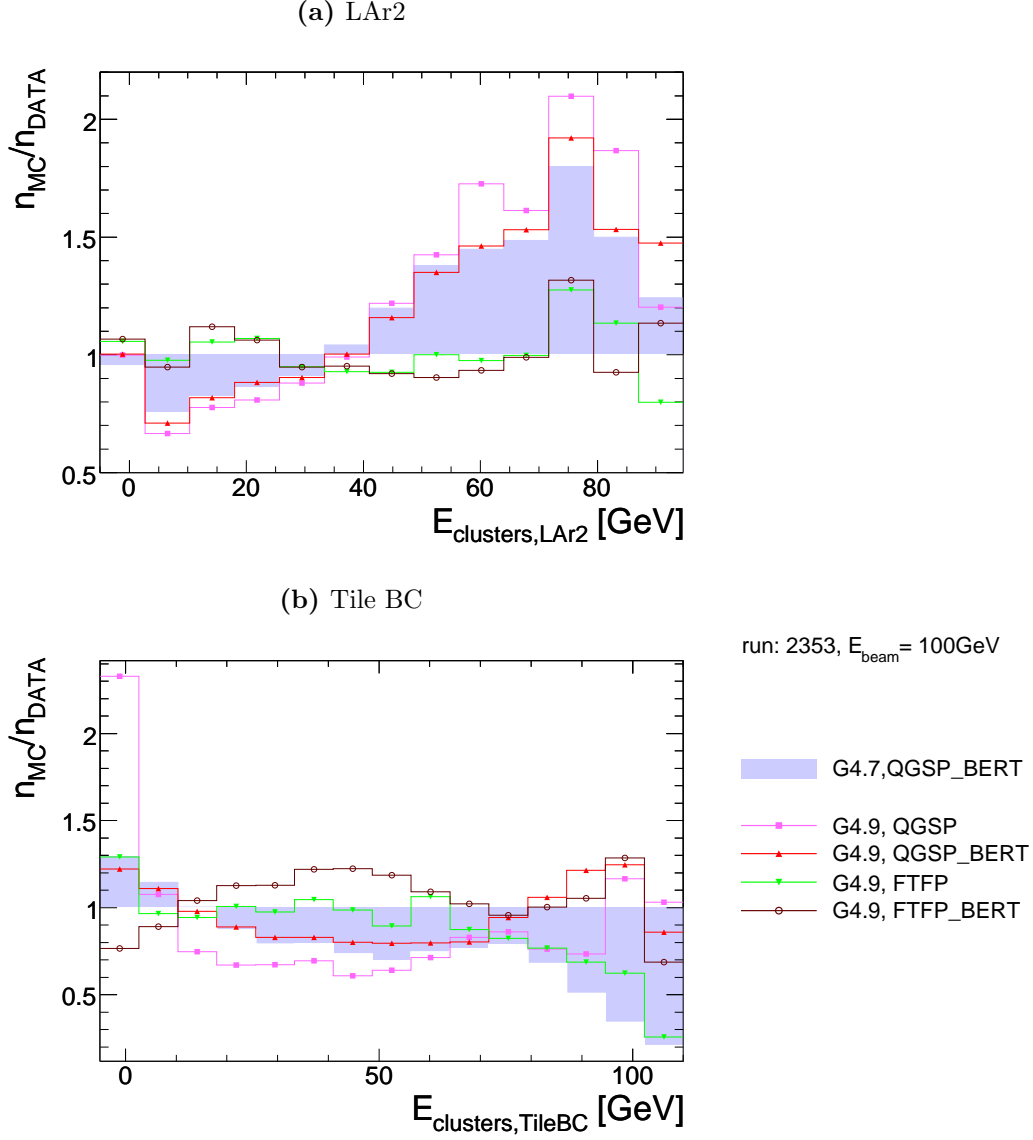


Figure 9.9: The ratio of the number of events predicted by the simulations and the number of events measured in the data as a function of the energy deposited in LAr2 and Tile BC (sum of all clusters) is shown. The ratios in LAr2 are shown in fig. (a). The ratios of the physics lists QGSP (QGSP_BERT) increase from 0.7 at 10 GeV to 2.1 (1.9) at 75 GeV then they decrease to 1.5 (1.2). The physics lists FTFP and FTFP_BERT show a ratio that is about 1 over the whole energy range. In fig. (b) the ratios in Tile BC are shown. The ratio for QGSP is 2.3 for low energies and stays below 1 for energies above 10 GeV except an increase above 90 GeV. The ratio of FTFP is 1.3 for energies below 10 GeV. For energies above 10 GeV the ratio is about 1 until it starts to decrease at about 70 GeV. The ratio for QGSP_BERT starts at 1.2 at low energies and decreases to 0.8 at 50 GeV. Then it rises again to about 1 at 75 GeV. For higher energies the ratio stays between 0.8 and 1.2. The events in that region have only a small influence on the total response of the calorimeter due to their small number. The ratio for FTFP_BERT behaves in the opposite way by starting at 0.8 for low energies and rising to 1.2 at 40 GeV then it decreases to 1 at 75 GeV. For the region above 75 GeV the ratio stays between 0.8 and 1.2.

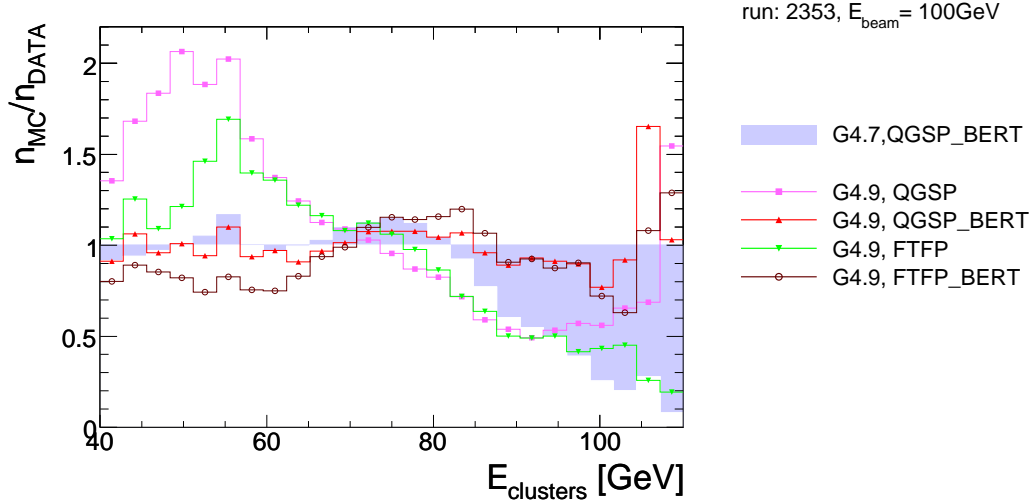


Figure 9.10: The ratio of the number of events predicted by the simulation and the number of events measured in the data as a function of the energy deposited in the calorimeters (sum of all clusters) is shown. As a result from the shift of the distribution to lower energies for QGSP and FTFP, their ratios have a maximum at about 55 GeV and minimum at about 90 GeV. The agreement with data is best for QGSP_BERT for which the ratio is constant at 1 within 10% with larger deviations only in the high energy region (above 90 GeV) which is of minor importance due to the small number of events with energies in that energy region. The ratio for FTFP_BERT is shifted towards higher energies, it has a minimum at about 55 GeV and a small maximum at about 85 GeV which comes from a slight shift of the total deposited energy to higher energies.

distribution in LAr and especially LAr 2 is too high and in Tile too low. Using the Bertini cascade reduces this effect, but not sufficiently.

- FTFP_BERT gives an adequate description of the shower start, but the produced showers deposit too much energy in the Tile calorimeter. Adding the Bertini cascade makes the showers longer than observed in the data.
- The longitudinal shower development is strongly influenced by the fragmentation model.

In conclusion, we have seen that for a pion energy of 100 GeV the QGSP physics list together with the Bertini cascade gives an improved description of the data. The Fritiof fragmentation was able to better describe some of the remaining observables that are difficult to describe for QGSP_BERT. Before concluding on the suitability of the physics lists, we look at a selection of moments and estimators of the clusters and more in detail on the energy sharing between LAr and Tile at 100 and 20 GeV.

9.2 Comparison of the cluster moments and estimators for selected physics lists

Cluster moments and other estimators characterize the topology of the hadron shower. They have been defined in section 8.2.1. In the following the moments of the cluster with the highest energy in the event is chosen to compare data and MC simulations.

In fig. 9.11 the energy fractions deposited in the electromagnetic (LAr) calorimeter (`eng_frac_em`), in the hottest cell (`eng_frac_max`) and in the core of the shower (`eng_frac_core`) are shown for GEANT4.7 QGSP_BERT, GEANT4.91 QGSP, QGSP_BERT, FTFP, FTFP_BERT and data for pions at 100 GeV .

The estimator `eng_frac_max` of the data is well described by the simulations using all physics lists. It denotes the fraction of energy deposited in the cell with the largest signal in relation to the total deposited energy by the cluster.

The estimator `eng_frac_em` varies strongly for all physics lists. It describes the fraction of the energy deposited in the LAr calorimeter in relation to the total deposited energy by the cluster. At low values where more energy is deposited in the Tile calorimeter QGSP and QGSP_BERT both underestimate data although QGSP_BERT is closer to data than QGSP. FTFP slightly overestimates the amount of clusters with that fraction and FTFP_BERT is even above FTFP. For high values for `eng_frac_em` the inverse behavior can be observed. QGSP is clearly too high, which means, that too much energy is deposited in the LAr calorimeter. QGSP_BERT comes closer to data but stays still above. FTFP describes this part of the distribution better than QGSP_BERT and FTFP_BERT gives the best description. The peak at about 1 is underestimated by all physics lists. This peak corresponds to events where the pion shower has been split in two clusters, one in the LAr calorimeter and a second one in the Tile calorimeter.

For the `eng_frac_core` estimator the energy of the cell with the highest signal of each sampling is summed up and divided by the total energy deposited by the cluster. It is showing the amount of energy which is deposited in the core of the shower. QGSP and QGSP_BERT describe well the part up to 0.7, while FTFP and FTFP_BERT are shifted to higher fractions. Showers with large radial extension are therefore not well described by the Fritiof model. In the region above 0.7 the physics lists without cascade models develop a pronounced peak shortly before 1 which is not seen in the data. The peak of QGSP_BERT is marginally shifted to higher fractions in that region and FTFP_BERT

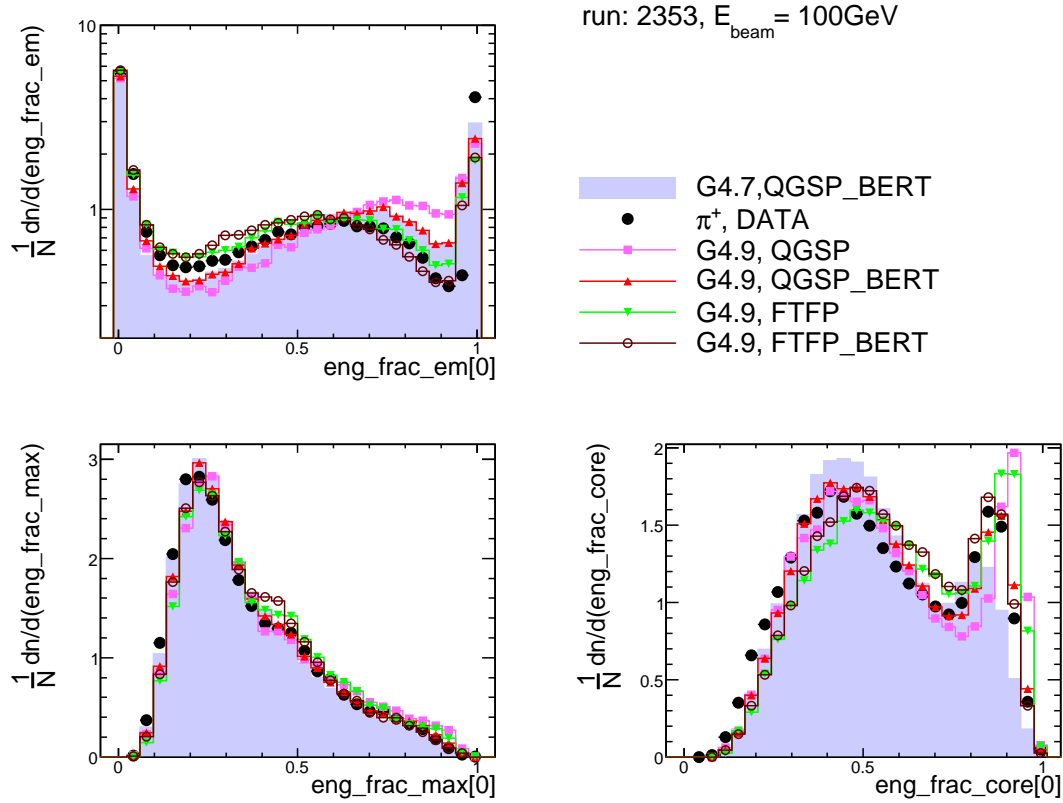


Figure 9.11: Comparison of the moments of the highest energetic cluster describing the fraction of energy deposited in certain regions of the calorimeter. The estimator `eng_frac_em` for the QGSP physics lists has the opposite behavior to the FTFP physics lists. While QGSP is above data for high energy fractions in the LAr calorimeter, it is below data for low fractions. For the FTFP lists, the energy fraction in the LAr calorimeter is lower than for QGSP and closer to data. In clusters where more energy has been deposited in the Tile calorimeter, the QGSP physics lists are below data while the Fritiof lists are above data. The Bertini cascade has for both QGSP and FTFP the same behaviour: More energy deposits are moved from the LAr calorimeter to the Tile calorimeter. For QGSP the agreement is thus better with Bertini cascade, for FTFP without. The estimator `eng_frac_max` is very similar for all physics lists, the agreement with data is good. The estimator `eng_frac_core` agrees well with data for both QGSP lists at the broad peak at low fractions. For the peak at high fractions, QGSP_BERT agrees better than QGSP without the Bertini cascade. The FTFP models are shifted to higher fractions. FTFP_BERT agrees well with data at the narrow peak at large fractions. For both, QGSP and FTFP the Bertini cascade improves the agreement in general, but especially for the narrow peak of the distribution.

describes the peak very well. Adding the cascade models therefore make the shower radially more extended. However, the interpretation of this moment is not so easy, since the cell granularity strongly varies with shower depth.

The shift of the FTF models in the low fraction region can be explained by the tendency to produce longer showers in the FTF models. With longer showers more energy is deposited in the Tile calorimeter contributing to a shift of the core distribution to higher values due to the change in granularity from the LAr to the Tile calorimeter.

The conclusions for the comparison shown in fig. 9.11 are:

- QGSP produces showers which are too short (too much energy in LAr, too few in Tile).
- The Fritiof model is in better agreement to the data, but leads to slightly too much energy in Tile and too few energy in LAr.
- QGSP_BERT produces longer showers than QGSP, but stays still slightly short compared to data. Adding the cascade models makes showers longer in better agreement with data in case of the quark gluon string model and in worse agreement in case of Fritiof.

In fig. 9.12 the lateral and the longitudinal estimators are plotted (see sec. 8.2.1). The physics lists using cascade models describe data generally better than physics lists without. The longitudinal estimator is described best by QGSP_BERT although the peak at 1 is overestimated. Differences between the physics lists can be seen mainly in the region 0.5 to 0.6, where a small peak is produced which is on a different position for QGSP_BERT and FTFP_BERT on one hand and QGSP and FTFP on the other hand. The physics lists with the cascade model is in better agreement with data. In the region of about 0.2 to 0.3 for QGSP and FTFP (physics lists without cascade models) a shallow peak is visible for those physics lists. The peak at about 1 is overestimated by QGSP and QGSP_BERT and underestimated by FTFP and FTFP_BERT.

The conclusions on the lateral and the longitudinal estimators of the clusters shown in fig. 9.12 are:

- The Bertini cascade improves the description of the longitudinal and the lateral estimators.
- FTFP_BERT predicts the data very well.

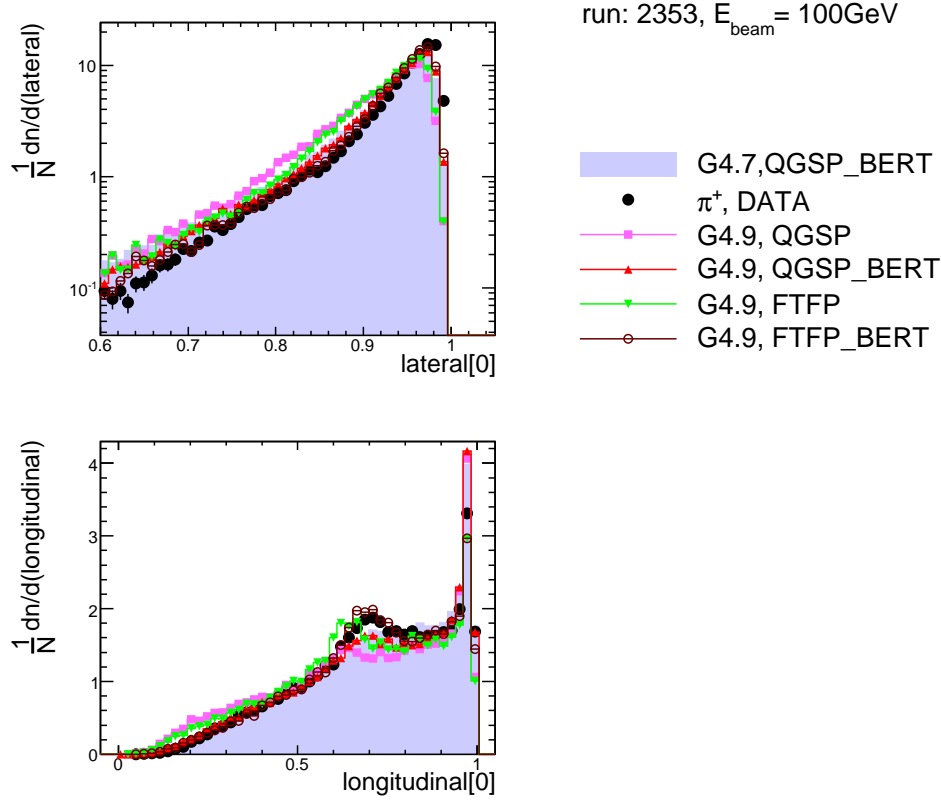


Figure 9.12: Comparison of the lateral and longitudinal estimator distribution for the most energetic cluster for data and MC simulations produced with the physics lists GEANT4.7 QGSP_BERT, GEANT4.91 QGSP, QGSP_BERT, FTFP and FTFP_BERT. The agreement of the MC with the data for the estimator lateral is good for GEANT4.91 QGSP_BERT and GEANT4.91 FTFP_BERT and worse for the physics lists without Bertini cascade model. For the estimator longitudinal the peak just under 1.0 is above data for QGSP and QGSP_BERT and below data for FTFP and FTFP_BERT. At the second (smaller) peak at about 0.65 GEANT4.91 QGSP_BERT and FTFP_BERT agree best with data. FTFP and QGSP are shifted to lower values. QGSP and FTFP develop a small bump at about 0.2.

In fig. 9.13 the first and the second moment of the energy density in the cluster with the highest energy are compared. For both distributions data are well described by the Fritiof physics lists and clearly worse by the QGSP physics lists.

The conclusions on the energy density of the clusters (see fig. 9.13) are:

- The Fritiof physics lists describe the energy density well.
- The QGSP physics lists produce showers with an energy density which is too high.
- The cascade models have no influence.

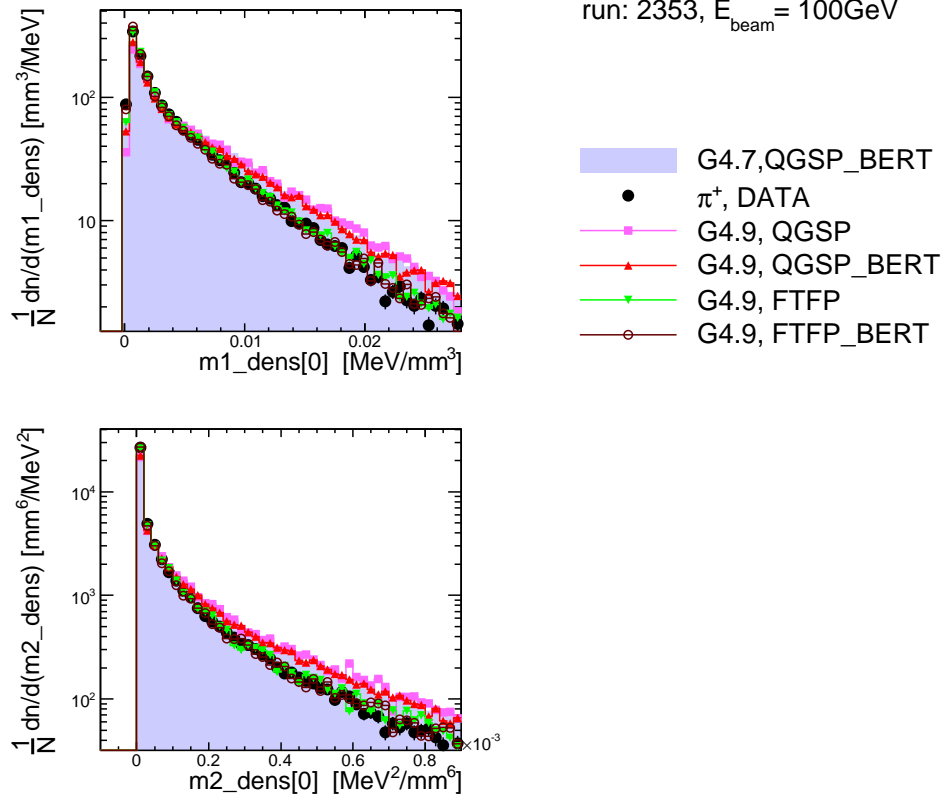


Figure 9.13: Comparison of $m1_dens$ and $m2_dens$ moments of the most energetic cluster of data and the MC simulations with GEANT4.7 QGSP_BERT and GEANT4.91 QGSP, QGSP_BERT, FTFP and FTFP_BERT. For both, $m1_dens$ and $m2_dens$ moments the data is well described by FTFP and FTFP_BERT, QGSP and QGSP_BERT are below data at low values and above at high values.

In fig. 9.14, the moments and estimators $m2_r$, $m2_lambda$ and $center_lambda$ are shown for data and the simulations, GEANT4.7 QGSP_BERT, GEANT4.91 QGSP, QGSP_BERT, FTFP and FTFP_BERT. The moment $m2_r$ is a measure for the radial extension of the shower. A clear difference can be seen for the physics lists using cascade models and those which are not using them. Both, QGSP and FTFP are much too narrow. QGSP_BERT and FTFP_BERT are considerably wider, but are still narrower than the data. FTFP_BERT has slightly higher values for the radial moment than QGSP_BERT, but both do not predict the data which is clearly shifted to higher radial moments. So, the radial extension of the shower is largely influenced by the cascade models and depends only slightly on the fragmentation model. The moment $m2_lambda$ is a measure for the shower length and is generally well described by the physics lists. QGSP is above data for regions below $200 \times 10^3 \text{ mm}^2$, but stays below data for regions

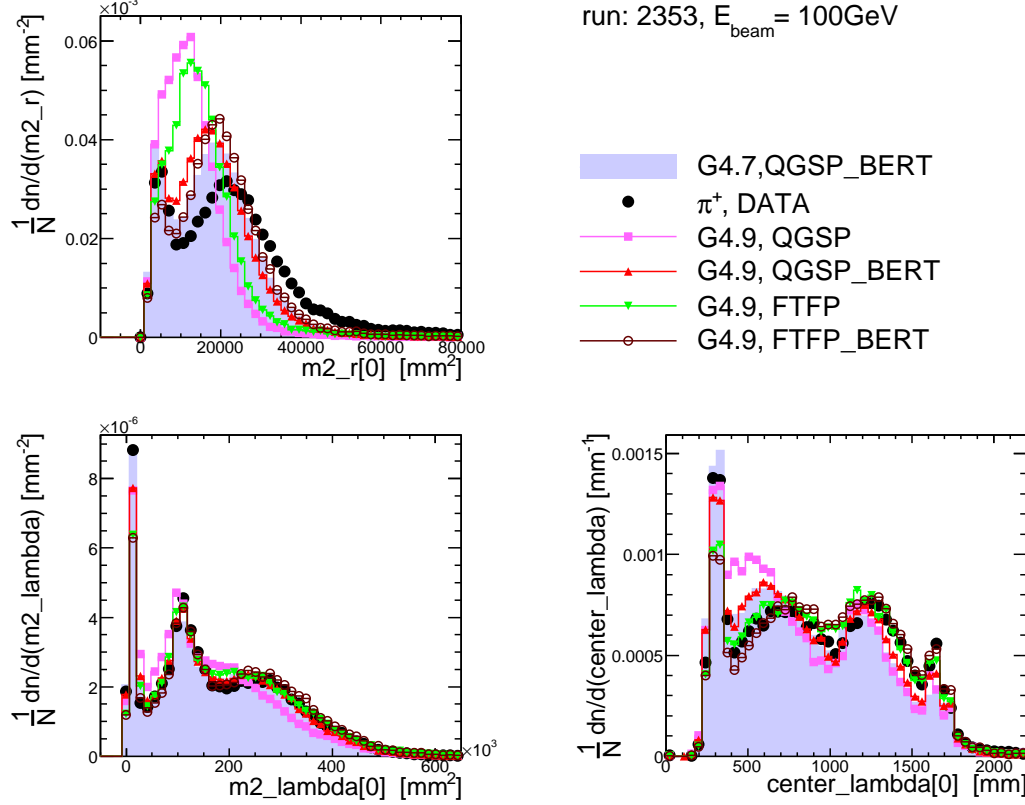


Figure 9.14: Moment distributions $m2_r$, $m2_{\text{lambda}}$ and center_lambda of the most energetic cluster of data and the MC simulations with GEANT4.7 QGSP_BERT and GEANT4.91 QGSP, QGSP_BERT, FTFP and FTFP_BERT. For the $m2_r$ moment QGSP and FTFP are shifted strongly to lower values compared to data. GEANT4.7 QGSP_BERT as well as GEANT4.91 QGSP_BERT and FTFP_BERT are closer to data, but still stay too narrow compared to data. The $m2_{\text{lambda}}$ moment is generally reasonably described by the MC simulations. QGSP predicts values which are too low, FTFP does better, QGSP_BERT is very close to data while FTFP_BERT slightly overestimates the number of clusters with larger values of $m2_{\text{lambda}}$. The center_lambda estimator varies a lot with the different physics lists. For QGSP there is a clear shift to lower values compared to data. The Bertini cascade in QGSP_BERT attenuates this shift. QGSP_BERT agrees for GEANT4.7 and GEANT4.91. FTFP and FTFP_BERT have a better agreement with data although the dip at about 1000 mm is not well described and the peak at about 300 mm is too low.

above that value. This behavior is due to the feature observed earlier that too short showers are produced by QGSP. FTFP shows the same behavior for the region up to $200 \times 10^3 \text{ mm}^2$, but describes data well above that. When adding the cascade models the shower get larger and in better agreement with data. In case of Fritiof the showers get a bit too long.

The estimator `center_lambda` denotes the position of the barycenter of the shower measured from the front face of the calorimeter along the shower axis. Four regions can be identified from left to right (below 400 mm, between 400 and 1000 mm, between 1000 and 1500 mm and between 1500 and 2000 mm). The structure of the distribution of `center_lambda` is caused by the longitudinal structure of the calorimeter system (LAr and Tile calorimeters) and is explained in sec. 9.3. In the first region QGSP and QGSP_BERT have about the same distribution as data, FTFP and FTFP_BERT are below. In the second region, QGSP is clearly above data, QGSP_BERT, FTFP and FTFP_BERT are closer to data. While QGSP_BERT describes better the falling slope, FTFP and FTFP_BERT agree better on the rising slope with data. At about 1000 mm data has a dip which is well described by QGSP and QGSP_BERT. FTFP and especially FTFP_BERT smooth out this dip. The third region is well described by FTFP and FTFP_BERT while QGSP and QGSP_BERT stay below data. In the fourth region QGSP and QGSP_BERT are below data while FTFP and FTFP_BERT follow the data closely. In general with the FTF physics list fewer showers have their barycenter near the front face of the calorimeter, but more at the dip at about 1000 mm, in case of the QGSP physics lists, more showers are at the beginning and less at the end of the calorimeter.

The conclusions from the comparisons in fig. 9.14 are:

- Cascade models (i.e., Bertini cascade, binary cascade) improve the description of the lateral extensions of hadron showers, but the data are still wider than the MC simulations. The lateral shower extension does not depend on the fragmentation model.
- QGSP produces showers which start too early and whose longitudinal extension is too short. Adding the Bertini cascade leads to a better description of the data.
- The Fritiof model leads to larger showers. Adding the Bertini cascade makes the showers larger than the data.
- The QGSP models have the shower barycenter too early. Adding the Bertini cascade improves the data description, but the shower starts still too early. The Fritiof fragmentation model leads to late showers. Adding Bertini makes the showers too long.

9.3 Energy sharing between the LAr and Tile calorimeters

To get a better idea about the topology of the events in the four regions of the `center_lambda` estimator (barycenter of the cluster λ_{center}) identified in fig. 9.14 the reconstructed energy in the LAr calorimeter, the Tile calorimeter and both calorimeters are plotted for those four regions in fig. 9.15.

In first region of λ_{center} from 0 to 400 mm nearly all of the shower energy is deposited in the LAr calorimeter. These showers deposit a large fraction of their energy in the first 1.8λ of the calorimeter. It is likely, that such events loose a lot of energy in the dead material behind the LAr calorimeter. The shape of the distribution of the data is very well described by the physics lists FTFP and FTFP_BERT. QGSP and QGSP_BERT deposit too much energy and are therefore shifted to higher energies.

In the region of λ_{center} between 400 mm and 1000 mm the energy is deposited in the LAr and the Tile calorimeter with the larger amount of energy in the LAr calorimeter. In the LAr calorimeter the data are well described by FTFP and FTFP_BERT, while QGSP and QGSP_BERT are shifted to higher energies. In the Tile calorimeter the data are best described by GEANT4.7 QGSP_BERT, GEANT4.91 QGSP_BERT and FTFP. QGSP deposits too few energy and FTFP_BERT is slightly shifted to higher energies. The sum of LAr and Tile calorimeter is described by QGSP_BERT (GEANT4.7 and GEANT4.91) and slightly worse by FTFP_BERT. QGSP and FTFP are shifted to lower energies.

In the region of λ_{center} between 1000 mm and 1500 mm a small amount of energy is deposited in the LAr calorimeter and a large amount in the Tile calorimeter. The shape of the energy distribution in the Tile calorimeter has two peaks. The first peak at about 50 GeV consists of the events which deposit a considerable part of their energy in the LAr calorimeter. These events probably loose a lot of energy in the dead material between the LAr and the Tile calorimeter. The second peak at about 80 GeV is formed by events which deposit basically all of their energy in the Tile calorimeter. When the sum of the energy in the LAr and the Tile calorimeter is considered, a broad distribution with one peak is observed. Events with less energy in the Tile calorimeter are thus complemented by energy deposits in the LAr calorimeter. The peak at lower energy in the Tile calorimeter is best described by GEANT4.7 QGSP_BERT and GEANT4.91 QGSP_BERT. FTFP_BERT is slightly above the data, but the position of the peak agrees with the

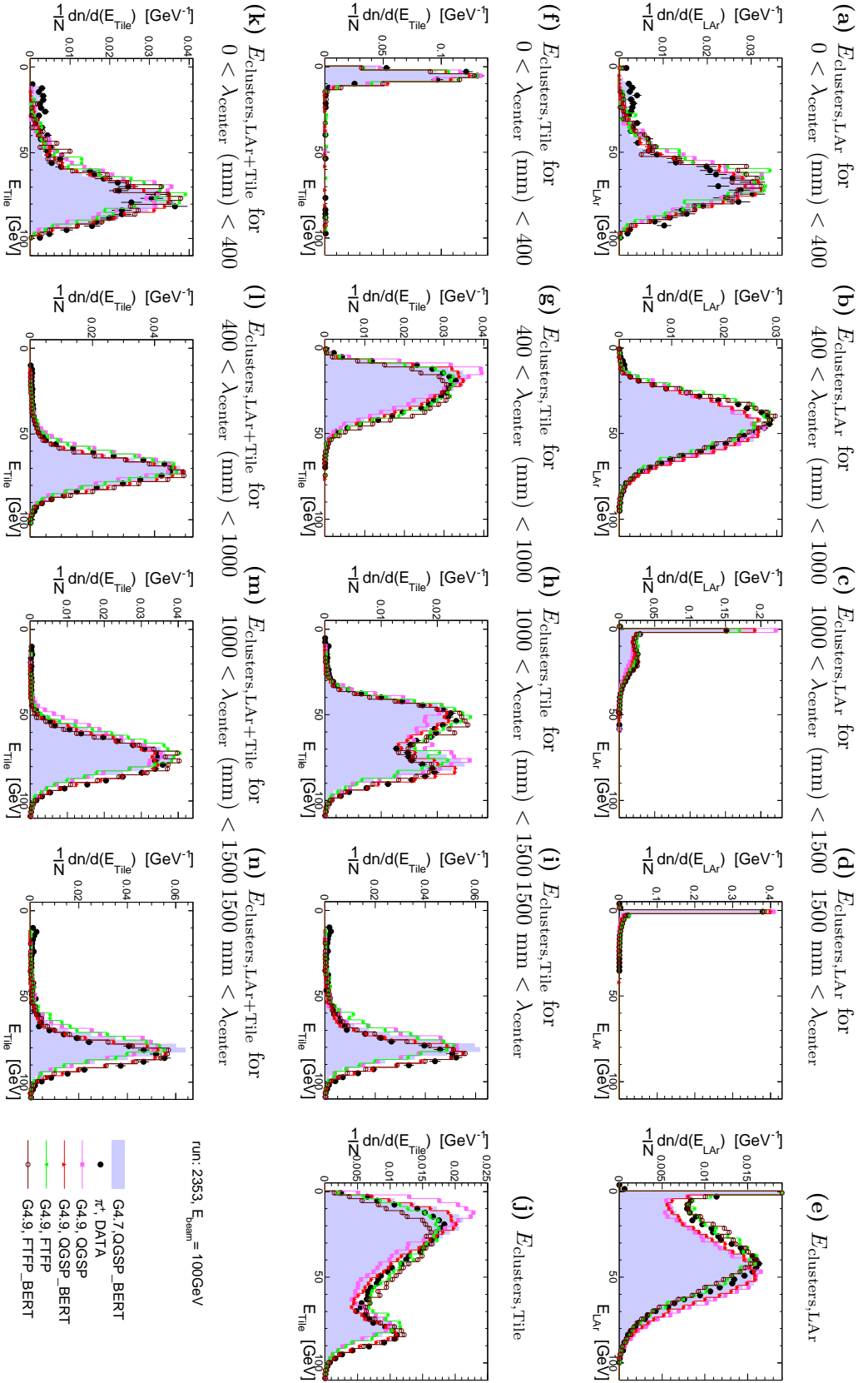


Figure 9.15: Energy sharing between the LAr and the Tile calorimeter for the sum of the energy of all clusters of each event for different regions of the barycenter of the clusters λ_{center} . The uppermost row shows the reconstructed energy in the LAr calorimeter, the middle row for the Tile calorimeter and the bottom row for the sum of both. In the columns, different groups of events are presented depending on the energy-weighted barycenter of all clusters of the event (calculated with: $\lambda_{\text{center}} = \sum_d^{clusters} (\lambda_{\text{center},d} E_{cl}) / \sum_{cl}^{clusters} E_{cl}$). The distribution of λ_{center} is shown in fig. 9.14. In the fifth column, the reconstructed energy in the LAr and Tile calorimeter are shown for all events.

data. QGSP underestimates the number of events depositing energy in the LAr and the Tile calorimeter in favor of events where the energy is deposited basically only in the Tile calorimeter (peak at higher energies). In this region it overestimates the number of events and deposits too much energy (pronounced peak of QGSP at about 80 GeV). QGSP and FTFP deposit both too few energy in the Tile calorimeter at the events with showers only in the Tile calorimeter. The peaks are shifted to lower energies compared to data. The peak of the events showering only in Tile is well described by QGSP_BERT and FTFP_BERT. For the sum of LAr and Tile QGSP_BERT and FTFP_BERT describe the energy deposits of data better while QGSP and FTFP show a shift to lower energies.

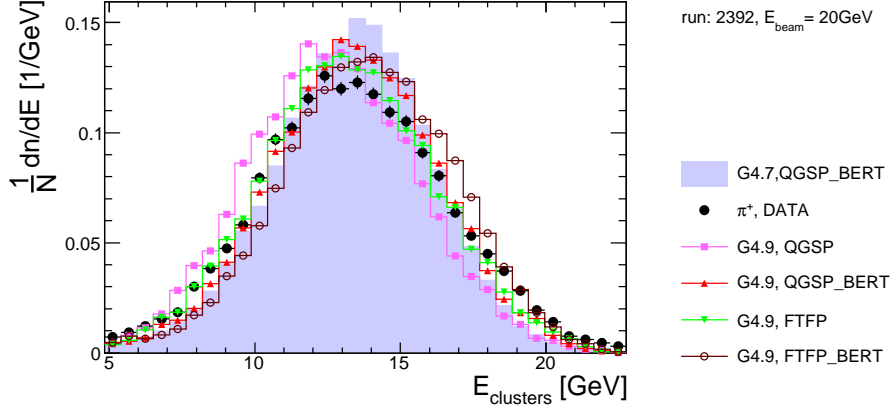
In the region of λ_{center} larger than 1500 mm basically the same features can be seen as for the region between 1000 mm and 1500 mm for the events which deposited most of their energy in the Tile calorimeter. Data is best described by QGSP_BERT and FTFP_BERT and QGSP and FTFP are clearly shifted to lower energies. The sum of LAr and Tile has the same shape as the Tile calorimeter distribution as only a negligible amount of energy is deposited in the LAr calorimeter.

Fig. 9.15e and 9.15j show the energy distributions of data and the compared physics lists for all events (no cut in λ_{center}). The same features as discussed for the selected regions earlier are seen again for the distribution of all events in LAr and Tile. The distribution of the sum of the energy in LAr and Tile for all events is shown in fig. 9.8a.

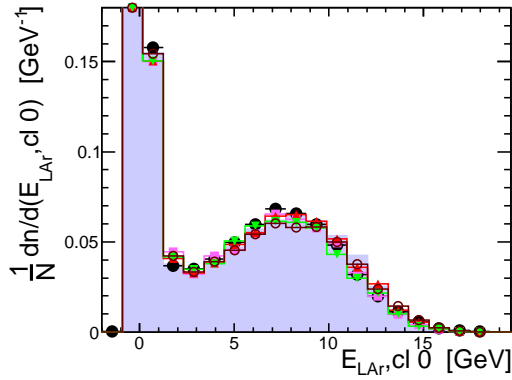
The conclusions from these Monte Carlo comparisons (see fig. 9.15) are:

- The QGSP models (with and without cascade model) deposit too much energy in the LAr calorimeter. The amount of energy deposited in the Tile calorimeter agrees with the data when the Bertini cascade is added.
- The FTFP models (with and without cascade model) describe the energy deposit in the LAr calorimeter very well. For events where some energy is deposited in the LAr calorimeter, the amount of energy deposited in the Tile calorimeter is too high. The total energy is well described for events where the most energetic cluster is only in Tile and shifted to higher energies for event where the dead material region between the LAr and the Tile calorimeter is crossed by the shower.

(a) Energy of the most energetic cluster deposited in the calorimeters



(b) Energy of the most energetic cluster deposited in the LAr calorimeter



(c) Energy of the most energetic cluster deposited in the Tile calorimeter.

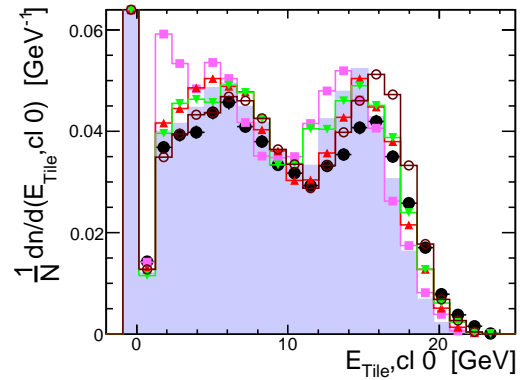


Figure 9.16: (a) shows the sum of the energy deposited in LAr and Tile. Data is best described by QGSP_BERT. The distribution of the total energy with QGSP is shifted to lower energies. FTFP agrees generally well with data, at high energies it is slightly below data. QGSP_BERT describes data well, but it is in the peak region above the data. FTFP_BERT is shifted to higher energies. (b) shows the energy of the most energetic cluster deposited in the LAr calorimeter. The energy distribution in the LAr calorimeter is very similar for all physics lists. (c) shows the energy deposited in the Tile calorimeter. In the high energy region (above 12 GeV), QGSP_BERT predicts data the best while FTFP_BERT produces too many events and QGSP and FTFP are shifted to lower energies. Below that region, FTFP_BERT agrees best with data, QGSP_BERT produces slightly too many events, FTFP is close to data, but QGSP is clearly off.

9.4 Energy sharing and selected moments for 20 GeV pions

In fig. 9.16 the energy deposited in LAr and Tile by the most energetic cluster for pions with an energy of 20 GeV is shown. In both, the LAr and the Tile calorimeter QGSP and FTFP describe data the worst. QGSP_BERT describes the data best in the high energy region and FTFP_BERT in the low energy region. FTFP_BERT is slightly shifted to lower energies in the LAr calorimeter. For the sum of LAr and Tile calorimeter QGSP_BERT and FTFP agree best with data. QGSP is shifted to lower energies, FTFP_BERT is shifted to higher energies.

The conclusions from these Monte Carlo simulations are:

- QGSP does not describe data well: the total response is too low, the showers start and end too early. Adding the Bertini cascade improves the data description.
- The Fritiof model describes the energy distribution well. Adding the Bertini cascade leads to a response that is too high and to a shower that is too long.

In fig. 9.17 the radial extension (`m2_r`), the longitudinal extension (`m2_lambda`) and the barycenter (`center_lambda`) of the most energetic cluster of all events are shown. The radial extension is much too small for the physics lists without cascade models. QGSP_BERT and FTFP_BERT show a very similar behavior and come closer to the data, but are still too narrow. For the second moment in λ and for the barycenter of the cluster all physics lists are very similar. QGSP produces slightly shorter showers and its barycenters are too early.

The conclusions of these Monte Carlo simulations are:

- Physics lists without cascade model predict clusters which are much too narrow. Using the Bertini cascade improves the radial extension of the clusters, but the extension of the data is not reached.
- QGSP produces showers which start too early and are slightly too short.

9.5 Summary

No physics list is capable of describing data in all layers, for all cluster moments and the total deposited energy. On the other hand, for each studied observable (except the radial extension) there is at least one physics list that approximately describes the data.

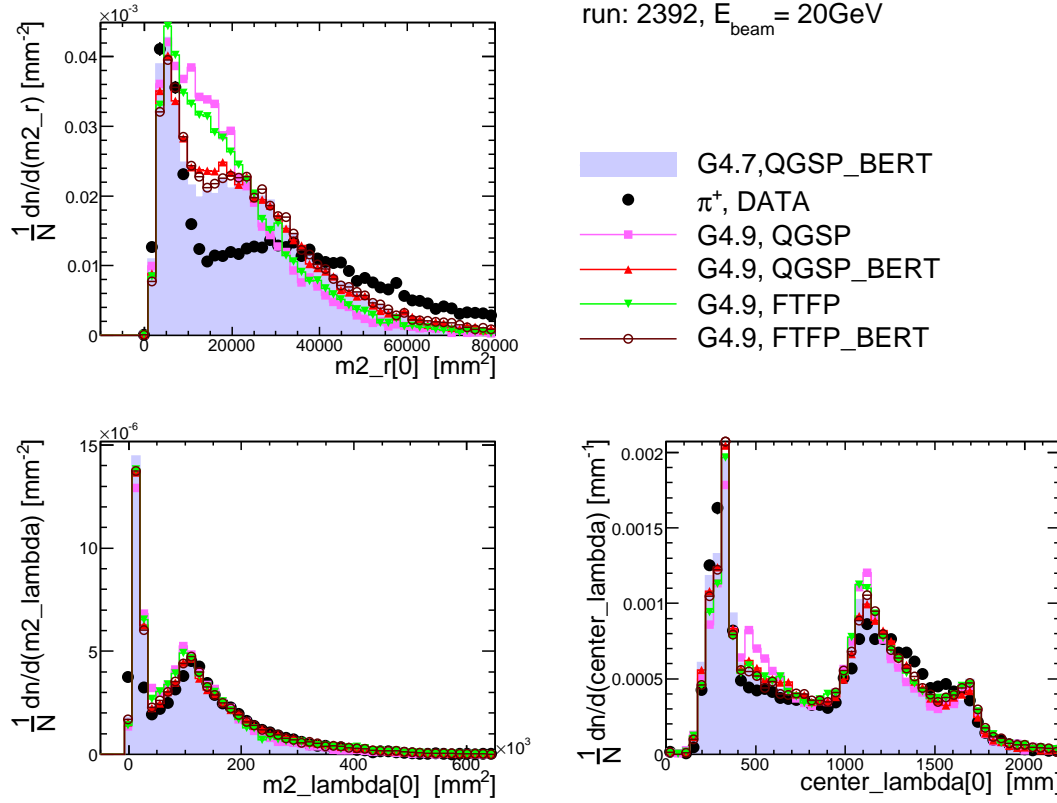


Figure 9.17: Comparison of data and MC simulations at 20 GeV with GEANT4.7 QGSP_BERT and GEANT4.91 QGSP, QGSP_BERT, FTFP and FTFP_BERT for the radial moment, the longitudinal extension and the barycenter of the highest energetic cluster. The physics lists QGSP and FTFP without Bertini cascade show a very different behavior for the moment $m2_r$ than data. Both physics lists produce distributions which are much too narrow. The use of the Bertini model in QGSP_BERT and FTFP_BERT improves the radial extension of the cluster, but the clusters are still too narrow compared to data. The longitudinal extension $m2_lambda$ is very similar for all physics lists. QGSP and FTFP are slightly shorter, but data is generally well described. The barycenter of the cluster $center_lambda$ is best described by FTFP_BERT and QGSP_BERT which are very similar one to each other. QGSP has the barycenter of its clusters too early.

In the ATLAS weighting scheme the cluster moments characterizing the shower topology have an important role (e.g., classification of a shower (a cluster) as electromagnetic or hadronic, weighting, dead material corrections). It is thus not sufficient to choose simply the physics list which describes the total deposited energy best. This brief summary gives a quick look on the most important features of the tested physics lists and a recommendation on which to use for ATLAS.

The physics list which is used to validate the weighting techniques is GEANT4.7 QGSP_BERT. The important changes from the GEANT4.7 to GEANT4.91 version of QGSP_BERT are the introduction of the quasi-elastic scattering for hadrons and an improvement in the description of elastic scattering and a change of the sampling fractions due to the introduction of a new multiple scattering model. These differences lead to an improvement in the description of the total deposited energy. The better description of the width of the shape of the total energy distribution gives a better description of the energy resolution of data by the simulations.

- The longitudinal shower development is largely influenced by the fragmentation model. The Fritiof model is in better agreement with the data than the quark gluon string model. The quark gluon string model starts and ends too early.
- Adding the cascade models make the shower longer, in better agreement with the data in case of the quark gluon model, but worse for the Fritiof model.
- Adding the cascade models also increases the total response and brings the simulations in better agreement with the data. The use of the Bertini or binary cascade leads to similar longitudinal shower developments. The response is a bit lower for the binary cascade.
- The radial extension of the shower is largely influenced by the cascade models and does not depend on the fragmentation model. Adding the cascade models make the showers radially wider. However, the data are still wider than the data.
- High precision neutron physics does not significantly improve the data description.
- The energy cell density is strongly influenced by the fragmentation model. It is best described by the Fritiof model. Cascade models do not influence the energy density.
- No difference has been found between the precompound and the chiral invariant phase space (CHIPS) models.

In conclusion, there is no physics list that describes all the features of the data. The best overall description of the data is obtained with the Fritiof model with or without the Bertini cascade and with the quark gluon string model with the Bertini cascade.

For the analysis of the first data, ATLAS has now adopted QGSP_BERT as the default physics list. This decision has been taken based on the results of the MC/data comparison studies presented in this thesis. Further recommendations for ATLAS are to change

from GEANT4.7 to GEANT4.91 with QGSP_BERT as the main physics list and with FTF_BIC as second physics list. The complementary description of the longitudinal shower development might be useful to evaluate the systematic uncertainty in certain measurements.

In the following, the GEANT4.7 version is used to validate the pion calibration scheme¹. From the comparison above, the new version is expected to behave similarly. Only in the description of the width of the total energy distribution and therefore the resolution an improvement is expected.

¹This has purely practical reasons, since only for the old version a large data set necessary for the validation was available.

10 Hadronic energy measurement with the ATLAS baseline method

In the previous chapter the MC simulations have been compared to data for observables like the total energy, the energies in the layers or other observables characterizing the shower topology. It has been shown that the physics list QGSP_BERT describes the data best.

The default ATLAS hadronic calibration scheme developed for the ATLAS detector is based on MC simulations. All the corrections are extracted with respect to the true energy deposits. The quality of the calibration depends critically on the ability of the MC to describe the data.

In this chapter the ability of the MC simulations using the QGSP_BERT physics to predict the corrections necessary to reconstruct the full pion energy will be tested. Corrections will be derived from the MC simulations and applied on data. Before ATLAS is starting to take data, the only data available are from testbeams which have been undertaken in the past. For the validation of the calibration scheme and to assess its quality the ATLAS Barrel Combined Testbeam 2004 (CTB) has been chosen where all sub-detectors present in a slice of the ATLAS detector have been tested. The calibration scheme consists of three steps: weighting, out-of-cluster corrections and dead material corrections.

10.1 Technical details

In the following sections each correction (i.e. weighting, out-of-cluster, dead material) has been derived from MC simulations of charged pions (and for protons) at various energies and then applied to data. For each energy 15000 events for pions and the same number of events for protons have been used for various pion and proton energies which sums up to 780000 events in total. While for the weighting of the full ATLAS detector a logarithmic scale from very low energies (150 MeV) up to the TeV-scale

energies (GeV)	run-number (geometry)
15, 17, 20, 22, 25	2392
35, 40, 45, 50, 55, 60, 65	2343
70, 80, 90, 100, 110, 120, 130	2355
130, 150, 170, 180, 190, 210, 230	2225

Table 10.1: Energies and run-numbers of the simulations used to derive weights and corrections. The first column shows the energies which have been simulated and in the second column the run-number (geometry) which has been used for the simulation is shown.

is used, in the CTB the energies shown in tab. 10.1 have been simulated with the geometries from the four runs from data which have been chosen as a reference. An energy range of about $\pm 30\%$ around the energy of the corresponding data runs has been simulated. This is necessary to avoid to assume the beam energy when evaluating the corrections. All simulations have been done with Athena, version 12.0.6 and GEANT4, version 4.7 using QGSP_BERT as physics list for the simulation of the hadronic physic. Several technical differences between ATLAS and the CTB setup made adaptations of the software necessary.

10.2 Weighting correction

The weighting to correct for invisible energy losses is done as described in sec. 8.2.2. The aim of the weighting step is to obtain the total true deposited energy in each cluster. This is done by multiplying the energy of each cell of a cluster with a weight which depends on the cluster energy and the energy density of the cell. The lookup table with the weights has already been shown in fig. 8.7. Fig. 10.1 shows the difference between the sum of the reconstructed energy (blue circles) and the true deposited energy (red squares) in all clusters for a simulations of pions with a beam energy of 100 GeV. Before the weighting, the mean value of the reconstructed energy is on average about 12 GeV lower than the true energy. Afterwards, the reconstructed energy is approximately equal to the true energy and the RMS improves from 5.31 GeV to 5.17 GeV.

Figs. 10.2(a) and (b) show the effect of the weighting for simulated pions with 20, 50, 100 and 180 GeV beam energy. A good agreement of reconstructed and true energy

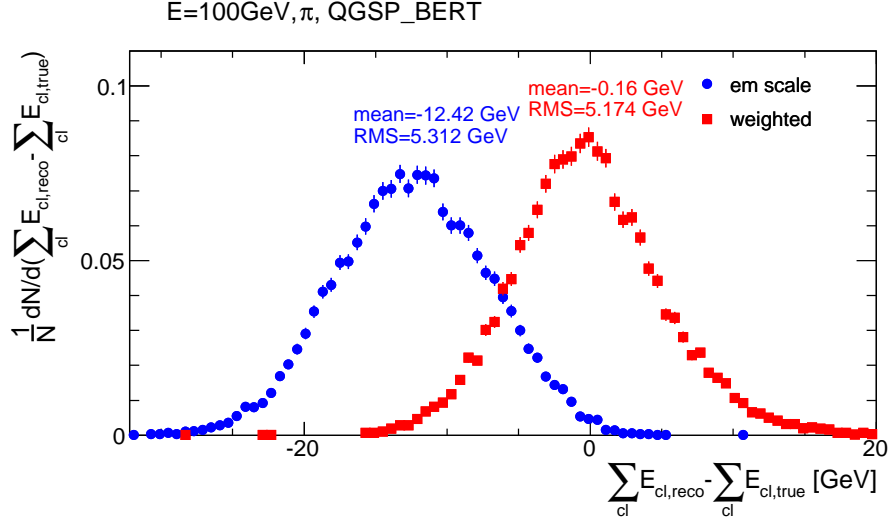


Figure 10.1: Difference between the sum of the reconstructed energy and the true deposited energy in all clusters for a simulation of pions at 100 GeV.

is observed. The relative deviation of the reconstructed energy from the true energy is below 1% for the whole energy range. The improvement of the resolution (RMS) of the relative deviation is about 15% at 20 GeV to 25% at 180 GeV. For both the linearity and the resolution the weighting is best for high energy.

10.3 Out-of-cluster corrections

The out-of-cluster (ooc) correction accounts for all energy depositions deposited outside of the clusters and the dead material (see sec. 8.2.3). Fig. 10.3 shows the difference between reconstructed and true out-of-cluster energy for simulated pions at 100 GeV.

The peak visible around -1.3 GeV seen in the distribution when no correction has been applied is significantly reduced after the correction. However, an asymmetric shape with a double peak structure can be observed where the peaks are slightly shifted with the reconstructed being larger than the true ooc energy. At the same time, a shoulder can be seen in the rising slope of the distribution. This asymmetry in the shape of the distribution is not observed when the ooc corrections are used which have been derived from ATLAS. The main difference between the CTB derived and the ATLAS derived ooc corrections is the range of beam energies which are used to compute the ooc corrections (logarithmic in ATLAS, in CTB see tab. 10.1). Hence, in the CTB more runs with a high beam energy compared to runs with a low energy are taken to derive the ooc corrections which might cause the different behavior of the reconstructed ooc energy.

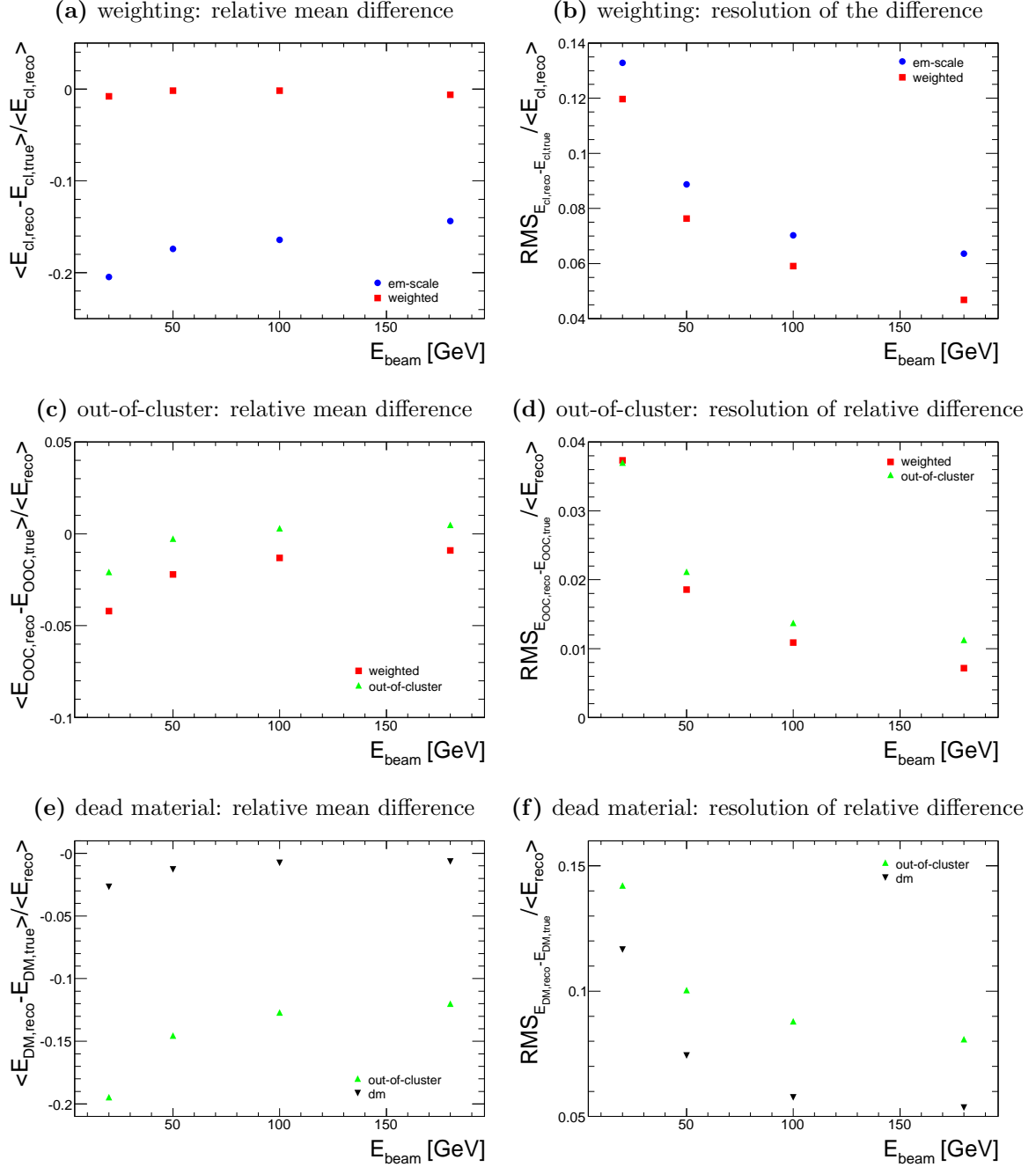


Figure 10.2: Blue circles, red squares, green triangles pointing upwards and black triangles pointing downwards indicate the energy response at the electromagnetic scale, after the weighting correction, after the out-of-cluster correction and after the dead material correction respectively. The figures on the left hand side (a), (c) and (e) show the relative mean differences of the reconstructed (E_{reco}) and the true (E_{true}) value of (a) the cluster energy (E_{cl}), (c) the out-of-cluster energy (E_{ooc}) and (e) the energy deposited in the dead material (E_{DM}). The figures on the right hand side (b), (d) and (f) show the respective resolutions of the relative differences.

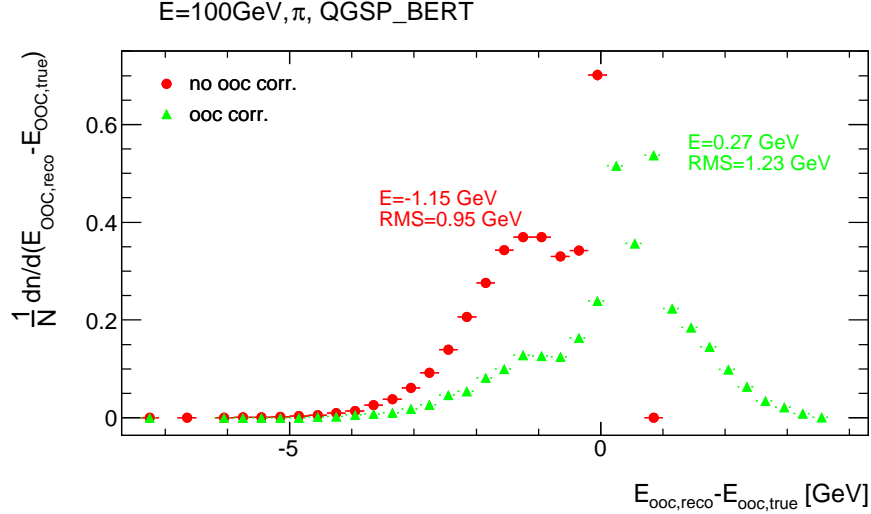


Figure 10.3: Difference between the reconstructed ($E_{\text{ooc, reco}}$) and the true ($E_{\text{ooc, true}}$) out-of-cluster energy in MC simulations of pions with an energy of 100 GeV.

In fig. 10.2c and 10.2d the relative deviation of the reconstructed from the true out-of-cluster energy and the resolution thereof are plotted for simulated pions. The out-of-cluster energy reduces the relative deviation for 20 GeV from about -4% to -2%, but over-corrects at 180 GeV from -1% to +0.5%.

With the ooc corrections derived from the CTB no significant improvement of the linearity has been achieved, but the reconstructed energy is closer to the true energy (see figs. 10.2c and 10.2d). The resolution of the deviation between reconstructed and true ooc energy worsens. Since the asymmetric shape and the worsening of the resolution of the difference between reconstructed and true ooc energy is neither observed for the CTB when the ATLAS derived ooc corrections are used nor in full ATLAS simulations, this problem seems to be a particular problem for the testbeam only. The reason for this is not clear and has to be addressed in the future.

10.4 Dead material corrections

The performance for dead material corrections shown in this section has been achieved with a layer-based parametrization using the energies deposited in the adjacent layers to estimate the energy lost in the dead material (see sec. 8.2.4). This method works similar to the ATLAS default method for dead material correction and has been therefore chosen as a benchmark.

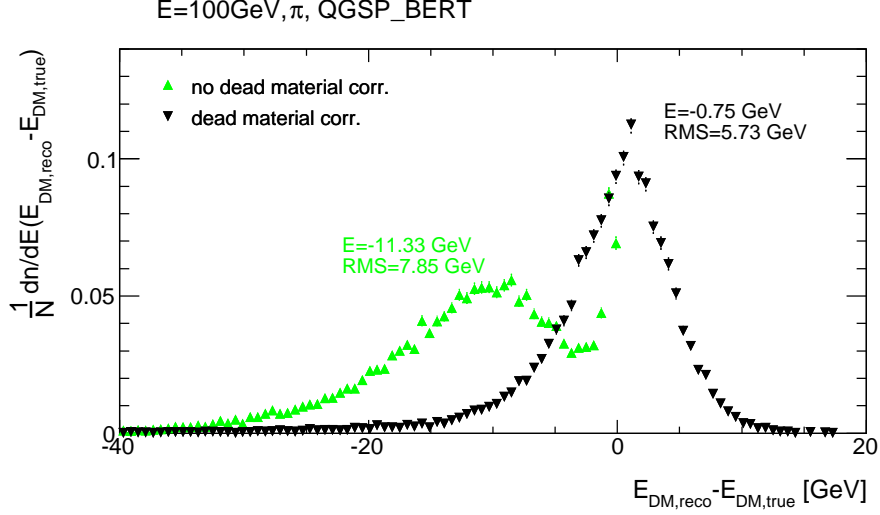


Figure 10.4: Difference between the reconstructed ($E_{\text{DM, reco}}$) and the true ($E_{\text{DM, true}}$) energy deposited in the dead material for simulated pions with an energy of 100 GeV.

The effect of the dead material correction for a beam energy of 100 GeV can be seen in fig. 10.4. The distribution for no dead material correction shows two peaks. The peak around zero is produced by events where only little energy is deposited in the dead material i.e. by events where the pion showers in the Tile calorimeter only, while the second peak is generated by events where some energy is deposited in the dead material. After the correction the double peak structure is reduced to a single peak with an maximum slightly above and with a mean energy slightly below zero. The RMS is significantly diminished reflecting in a remarkable improvement of the resolution.

The effect of dead material corrections can be observed in fig. 10.2e and 10.2f for the beam energies 20, 50, 100 and 180 GeV. At 20 GeV the dead material correction is underestimated by about 3%. With increasing beam energy, the energy is better reconstructed within 1% (see fig. 10.2e). The resolution is improved by about 15% at 20 GeV to 30% at 180 GeV (see fig. 10.2f). This shows that the dead material corrections are important for the ATLAS central calorimeter where there is $\sim 0.5\lambda$ of dead material between the LAr and the Tile calorimeter. The gain in resolution is similar or bigger than the one obtained by the weighting. By applying those corrections on data, the description of the detector geometry in the simulation and the ability to describe the energy depositions in the dead material by the physics lists is tested.

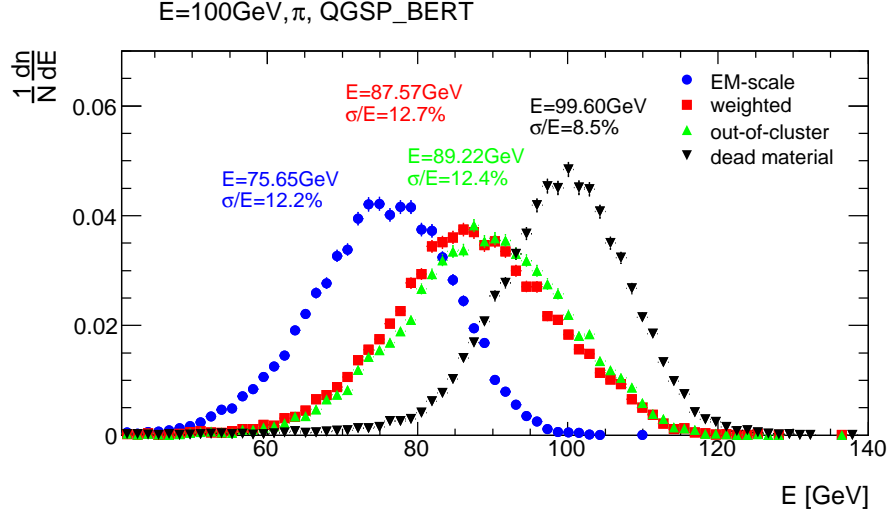


Figure 10.5: Distributions of the reconstructed energy at the em-scale (blue circles), after weighting (red squares), out-of-cluster correction (green triangles) and dead material correction (black triangles) for simulated pions with an energy of 100 GeV respectively.

10.5 Combined corrections applied on MC

The subsequent application of all three correction steps is shown in fig. 10.5. The energy distribution on the electromagnetic scale is indicated by blue circles. The energy distribution after the weighting step is shown with red squares, green triangles indicate the status after the out-of-cluster correction and finally black triangles pointing downwards show the energy distribution after all corrections are applied. The reconstructed energy after all corrections is approximately equal to the beam energy and the shape of the distribution is narrower and more Gaussian than at the em-scale.

Fig. 10.6 shows the linearity and the resolution obtained for the electromagnetic scale and after each correction step. Blue circles show the result on the electromagnetic scale, red squares after the weighting step, green triangles after the out-of-cluster correction and finally black triangles pointing down show the result after the dead material correction. At low beam energies, the reconstructed energy is about 3% too low. At high energies the deviation of the reconstructed to the true energy is within 1%. The resolution improves from 22% to 17% at 20 GeV and from 11.5% to 6.5 % at 180 GeV. The resolution function (see sec. 4.3) is fit to the obtained resolutions for the four beam energies 20, 50, 100 and 180 GeV after all steps of hadronic calibration. A stochastic term of $73.2\%/\sqrt{E}$ and a constant term of 3.8% is found. The function describes well the points.

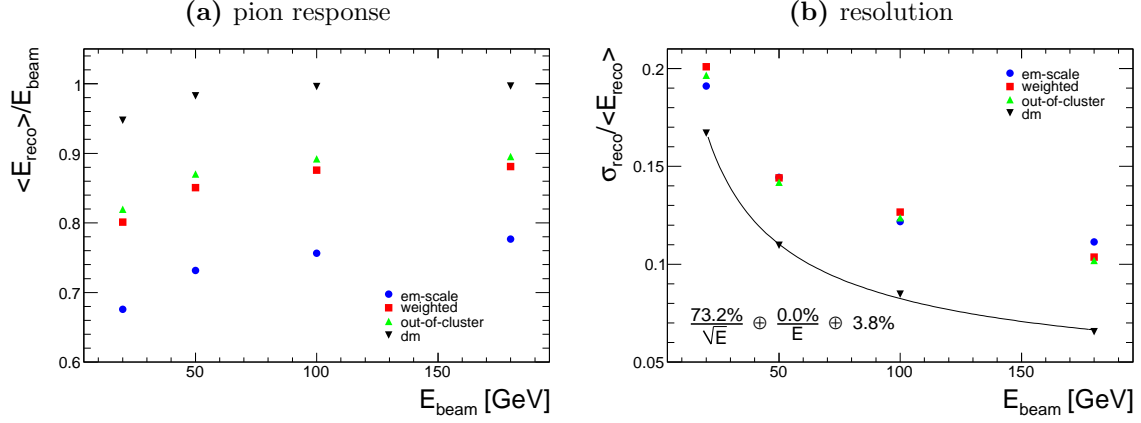


Figure 10.6: The response and resolution as a function of the pion energy for simulated pions for the electromagnetic scale and for each step of correction for MC simulations of pions.

10.6 Combined corrections applied on data

For the evaluation of the calibration scheme on data, the proton-contamination has to be taken into account. For this purpose, the previously mentioned MC simulations have been performed for protons as well and weights and corrections have been re-calculated. For each data run the weight files derived from pions and protons have been mixed with a pion/proton fraction according to the measured proton contamination for each energy.

Pions are mesons and thus the whole energy of the incident pion is deposited after or during the hadron shower. However, protons are baryons and due to the baryon number conservation, in a proton induced shower at the end of the shower development one baryon is left that has not deposited its energy in the calorimeter. Hence, there is a difference of the total deposited energy (visibly and invisibly) of one proton mass between a proton induced shower and a pion induced shower. To correct for this, all weights which were created with protons have been re-weighted with a factor $E_{\text{beam}} / (E_{\text{beam}} - m_p)$ where m_p is the proton mass.

Fig. 10.7 shows the application of all three correction steps on the data. The energy distribution after the weighting (red squares) is asymmetric with a large tail towards high energies. The ooc-correction (green triangles pointing upwards) shifts the distribution slightly to higher energies, but does not change the shape. The dead material correction reduces the asymmetry. The energy distribution is more Gaussian than before corrections, but such an effect has not been observed for the simulated pions. A large

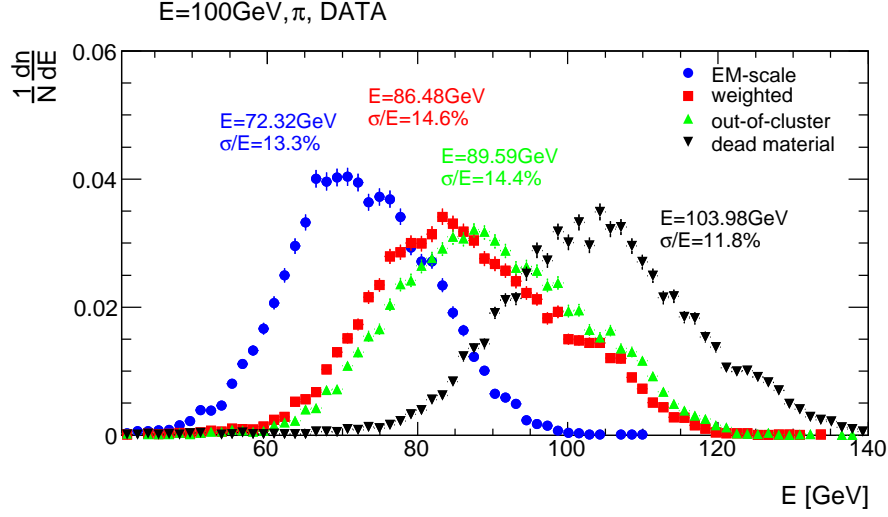


Figure 10.7: Distributions of the reconstructed energy at the em-scale, after weighting, out-of-cluster correction and dead material correction applied on data for a beam energy of 100 GeV respectively.

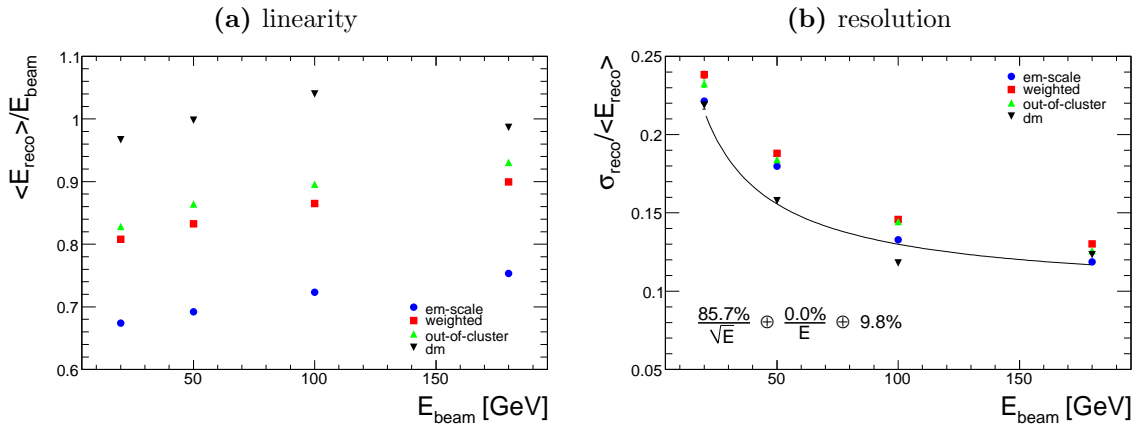


Figure 10.8: Linearity and resolution for the reconstructed energy of data at the em-scale, after weighting, out-of-cluster correction and dead material correction, respectively.

tail remains which deteriorates the resolution. The mean energy is 4% higher than the beam energy.

As for the MC simulations, the resolution function has been fit to the energy points. The fit does not describe the points. In particular, the point at 180 GeV seems to be too high. Since in data the proton contamination varies strongly for the different energies

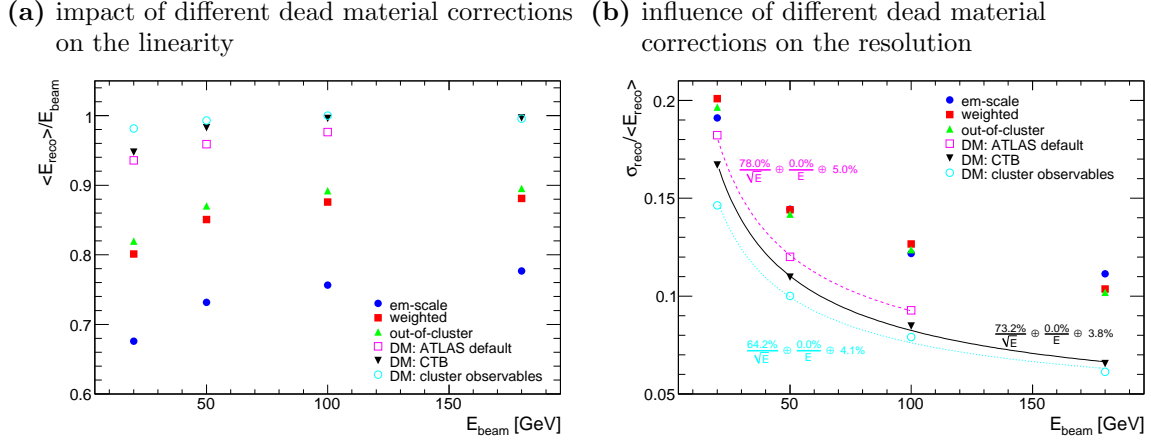


Figure 10.9: Linearity and resolution for the reconstructed energy of data at the em-scale, after weighting, out-of-cluster correction and for different types of dead material corrections respectively. The dead material correction of the ATLAS default calibration scheme is compared to the event based CTB specific dead material correction and to the dead material correction based on cluster observables.

and the resolution for pions and protons changes differently as a function of the beam energy, the values for the stochastic term, noise term and constant term should be only taken to guide the eye.

10.7 Comparison of different dead material corrections in MC simulations

As we have seen in the previous chapter, one of the most important factors for the energy resolution of the calorimeters in the ATLAS barrel region is the dead material correction (accounting for more than 10% of the true energy). It is therefore beneficial to optimize the performance of this part of the hadronic calibration. In fig. 10.9 three different methods of dead material corrections are compared.

The ATLAS default method (see sec. 8.2.4) has shown to have the worst linearity and resolution of the three methods, but it is the only one which is for the moment available and fully functional for the complete ATLAS detector. The CTB reconstruction is not any more supported with the newer versions of the ATLAS software (release $\geq 13.0.0$). This caused technical problems which prevented one from recalculating the dead material corrections with an extended energy range which includes the 180 GeV beam energy point. Hence this beam energy had to be left out in the comparison. The ATLAS default

achieves on Monte Carlo simulations a stochastic term of $78\%/\sqrt{E}$ and a constant term of 5% (see fig. 10.9b, open squares). The linearity is only about 5% in the region from beam energies from 20 GeV to 100 GeV (see fig. 10.9a, open squares).

The event based, parameterized method for the dead material correction (*CTB method*, see sec. 8.2.4) is only applicable on the testbeam. Since in the testbeam only single particles are impinging on the calorimeters, all dead material energy of an event is caused by one particle and can therefore be attributed to this particle. This is not the case for ATLAS, where at each event a multitude of particles will be created. There, the dead material energy has to be attributed to each of the reconstructed clusters. The CTB method is shown here as a benchmark method. The dead material corrections are derived for beam energies up to 180 GeV. A stochastic term of $73.2\%/\sqrt{E}$ and a constant term of 3.8% is achieved with the CTB method (see fig. 10.9b, filled triangles, pointing downwards). The linearity is within 5% in the region from beam energy 20 GeV to 180 GeV (see fig. 10.9a, filled triangles, pointing downwards).

The iterative assignment of dead material estimators to cluster observables is the most recent developed method (see sec. 8.2.4). The potential of this method is shown by taking the CTB method for the dead material correction, but replacing the correction for the dead material region between LAr and the Tile calorimeter by the new method. This is the most important dead material region for hadronic showers, since the hadronic showers are typically fully developed in that region and therefore a lot of particles pass this dead material region. An improvement there has a large impact on the performance of the whole hadronic calibration scheme. A stochastic term of $64.2\%/\sqrt{E}$ and a constant term of 4.1% is achieved with this combination of the CTB method and the iterative method in the LAr-Tile dead material region (see fig. 10.9b, open circles). The linearity is about 2% in the region of beam energies from 20 GeV to 180 GeV (see fig. 10.9b, open circles).

Fig. 10.10 shows the application of the three correction steps on the MC simulation if 20 GeV pions. Additionally to the weighting (red filled squares), the ooc correction (green filled triangles pointing upwards) there are the three types of DM corrections shown: the ATLAS default (magenta open squares), the CTB method (black triangles pointing downwards) and the iterative assignment of DM estimators to cluster observables (cyan open circles).

From the three compared methods for dead material correction, the ATLAS default correction performed the worst. An improvement can be achieved with the CTB method, but this method cannot be used for ATLAS. A further improvement is achievable with

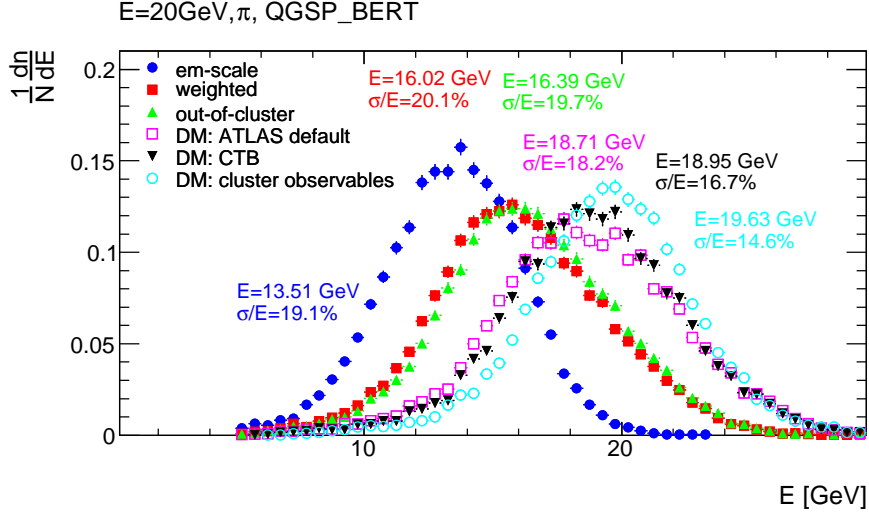


Figure 10.10: Distributions of the reconstructed energy at the em-scale, after weighting, out-of-cluster correction and three types of dead material correction (ATLAS default, CTB method and iterative assignment of DM estimators to cluster observables) applied on MC simulations for a beam energy of 20 GeV respectively.

the iterative method. This method can be used for ATLAS. The conclusions of the comparison of the different dead material correction methods are, that the iterative method should be implemented into ATLAS reconstruction in order to assess also its performance on jets.

10.8 Discussion

The resolution after the application of all corrections is worse in data than in MC. But already at the electromagnetic scale the resolution of data is worse than in MC. The description of the hadronic interactions improves in GEANT4.91 QGSP_BERT compared to GEANT4.7 QGSP_BERT in terms of total deposited energy and width of the distribution, which might lead to a better description of the resolution in the electromagnetic scale, i.e. a worsening of the resolution in MC. The deviation of the reconstructed from the true energy after all corrections have been applied is in MC for pions 2% for beam energies above 20 GeV and 5% for 20 GeV (see fig. 10.6, filled triangles pointing downwards). In data it is 5% at 20 GeV and within 5% for higher beam energies (see fig. 10.8, filled triangles pointing downwards).

The stochastic, noise and constant term from the fit of the resolution function to the energy points cannot be translated directly into the energy resolution of jets.

The analysis of the hadronic calibration on the testbeam is limited by the beam energies which have been used for data taking. In ATLAS particles and jets up to much higher energies (TeV scale) are expected. A further difference is, that in the testbeam only showers induced by single particles can be analyzed while in ATLAS showers often will be often created by a multitude of particles (jets).

The validation of the hadronic calibration on the CTB has shown, that the ATLAS default scheme works technically and does improve linearity and resolution of MC simulations and data of the testbeam. This is important since the calibration parameters have been extracted from the MC. The fact that the linearity can be reconstructed on the data proves that the quality of the MC simulations is sufficient to ensure a pion calibration to within a few percent. However, the performance on the data is worse than the one the MC. In data a pion energy is reconstructed within 5%. This shows that there is still some room for improving the MC simulations. The results which have been achieved by alternative techniques such as the event based *CTB method* and the cluster observable based *iterative method* where the ATLAS default dead material correction has been replaced have shown, that the performance can still be improved by better algorithms to reconstruct the pion energy.

Conclusions

In this thesis the signal of single pions has been investigated in detail using the data from the Combined Test Beam (CTB) 2004 where a full slice of the barrel of the ATLAS detector has been built up in the H8 beam line of the SPS at CERN.

The ability of the Monte Carlo simulations to describe the basic observables has been assessed. Using the best physics list, the description of the response is within 1% for a beam energy of 20 GeV and above. The mean energies in the individual calorimeter layers are described within 10 to 20%. The more complex variables characterizing the shower topology show in general a good agreement with data. However, none of the physics lists which have been used is capable of describing data for all observables which have been studied. Each observable though (except the radial extension) is described by at least one physics list. The longitudinal shower development and the cell density have shown to be largely influenced by the nuclear fragmentation model which is used in the physics list. Adding cascade models to the physics list makes showers longer and wider and they increase the total response which improves the agreement with data. From these comparisons, two physics lists usable within the GEANT4 framework have been recommended for the ATLAS simulations: QGSP_BERT and FTF_BIC. While the first one is in better agreement with data (except layer 2 of the LAr calorimeter), the latter one shows also a reasonable agreement with data, but describes different aspects of the data than QGSP_BERT (e.g. better description of LAr2, longer showers) and uses complementary models. It is therefore a good choice for assessing the uncertainties of the MC simulations.

The ATLAS default baseline calibration scheme where the non-measurable energy deposited in the calorimeter is estimated from the cluster energy and the cell density and where the dead material corrections are derived from the energy in the calorimeter layers in the vicinity of the dead material have been applied to data.

The corrections to fully restore the initial pion energy derived from MC simulations have been applied on both MC simulations and on the data. The comparison of the

fully corrected pion energy on MC and data have shown, that the concept of local hadronic calibration works in principle. Presently, above a beam energy of 20 GeV a deviation of the fully corrected pion signal from the beam energy of 2% and at 20 GeV 5% has been achieved.

The linearity after the hadronic calibration depends on both, the correction for invisibly deposited energy and energy deposited in dead material. The largest influence on the resolution comes from the dead material correction. The resolution is improved by about 10 (10) to 15% (40%) compared to the non-corrected signal in data (MC). However, the MC simulation doesn't reproduce well the resolution in the data before and after the energy correction.

A novel technique (iterative assignment of dead material estimators to cluster observables, see sec. 8.2.4) to extract the DM corrections has been developed and shown to improve the in MC the linearity to 2% for beam energies from 20 to 180 GeV and the resolution by about 8 (20 GeV beam energy) to 6% (180 GeV beam energy) compared to the benchmark method (CTB method, see sec. 8.2.4) for the CTB.

Outlook

In this thesis it has been shown, that the MC simulations are able to describe to a large extent the basic features of a hadron shower induced by pions or protons. The results obtained with the hadronic calibration scheme are still not perfect, but the framework is fully functional and can be used in ATLAS. This comparison will allow to better understand the response of the ATLAS calorimeter to pions or even jets produced in pp -collisions.

In particular in the beginning of the data taking period, isolated charged hadrons could be selected, for instance in minimum bias events, to study the response of the ATLAS calorimeter. Minimum bias events allow to access particle momenta up to about 10 GeV. For higher momenta, isolated τ -leptons (in the decay mode $\tau^+ \rightarrow \pi^+ \nu$) produced in Z - or W -boson decays, could be used. Once the track momentum measurement with the inner detector has been validated using electrons, the ratio of the energy measured in the calorimeter to the measured track momentum can be used to assess the hadronic calorimeter calibration. Comparison of such data to MC simulations and to the measurements performed in the testbeam as presented in this thesis will allow to assess first the basic understanding of the calorimeter and subsequently the ability of the calibration procedure to correct the pion and jet signals.

When the first ATLAS data will be available, the detector response has to be studied and to be compared to the simulations. Possible deviations might be due to several effects. This includes the identification of possible differences of the geometry between the ATLAS detector, its representation in the software and its correction. Regions where such deviations might occur are, for example the dead material regions, where components such as cables or details of cooling facilities could be missing in the geometry description of the simulation. This leads to approximations of the geometry whose accuracies have to be assessed in-situ. Other detector effects such as dead or noisy cells where cells produce unreasonable, non-physical signal (e.g. too large noise) or even don't work for a technical reason have to be found and repaired or the related cells have to be disabled, if no correction is possible. To disentangle the various possible effects studies of electrons, muons and hadrons will be necessary.

The subsequent step is studying jets. Since in the local hadronic calibration the energy corrections are determined from single charged and neutral pions and then applied to jets, the validation of the fully corrected pion signal in the testbeam and in the ATLAS detector will allow to assess certain aspects of the calibration of jets. This will complement the possibility to check the jet calibration in-situ via momentum balance in events, where a jet recoils on a photon or from the jets produced in the decay of a W -boson in events where two top quarks have been produced.

Appendix

Historical Remarks on the Monte Carlo Method

It was Stanislaw Ulam who was working for the Los Alamos National Laboratory who had the initial idea for a Monte Carlo algorithm in 1946. While convalescing from an illness and playing Canfield solitaire (a card game) he thought about the chances of laying out the 52 cards successfully. He first tried to do an estimation using combinatorial calculations, but soon thought of a more practical method which consisted in simply laying out the cards one hundred times and counting the plays which turned out successfully. The method's name "Monte Carlo" was suggested by Metropolis [38]. It seemed on one hand to be an obvious name for a statistical method being born during a card game and there was on the other hand a slight relation to an uncle of Stanislaw Ulam who is told to have borrowed money from relatives giving the reason he "just had to go to Monte Carlo." [38].

Stanislaw Ulam and John von Neumann applied this new "Monte Carlo" principle on a problem of their work, the neutron diffusion. Electronic computing techniques being developed at that time came in handy for treating the large number of calculations necessary for this type of statistical sampling techniques. They were successful in using the Monte Carlo method for determining the behavior of neutron chain reactions in fission devices. Neutron multiplication rates could be estimated and the explosive behavior of fission weapons designed at that time could be predicted [17, 38].

Due to the development of computers and software over the years even very complex and computing-time consuming concepts can be treated with MC methods. They are applied in a wide range of fields, such as the evaluation of multi-dimensional integrals, quantum mechanics, electromagnetics and many more. Of course, MC is still widely used for tracking elementary particles as in what has been the very first application of MC from Stanislaw Ulam and John von Neumann.

Glossary

Athena

The name of the ATLAS software framework for simulation, digitization and reconstruction (of data and simulations). 131

ATLAS

A multi-purpose LHC experiment for the measurement of pp -collisions. ATLAS is the acronym for A Toroidal LHC ApparatuS. 14

CalibrationHits

True energy which is deposited in active and non-active detector material per event. With the CalibrationHits the signal which is measured in the calorimeters can be compared to the true energy deposits in all parts of the detector. This is used to derive corrections for the energy measurement. 57, 90

CASTOR

CASTOR is the acronym for CERN Advanced STORage manager. It is a storage management system which provides disk- and tape-storage for the LHC experiments and for user files. 61

Combined Testbeam 2004 (CTB)

In the Combined Testbeam 2004 a full slice of the central region of the ATLAS has been installed in the CERN SPS H8 beam line. Pions and electrons with energies from 1 to 350 GeV have been tested. 63, 131

dead material (DM)

Inactive regions of the ATLAS detector where no energy measurement is carried out. For example, cables, support structures, cooling systems. 80, 90, 131, 135

escaped energy

In the simulation, some particles like neutrinos leave the simulated spatial region (experimental hall). The energy carried by these particles is called escaped energy. **34**, 90

GEANT4

A framework for the simulation of interactions of particles with matter using Monte Carlo simulation techniques. **41**, 131

GRID

A large scale computing infrastructure which consists of computing centers distributed around the globe. It has been designed to provide the computing power and storage requirements for the LHC experiments. **60**

invisible energy

Energy deposited by nuclear reactions in the detector which can not be measured. **34**, 88

Liquid Argon (LAr) Calorimeter

The part of the calorimeter system of the ATLAS detector which is optimized for the measurement of the energy of electromagnetic showers. **16**

LVL1 trigger

see *trigger system*. 22

minimally ionizing particle (mip)

Particles passing through matter and losing a minimal amount of energy by ionization. **26**, 30

missing transverse energy

energy which is expected by momentum conservation, but has not been measured in the particle detector. Examples are the transverse momentum carried by a neutrino. 1

Monte Carlo (MC) simulations

Computational statistical sampling techniques which can be applied to a wide range of scientific problems. In high energy particle physics MC simulations are used for the simulation of the interactions of particles with matter. **41**, 100

out-of-cluster correction

Out-of-cluster corrections aim at correcting for energy which is deposited outside of (topological) clusters and outside of dead material regions. 80, **90**, 131, 133

physics list

A selection of models for physical effects for the elementary particles in all energy ranges. 46, **54**, 56, 61, 100, 144

pseudorapidity

The pseudorapidity η describes the angle of a particle trajectory relative to the beam axis with $\eta = -\ln(\tan(\Theta/2))$ where Θ is the angle to the beam axis in radians. 15, 17–19, 21

Quantum Chromodynamics (QCD)

Theory of the strong interaction, describing the interaction of quarks and gluons. **1**

sampling calorimeter

Calorimeter type where slices of active and passive material alternate. 18, 20

sampling fraction

Fraction of the energy deposited in the active layers of the calorimeter divided by the energy deposited in both, active and passive layers. **29**

significance

The statistical significance expresses the confidence that the discovered signal is non-random. 6

stochastic term

Part of the calorimeter resolution which is driven by number of charged particles in the shower. **30**

Tile Calorimeter

The part of the calorimeter system of the central region of the ATLAS detector which is optimized for the measurement of the energy of hadronic showers. **20**

topological clustering

Grouping of adjacent cells with energy deposits which pass certain thresholds to clusters. 82

Transition Radiation Tracker (TRT)

Part of the ATLAS Inner Detector which measures transition radiation photons to separate electrons from pions and for track measurement. 16

trigger system

The task of the trigger system is the rejection of background events. The collision rate of the LHC is 40 MHz, but events read by ATLAS can only be written with a rate of about ~ 200 Hz to the mass storage. This reduction is done with three trigger levels, one hardware trigger ('LVL1', latency $\sim 2.5 \mu\text{s}$) a software trigger (latency ~ 10 ms) and the event filter (latency ~ 1 s). 22

visible energy

Energy deposited by ionization or scintillation in the calorimeter which can be measured. 34

weighting correction

Weighting is the correction for energy which is deposited "invisibly" (energy deposits which cannot be measured by the calorimeters) in the calorimeter cells. 80, 88, 131, 132

Bibliography

- [1] ALICE Collaboration. ALICE: Physics Performance Report, Volume I. *J. Phys. G: Nucl. Part. Phys.*, vol. 30(11) pp. 1517–1763, 2004.
- [2] LHCb Collaboration. *LHCb : Technical Proposal*. No. CERN-LHCC-98-004 ; LHCC-P-4 in Tech. Proposal. CERN, Geneva, 1998.
- [3] ATLAS Collaboration. *ATLAS Technical proposal for a general-purpose pp experiment at the Large Hadron Collider at CERN*. LHC Tech. Proposal. CERN, Geneva, 1994.
- [4] LHC Experiments Committee. *ATLAS tile calorimeter Technical Design Report*, vol. CERN-LHCC-96-042 of *Technical Design Report ATLAS*. CERN, Geneva, 1996.
- [5] W.-M. Yao et al. Review of Particle Physics. *J. Phys. G: Nucl. Part. Phys.*, vol. 33(1) pp. 1+, 2006.
- [6] C. W. Fabjan and F. Gianotti. Calorimetry for particle physics. *Rev. Mod. Phys.*, vol. 75(4) pp. 1243–1286, 2003.
- [7] E. Longo and I. Sestili. Monte carlo calculation of photon-initiated electromagnetic showers in lead glass. *Nucl. Instrum. Methods Phys. Res., Sect. A*, vol. 128(2) pp. 283–307, 1975.
- [8] R. Wigmans. *Calorimetry*. Oxford University Press, 2000.
- [9] N. Akchurin et al. On the differences between high-energy proton and pion showers and their signals in a non-compensating calorimeter. *Nucl. Instrum. Methods Phys. Res., Sect. A*, vol. A408 pp. 380–396, 1998.
- [10] D. E. Groom. Energy flow in a hadronic cascade: Application to hadron calorimetry. *Nucl. Instrum. Methods Phys. Res., Sect. A*, vol. 572(2) pp. 633–653, 2007.
- [11] H. Hakobyan, M. Simonyan, T. Carli and A. M. Henriques-Correia. Measurement of pion and proton longitudinal shower profiles up to 20 nuclear interaction lengths with the atlas tile calorimeter. *CERN*, (ATL-COM-TILECAL-2006-014), 2006.
- [12] R. K. Bock, T. Hansl-Kozanecka and T. P. Shah. Parametrization of the longitudinal development of hadronic showers in sampling calorimeters. *Nucl. Instrum. Methods*, vol. 186(3) pp. 533–539, 1981.

- [13] S. Agostinelli et al. Geant4 – a simulation toolkit. *Nucl. Instrum. Methods Phys. Res., Sect. A*, vol. 506(3) pp. 250–303, 2003.
- [14] J. Allison et al. Geant4 developments and applications. *IEEE T. Nucl. Sci.*, vol. 53(1) pp. 270–278, 2006.
- [15] The GEANT4 collaboration. GEANT4. URL <http://geant4.cern.ch>, 2007.
- [16] K. Binder and D. Heermann. *Monte Carlo Simulation in Statistical Physics: An Introduction*. Springer Verlag, 2002.
- [17] R. Eckhardt. Stan Ulam, John von Neumann, and the Monte Carlo method. *Los Alamos Science*, vol. Special Issue (15) pp. 131–137, 1987.
- [18] A. Fasso’ et al. The physics models of FLUKA: Status and recent development. In *CHEP03, March 24-28, 2003, La Jolla, California*. 2003.
- [19] A. Ferrari, P. R. Sala, A. Fasso’ and J. Ranft. *FLUKA: A multi-particle transport code (program version 2005)*. CERN, Geneva, 2005.
- [20] M. Goossens. *GEANT — Detector Description and Simulation Tool, long writeup W5013*. CERN Program Library. CERN, Geneva, 1993.
- [21] J. P. Wellisch. Hadronic shower models in GEANT4 – the frameworks. *Comput. Phys. Commun.*, vol. 140(1-2) pp. 65–75, 2001.
- [22] H. S. Fesefeldt. The simulation of hadronic showers : physics and applications. Tech. Rep. PITHA-85-02, Aachen RWTH Inst. Phys., Aachen, 1985.
- [23] G. Folger and J. P. Wellisch. String parton models in Geant4. In *CHEP03, March 24-28, 2003, La Jolla, California*. 2003.
- [24] G. Folger, V. N. Ivanchenko and J. P. Wellisch. The Binary Cascade - Nucleon nuclear reactions. *Eur. Phys. J. A*, vol. 21 pp. 407–417, 2004.
- [25] A. Heikkinen, N. Stepanov and J. P. Wellisch. Bertini intra-nuclear cascade implementation in Geant4. *Proc. Computing in High Energy and Nuclear Physics, La Jolla CA*, vol. MOMT008, 2003.
- [26] B. Di Girolamo et al. Beamline instrumentation in the 2004 combined ATLAS testbeam. *CERN*, (ATL-COM-TECH-2005-001), 2005.
- [27] H8 SPS Beam Line User Guide. URL <http://nahandbook.web.cern.ch/nahandbook/default/h8/H8usermanual.pdf>, 1996.
- [28] J. Spanggaard. Delay wire chambers – a users guide. *CERN*, (SL-Note-98-023-BI), 1998.

- [29] G. Jaffe. Zur Theorie der Ionisation in Kolonnen. II. *Annalen der Physik*, vol. 393(7) pp. 977–1008, 1929.
- [30] S. Amoruso et al. Study of electron recombination in liquid argon with the ICARUS TPC. *Nucl. Instrum. Methods Phys. Res., Sect. A*, vol. 523(3) pp. 275–286, 2004.
- [31] R. T. Scalettar, P. J. Doe, H. J. Mahler and H. H. Chen. Critical test of geminate recombination in liquid argon. *Phys. Rev. A: At., Mol., Opt. Phys.*, vol. 25(4) pp. 2419–2422, 1982.
- [32] V. Vuillemin et al. Characteristics of the charge response to alpha and beta particles in liquid argon doped with ethylene. *Nucl. Instrum. Methods Phys. Res., Sect. A*, vol. 327(1) pp. 44–47, 1993.
- [33] RD4 Collaboration. Final report on the RD-4 project. Tech. Rep. CERN-DRDC-93-23, CERN, Geneva, 1993.
- [34] W. E. Cleland and E. G. Stern. Signal processing considerations for liquid ionization calorimeters in a high rate environment. *Nucl. Instrum. Methods Phys. Res., Sect. A*, vol. 338(2-3) pp. 467–497, 1994.
- [35] M. Aleksa et al. ATLAS Combined Testbeam: Computation and Validation of the Electronic Calibration Constants for the Electromagnetic Calorimeter. Tech. Rep. ATL-COM-LARG-2006-003, CERN, Geneva, 2006.
- [36] P. Adragna et al. The ATLAS hadronic tile calorimeter from construction toward physics. *IEEE T. Nucl. Sci.*, vol. 53 pp. 1275–81, 2006.
- [37] Y. A. Kulchitskii et al. Electromagnetic cell level calibration for ATLAS Tile calorimeter modules. Tech. Rep. CERN-ATL-TILECAL-PUB-2007-001, CERN, Geneva, 2006.
- [38] N. Metropolis. The beginning of the monte carlo method. *Los Alamos Science*, vol. Special Issue (15) pp. 125–130, 1987.

Curriculum Vitae

I was born June 26th, 1976 in Vienna, Austria. In Vienna I attended the Primary School (1982-1986) and the Secondary School (AHS) (1986-1990). From 1990 to 1995 I attended the “HTL-Wien XX, Technologisches Gewerbemuseum”, department for electronics–biomedical engineering. This is a special type of school, where the secondary school is combined with specialised technical education. During this time, I carried out four traineeships, the first in summer 1992 at Knoblich Licht GmbH. and the subsequent three in the following summers at Siemens Nixdorf Informationssysteme GmbH. In June 1995 I passed the Austrian school leaving examination (general university entrance exam) with honor.

From October 1995 to September 1996 I carried out my military service at the Austrian military. In 1996 I began my studies in Technical Physics at the Technical University of Vienna. During my study I worked several times at Breitenbach and Heller (development of computer programs) and two times as a trainer for Badminton. From February 2002 to September 2002 I studied physics in the Universidad Autónoma de Madrid in Spain with the ERASMUS students exchange program.

In 2004 I worked on my diploma thesis at the “Institut für Festkörperphysik” of the Technical University of Vienna with the topic “Electron Microscopy and Micromagnetic Simulation of FePt and CoPt Nanoparticles”. In 2004 I passed the diploma examination in Technical Physics at the Technical University of Vienna. In 2005 I was accepted as a student in the CERN Austrian Doctoral Student Program. In July 2005 I started working on my PhD thesis in the CERN ATLAS calorimeter group on the topic “Energy measurement with the ATLAS calorimeter”.